Effect of Radiation on Electronic Devices

Mohamed Aslam.P

University of Calicut, Kerala

Thesis submitted to the University of Calicut for the award of the Degree of **DOCTOR OF PHILOSOPHY IN PHYSICS.**
2017

DEPARTMENT OF PHYSICS
UNIVERSITY OF CALICUT

CERTIFICATE

This is to certify that the thesis entitled **Effect of radiation on electronic devices**, is a record of bona fide research work carried out by Mohamed Aslam P, under my guidance. It is also certified that the corrections/suggestion from the adjudicators have been incorporated.

(Sd/-)
Dr. M. M. Musthafa
Research Supervisor

DECLARATION

I hereby declare that, this thesis entitled **Effect of Radiation on Electronic Devices** is a bona fide record of research work carried out by me and that no part of this thesis has been presented before the award of any other degree or diploma.

Calicut University   Mohamed Aslam. P.

Dedicated to
My Parents, Wife & Children

Acknowledgments

It gives me immense pleasure to acknowledge my deep sense of gratitude and indebtedness to Dr. M. M. Musthafa, my thesis supervisor, Professor and the former Head of the Department of Physics, University of Calicut, for helping and inspiring me throughout my work.

I express my sincere thanks to Dr. Sreekumar, Director, Indian Institute of Astro Physics Bangalore, Dr. Radhakrishna, Koushal V, ISRO Satellite Centre, Bangalore, Dr. S R Banerjee, Variable Energy Cyclotron Centre, Kolkata, Dr. A. K Sinha (Director), Dr. S. Ghugre and Dr. P Sudarshan, UGC-DAE Consortium for Scientific Research, Kolkata, Dr. E. Krishnkumar, Dr. P. Surendran, Dr. J.P. Nair and other scientific and technical staff of Tata Institute of Fundamental Research, Mumbai, Mr. Rajesh K R and Mr. Biju P Thomas, Senior Medical Physicists, Caritas Hospital, Kottayam for their collaboration, support and assistance, in various stages of the work at the respective centres, without which it may not be possile for me to complete the work and to my fellow research schoars of the nuclear physics team at Univeristy of Calicut Dr. Satheesh, Rajesh, Najmunnisa, Hind, Shan, Salma for their support and involvement in conducting my experimental work.

I am thankful to Dr. Antony Joseph, Former Heads of the department and faculties of the department for encouragement and valuable advice and to other technical and administrative staff of the department for their constant support.

I also express my sincere thanks to the principals of SARBTM Govt College, Koyilandi and Govt. Arts and Science College, Calicut and my colleagues there for their ardent support, particularly to Dr. Abdul Gafoor and Dr. Rajan Nambiar for scrutinising the script.

I am really at loss of words to express my obligation to my family and all my relatives who have supported me all through this journey. This thesis owes most to them.

The support from University Grants Commission by providing me the FDP fellowship to carry out my research work is immensely acknowledged here.

Introduction

Development in studies in Physics that leads to technological evolution and progress has significant role in developing various instruments and devices in modern world. The development in industry, agriculture, medicine, communication space etc. has to tell stories about the series of its growth and development based on observation and theories in physics developed from time to time. Discovery of atoms and the development of nuclear physics has revolutionized the concepts in communication and medicine.

In this modern era of satellite technology and space exploration, the demand for newer outlook and approaches are ever increasing. In the case of space technology, the satellites and space components are placed in outer space of earth and are continuously exposed to various atomic and nuclear radiations from various extra terrestrial sources. This radiation interacts with materials of the device and thereby causes damage or change to the performance and life of the device and components. Thus the interaction of the radiation with matter and the related effects are important in space technology. This will help us in devising the components which are radiation hardened and radiation masks without affecting the performance of the device. Further, the quantitative and qualitative analysis of the radiation effects on each component will be helpful in eliminating their contribution to the output signals to apply proper signal processing techniques to extract the actual data.

Study of interaction of radiation with matter is also important in various fields of science and technology like agriculture, medicine, research and industry. In agriculture, it is used in various stages in the modification of seeds, germination to food processing. In medicine radiation techniques are widely used in diagnosis as well as treatment of various ailments including cancer. In industry new materials are being developed and the properties of materials are altered with the help of radiation technology. The development of new radiation detectors with a complete knowledge of the effect of radiation on the performance of these detectors is very important in the advancement of scientific research.

Space Radiation and Electronics

Electronic and detector technology is the backbone of space mission and exploration. Control of space craft to place satellites in the suitable orbit, data exchange between space craft and ground based control room and observatory, Control of power supplies within space craft etc. require efficient use of electronic technology. The captured images of the space object and other

space environmental data by the satellites are accessible from the ground based laboratories and space stations with help of sophisticated electronic wireless communication devices and systems in the space vehicles and satellites.

Electronic systems in the space is built around micro miniature chips, components, sensor elements, detectors etc. The resolution and the quality of data received on the earth is limited by the resolution and quality of these systems. Any deterioration caused to this system due to aging or due to device degradation of any kind such as exposure to radiation environment etc. will affect the reliability of the data received on the earth. Hence it is important to understand the space radiation environment, the total dose expected to expose the devices during the mission period, the consequent deterioration of the device and the system and finally how it may affect the data received on the earth.

A systematic study of the individual device deterioration, when exposed to various types of radiation expected in space, is required to understand the mechanism involved and to evolve the correct models and theories that explain the observed effects. The study involve, identifying the radiations of various types and exposing the device to various dose levels and examines the device variation at these dose levels for different energies. In addition to our general understanding of the interaction of radiation with matter, ionizing and non-ionizing energy loss in the material of semiconductor, there are factors that depends the particular device technology such as thickness of the oxide films that permits tunneling of the carriers, and annealing effects during and after radiation, effects of applied bias during radiation, dependence of temperature during and after radiation etc.

The first part of the study is done to understand the effects due to radiation on discrete components such as transistor, diodes etc.

In the second part, *in-situ* measurements have been carried out on transistors to understand the variation of characteristics of the devices during the time of radiation.

The third part of the study is done on a space grade sensitive X-ray Fluorescence Detector under the name "Swept Charge Device". The performance of the device has been studied under various bias conditions, various operating frequencies and temperatures before exposing to radiation. The optimization of the device is made for the best resolution of the device for the operation in space.

The fourth part of the experiment involves damaging the device with protons of definite fluence controlled by a Rutherford Scattering Setup generated from Cyclotron at VECC, Kolkotta. Later, the experiment was repeated from Pellatron at TIFR, Mumbai. The results were analyzed for the observed effects. The defects generated in the system are analyzed.

The fifth part of the experiment is to understand the annealing behavior of the X-ray fluorescent detector, which is very much important for the space application of the device. Irradiation and annealing of the detector system were performed at room temperature.

An understanding of the space radiation environment is necessary for planning the study. Chapter I discuss the radiation environment of the space in brief. An introduction to the various types of interaction of different radiation with matter and associated effects in space electronic devices is discussed in the following sections. Interaction of radiation with matter is detailed in chapter II. The effects produced due to the above interaction in materials and associated changes in electrical, electronic and thermal properties of the material are discussed in the chapter III. Chapter IV discuss semiconductor technology in general and that of CCD used in space in particular. The effects of radiation in materials and devices and their consequences due to various types of radiation in space. Chapter V describe the experimental tools used in the study, the experimental set up, the results of the experiment and the analysis of the results. Chapter VI discuss the experiments done in detail and the analysis. The last section is the conclusion and the future plans.

Contents

1 Radiation Environment of Space 1

1.1 The Trapped Radiation 1
1.2 South Atlantic Anomaly & Auroral Horns 3
1.3 Non-Trapped Radiation 3
1.4 Cosmic Rays 3
1.5 Solar Flare 4

2 Interaction of Radiation with Matter 7

2.1 Interaction of Photons with Matter 7
2.1.1 Scattering 7
2.1.2 Photo electric effect 11
2.1.3 In-elastic or Incoherent scattering. 13
2.1.4 Photo nuclear interaction 15
2.1.5 Gamma ray attenuation 15
2.2 Interactions of Particles with Matter 16
2.2.1 Stopping power 17
2.2.2 Range of charged particle 17
2.2.3 Interaction of electrons 17
2.2.4 Positron interaction 19
2.3 Interaction of neutrons 19

3 Radiation Effects in Materials 22

3.1 Effects of Interaction of Electromagnetic Radiation 22
3.2 Effects of Heavy ions 23
3.3 Illustrative Example 26
3.3.1 Metals 26
3.4 Basic mechanism and their trends 29
3.4.1 Total dose effects in semiconductors 29
3.4.2 Displacement damage 29
3.4.3 Single event effects 30
3.4.4 Single event upset (SEU) and Multiple bit upset 31
3.4.5 Latch-up and Snap back 31

3.4.6 Single event hard errors 32
3.4.7 SEE rate calculations 33

4 Semiconductor Technology for Space Applications 36
4.1 Semiconductor Devices 36
4.1.1 Energy bands in solids 37
4.1.2 Direct and Indirect band semiconductors 39
4.1.3 Effective mass of the electrons and holes 39
4.1.4 Hole conduction 40
4.1.5 Excess carriers in semiconductors 40
4.1.6 Photo generation 41
4.1.7 Transient decay of excess carriers 41
4.1.8 Recombination mechanism 42
4.1.9 Auger recombination 42
4.1.10 Origin of Traps centers 43
4.1.11 Diffusion of charge carriers 44
4.1.12 Einstein relation 44
4.2 Junction Diodes 45
4.2.1 Electric field distribution in a diode 45
4.2.2 Electric potential distribution in a diode 46
4.2.3 The Ideal Diode equation 46
4.2.4 Depletion layer capacitance 48
4.3 Bipolar Junction Transistor (BJT) 48
4.3.1 Current flow in a transistor 49
4.3.2 Transistor - Ebers model 50
4.3.3 Transistor characteristics 52
4.4 Charge Coupled Devices(CCD) 58
4.4.1 CCD theory 62
4.4.2 Accumulation (When gate is negatively biased) 62
4.4.3 Depletion (When gate is positively biased) 63
4.4.4 Inversion and pinning (When gate is driven negatively) . 68
4.4.5 Bulk damage 70
4.4.6 Space radiation damage to CCD 71
4.4.7 Radiation units 73
4.4.8 Bulk damage equivalence 76
4.4.9 Generation of charge in a CCD 78
4.4.10 Dependence of operating temperature on QE performance 79
4.4.11 Effect of Channel stop region in the charge generation process 79
4.4.12 Virtual phase CCDs 79

4.4.13 Charge transfer 81
4.4.14 The mechanism of charge transfer 82
4.4.15 Measurement of Charge transfer efficiency 83
4.4.16 Charge Injection for CTE measurements 84
4.4.17 Traps 84
4.4.18 Fat-Zero compensation 85
4.4.19 Measurement of charge 86

5 Tools and Techniques Used **91**

5.1 Common Tools and Techniques Used for the Study of Radiation Damage on Electronic Devices 91
5.1.1 SRIM and TRIM 91
5.1.2 GEANT 4 93
5.1.3 SPENVIS 94
5.1.4 Deep Level Transient Spectroscopy 96
5.1.5 Device characterizers 96
5.1.6 ExpEyes 96
5.1.7 Development of Data acquisition systems 97

6 Experimental Observation and Analysis **106**

6.1 Study of the Effect of Space Radiation on Electronic Devices . . 106
6.1.1 Introduction 106
6.1.2 Phase - 1 Effect of radiation on discrete devices- Offline Study 107
6.2 Irradiation Effect on Junction Diodes 108
6.2.1 Electron irradiation effect 112
6.3 Effect of Radiation on Zener Diode 116
6.3.1 Zener diode - Effect of radiation under forward bias . . . 116
6.3.2 Zener diode under reverse bias - Electron effect study . . 123
6.4 Effect of Ionizing Radiation on Transistors 125
6.4.1 Transistors - Photon irradiation effect study 125
6.4.2 Transistors - Electron irradiation effect study 126
6.5 Transistors - Radiation Effect - *in-situ* Study of the Device Characteristics 129
6.5.1 The Experimental setup 130
6.5.2 Phase - 3 - Ground test on the device used in space - Analysis of proton irradiation effect on SCD (CCD236) X-ray fluorescence detector 140
6.5.3 Experimental study on the effect of proton irradiation on SCD 150

6.5.4 Room temperature annealing of CCD irradiated by protons at high doses 164
6.6 Conclusion 170

List of Figures

1.1 Jason-1 exposure to South Atlantic Anomaly effects, measured on 200-2004 period using the Doris ultra-stable oscillator. (Credits Cnes/CLS) 3

2.1 Scattering of particles 10
2.2 Relative importance of three major types of gamma ray interactions. (R D Evans, The atomic nucleus, Mc.Graw-Hill Book Company) 14
2.3 Contribution to total mass absorption coefficients from Photoelectric effect, Compton effect and Pair production. (H A Enge,1966, Introduction to nuclear physics, page 193, Addison Wasely Publishing(Co.)) 16
2.4 Stopping power. Nuclear and electronic contributions. NIST data. [www.nist.gov/pml/stopping-power-range-tables-electrons-protons-and-helium-ions] 18

3.1 Variation of resistivity with deutron beam flux. ASTM technical publication, No 208, Sept.20,1956. 27
3.2 Increase of resistivity of of a tungsten wire with energy of beam flux; www.astm.org/Standards/electronics-standards.html 28
3.3 Effect of heating on length and resistivity of irradiated copper; ASTM data 28

4.1 Silicon atomic structure - Possible X-ray florescence transitions 38
4.2 Energy band diagram with and without electric field 38
4.3 Energy of electron as a function of k. (a) Direct band and (b) indirect band semiconductors 40
4.4 Auger recombination 43
4.5 Trap aided Auger recombination 43
4.6 Distribution of Charge carriers, Charge density, Electric potential and Electric field 45
4.7 Minority carrier distribution across forward biased PN junction 47
4.8 Ideal diode characteristics with current in log scale 48

4.9 PNP transistor structure . . . 49
4.10 Current components in a forward biased pnp transistor . . . 49
4.11 Common emitter, common collector and common base configuration . . . 51
4.12 Ebers Moll model of p-n-p transistor . . . 52
4.13 Transistor configuration(p-n-p) . . . 53
4.14 Input characteristics (p-n-p) . . . 53
4.15 Output characteristics of p-n-p transistor - common base configuration . . . 53
4.16 p-n-p transistor- common emitter configuration . . . 54
4.17 p-n-p transistor- common emitter characteristics . . . 54
4.18 Output characteristics of a p-n-p transistor . . . 57
4.19 (Above)Variation of I_B and I_C with V_{BE}; (Below) Plot of β Vs. I_C for constant V_{CE} . . . 57
4.20 Clock voltage determine the the depth of potential well for the collection of charges . . . 59
4.21 Accumulation of charges . . . 63
4.22 Accumulation - Band diagram . . . 63
4.23 Depletion of charges . . . 64
4.24 Gate bias conditions to achieve depletion . . . 64
4.25 Buried channel-potential maximum shown beneath the surface . 66
4.26 Interface state creation. Dangling bonds and H passivated bonds are shown . . . 71
4.27 Experimental setup to expose CCD to Fe^{55} X-rays . . . 77
4.28 $Fe^5 5$ Spectrum . . . 78
4.29 Optimum full well bias condition for collecting phase . . . 81

5.1 SRIM simulation showing 1 MeV proton trajectories in CCD 236 92
5.2 SRIM simulation showing 1 MeV proton trajectories in CCD 236 94
5.3 Circuit diagram - Data Aquisition System Control Board . . . 98
5.4 Circuit diagram - Data Aquisition System Test Board . . . 98

6.1 Junction diodes- Pre-irradiation characteristics of the samples . 108
6.2 Characteristics of p-n junction after irradiation by photons of different energy at a constat dose level . . . 109
6.3 p-n Junction (1N 4001)-Comparison of characteristics after irradiation with different photon energy (current in the log scale) . 110
6.4 Characteristics of p-n junction after irradiation by 6 MeV photons to different doses . . . 110
6.5 Diode forward bias characteristics after 6 MeV photon irradiation. Study of the effect of variation of dose . . . 112

6.6 Characteristics of pn junction before and after irradiation under different electron energy 113
6.7 V-I characteristics of PN junction after irradiation with electrons of different energy (with current in log scale) 114
6.8 Characteristics of pn junction before and after irradiation under different electron doses 114
6.9 V-I characteristics of p-n junction after irradiation with electrons of different energy (with current in log scale) 116
6.10 Zener diode - Forward characteristics after irradiation with photons of different energies 117
6.11 Zener diode - Forward characteristics after irradiation with photons at different doses 118
6.12 Zener diode - Forward characteristics after irradiation with photons at different energies - in logarithmic scale 119
6.13 Zener diode - Forward characteristics after irradiation with electrons at different energies - in logarithmic scale 119
6.14 Zener diode - Forward characteristics after irradiation with electron of different energies 120
6.15 Zener diode - Forward characteristics after irradiation with electron at different doses 120
6.16 Zener diode - Reverse characteristics before and after irradiation with photons at different energies 121
6.17 Zener diode - Reverse characteristics after irradiation with electrons at different energies along with that before irradiation . . 122
6.18 Zener diode - electron dose effect study on reverse characteristics. Compared with that of Pre-irradiation plot 123
6.19 Zener diode - Photon dose effect study on reverse characteristics. Compared with that of Pre-irradiation plot 124
6.20 BJT Pre-irradiation output characteristics for $I_B = 10, 30, \&50(\mu A)$ 126
6.21 Comparing pre-irradiation characteristics with that of post-irradiation under two different Photon energies at I_B= 10 micro Amps . . 127
6.22 Comparing the output characteristics of transistors irradiated with photon of different doses with that of pre-irradiated device 127
6.23 Comparing the output characteristics of transistors irradiated with electrons of different energies with that of pre-irradiated device 128
6.24 Hole traps near the surface and the insulating layer result in the formation of inversion layer 129
6.25 experimental setup 131
6.26 data flow sequence 132

6.27 Effect of cumulative dose and dose variation effect of 6 MeV Xrays on transistor to produce random noise with instances of negative resistance . . . 133
6.28 Transistor 2N 2222, Effect of dose and dose rate of 15 MeV photon irradiation . . . 134
6.29 Transistor- BC 547, Effect of dose , dose rate and energy of photon irradiation . . . 134
6.30 Random telelgraphic signals . . . 138
6.31 Energy levels due to traps within the band gaps . . . 139
6.32 CCD Prototype . . . 141
6.33 SCD structure . . . 142
6.34 Typical X-ray spectrum emitted by Fe^{55} source as recorded by SCD at temperature -20 degree . . . 145
6.35 Mn Kα peak : Variation of FWHM with clock voltage at different temperatures . . . 146
6.36 Noise peak : Variation of FWHM with clock voltage at different temperatures . . . 147
6.37 Mn Kβ peak : Variation of FWHM with clock voltage at different temperatures . . . 147
6.38 Noise peak - FWHM Vs, Clock Frequency at different temperatures . . . 148
6.39 Mn Kα line - FWHM Vs, Clock Frequency at different temperatures . . . 149
6.40 Mn Kβ line - FWHM Vs, Clock Frequency at different temperatures . . . 149
6.41 FWHM Vs clock voltage at different temperatures. For 5.9 keV peak and 6.4 keV peaks . . . 152
6.42 FWHM Vs clock frequency at different temperatures . . . 153
6.43 Rutherford Scattering Setup for irradiation of SCD . . . 154
6.44 SRIM simulation showing 1 MeV proton trajectories in CCD 236 156
6.45 Histogram showing proton peak and background gamma rays . . 157
6.46 Variation of FWHM with clock voltage of CCD of the Mn Kβ line of Fe^{55} spectrum, at 100 kHz and -30° C; Comparison of pre and post irradiation performance. . . . 159
6.47 Variation of FWHM with clock voltage of CCD of the noise peak in the spectrum, at 100 kHz and -25° C; Comparison of pre and post irradiation performance. . . . 159
6.48 Variation of FWHM with clock voltage of CCD of the noise peak in the spectrum, at 100 kHz and -30° C; Comparison of pre and post irradiation performance. . . . 159

6.49 Variation of FWHM with clock voltage of CCD of the Mn Kα line of Fe^{55} spectrum, at 100 kHz and -25° C; Comparison of pre and post irradiation performance. 160
6.50 CCD 1: Variation of FWHM with temperature of CCD for the Mn Kβ line of Fe^{55} spectrum, at 100 kHz and 7.0 Volts; Comparison of pre and post irradiation performance. 161
6.51 CCD 1: Variation of FWHM with temperature of CCD for the Mn Kα line of Fe^{55} spectrum, at 100 kHz and 7.0 Volts; Comparison of pre and post irradiation performance. 161
6.52 CCD 1: Variation of FWHM with temperature of CCD for the zero energy peak of Fe^{55} spectrum, at 100 kHz and 7.0 Volts; Comparison of pre and post irradiation performance. 162
6.53 CCD 2: Variation of FWHM with temperature of CCD for the Mn Kα line of Fe^{55} spectrum, at 100 kHz and 7.0 Volts; Comparison of pre and post irradiation performance. 162
6.54 CCD 2: Variation of FWHM with temperature of CCD for zero energy peak of Fe^{55} spectrum, at 100 kHz and 7.0 Volts; Comparison of pre and post irradiation performance. 162
6.55 Comparison of CCDs: Variation of the post irradiation performance with temperature in two CCDs 163
6.56 Post irradiation comparison of CCDs: Variation of post irradiation performance with temperatures - (Mn Kαline) of Fe^{55} spectrum 163
6.57 Post irradiation comparison of CCDs: Variation of post irradiation performance with temperatures - Zero peak of Fe^{55} spectrum164
6.58 Fe^{55} Spectrum recorded using an irradiated CCD - Mn Kα and Mn Kβ peaks are seen- measured 12 months after irradiation - at -30° C 166
6.59 Fe^{55} Spectrum recorded using an irradiated CCD - Mn Kα and Mn Kβ peaks are seen- measured 20 months after irradiation - at -30° C 166
6.60 Figures depicts the dependence of resolution of the devices on temperature before and after irradiation 167
6.61 Comparison of device performance pre-irradiation, post irradiation and post annealing 169
6.62 Variation in the measurement of ΔFWHM at two different temperatures. 169

List of Tables

6.1 p-n Junction - Photon irradiation data 112
6.2 PN Junction-Electron Irradiation data 115
6.3 Photon irradiation-zener diode 121
6.4 Electron irradiation-zener diode 121
6.5 CCD irradiation data-pre and post irradiation, post annealing . 167
6.6 CCD annealing data-in different annealing period 168

Chapter 1

Radiation Environment of Space

To fulfill any space mission science objective, electronic instrumentation for data acquisition and electronic control equipments are inevitable. These electronic devices are prone to space radiation damage. In order to understand the possibilities of damage to electronic devices, it is important to understand the nature and type of radiation in the space. Since the trajectory and mission period of the space vehicles are predetermined, it is possible to determine the amount / dose of radiation, the device may be exposed in the space. There are several models exist which map various type of space radiation in different region of space and different period of time. [1]-[3]. In the case of lunar mission, the main source of radiation is the trapped radiation in the radiation belt of earth and the solar protons during the mission period.

In the low earth orbit having altitude less than 2,000 km and the Sun Synchronous Orbit, where the altitude is in the range of 700-800 km, the main source of radiation is from the trapped radiation.

The Highly Elliptical Orbit will have both trapped and non-trapped radiation. The reason being that, the orbit has a low altitude perigee and high altitude apogee. The Geocentric Earth Orbit of altitude 36,000 km and the transfer orbit to the moon will have both trapped and non-trapped radiation. The path of interplanetary travel will have the non-trapped radiation. In addition to the main sources, there may be secondary sources of radiation.

1.1 The Trapped Radiation

Cosmic radiations are the intense radiation in space. Even though, the major component being the photons, cosmic rays will have ions of all the atoms in the nature. In addition to the main particles, they produce showers of secondary particles when they reach the atmosphere of earth. The magnetosphere of earth can trap charged particle passing through it forming what is called 'radiation belt of earth'. The radiation belt of earth was first detected by Ex-

plorer I mission by Van Allen and his team with their cosmic ray detection instrument launched onboard Explorer I and the radiation belt is known after his name,"The Van Allen belt". The distribution of the charged particle and the type of charge particle varies depending on the charge of particle and magnetic field strength of various regions of the belt. The particle trajectory is a spiral path and advance along the magnetic field lines between north and south poles. The particles drift in the east or west direction near the poles depending on the charge of the particles. Electron drift towards east and protons drift towards west. During their drift, electrons and protons collide in the atmosphere producing auroras observed at the poles. [4]

In some region of the belt, protons are dominated while some other region will have electron domination. The radiation in the radiation belt has been modeled . NASA AP8MAX is a modeling code for proton fluxes during solar maximum and AP8MIN model for proton fluxes during solar minimum. AE8MAX is a similar modeling code for electron fluxes for solar maximum and AE8MIN for solar minimum conditions. The community coordinated modeling center, allow citizens to request a run on the web , specifying the entry parameters, for trapped radiation model and filtering the output flux based on several parameters [5]. A description of the model is given in Ginet, G.P. *et al.*, 2013 (DOI:10.1007/s11214-013-9964-y). The community co-ordinate modeling center can be found at https://ccmc.gsfc.nasa.gov/modelweb/models/trap.php.

The stability of the earth radiation belt is affected by space storms which may drain the particles from Van Allen Belts. There were instances, in which case the Van Allen Belt has moved much closer to earth two times in 2003. As a result of this, space craft has suffered exposure much higher than that expected[6]. Hence we must account the worst case in calculating the expected dose to space craft during the mission.

Modulation of cosmic ray intensities and drift in the South Atlantic Anomaly were observed over the period of solar cycle has been observed by CREAM and CREDO measurements [7]-[8]

South Atlantic Anomaly (SAA) is another phenomenon, explained below, which is of great concern to space craft and even to aircrafts. Hence, it is good that the orbit of the space craft to avoid frequent exposure to the SAA and auroral horns . The performance of SMART-1 was deteriorated to large extend when it arrived at moon spending nearly 18 months within the earth's radiation belt.

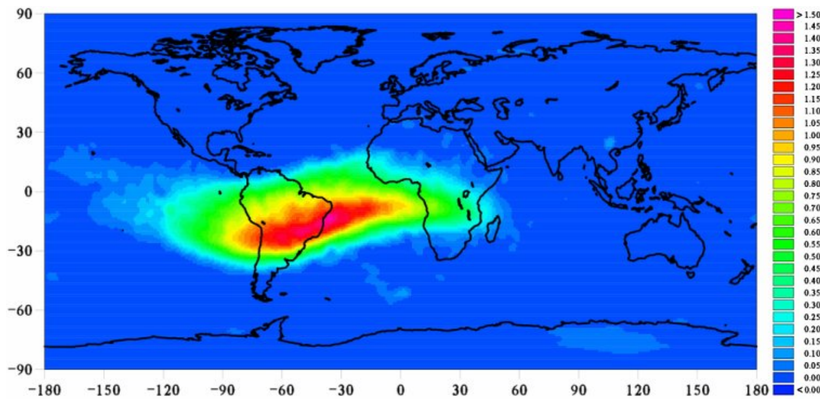

Figure 1.1: Jason-1 exposure to South Atlantic Anomaly effects, measured on 200-2004 period using the Doris ultra-stable oscillator. (Credits Cnes/CLS)

1.2 South Atlantic Anomaly & Auroral Horns

The magnetic field of earth is weaker near south pole due to the asymmetry of earth's magnetic axis about rotational axis. Hence the radiation belt near the south pole extend closer to that of the surface of earth. This effect is more pronounced near the south atlantic region, as shown in figure 1.1, and hence known as South Atlantic Anomaly (SAA). AP-8MAX and AE-8 MAX can be used to model South Atlantic Anomaly for trapped proton flux and trapped electron flux.

1.3 Non-Trapped Radiation

Non-trapped radiation include radiation originated from the sources other than that from trapped radiation. Radiation from the sun such as solar protons and radiation from other areas of galaxy and that from outside galaxy such as cosmic rays include the non-trapped radiation.

1.4 Cosmic Rays

The origin of the galactic cosmic rays is believed to be from the stars and later got accelerated by the shock waves from supernova explosions. Galactic cosmic rays consist mostly of protons (85%). The remaining are mostly alpha particles. 1 % of cosmic rays include moderate nuclides ($4< Z< 26$). The energy of the cosmic ray particles may be as high as 10^{20} eV. But the particles in the GeV range have most influence on instrumentation electronics. [9].

Solar cosmic rays are different from the galactic cosmic rays in that, they originate from the solar events or solar flares and from the solar wind ejected from the sun. The solar wind consists of protons and electrons of energy in

the range of few MeV. During high solar activity, sun's magnetic field causes galactic cosmic rays to loose some of its energy. Hence, the galactic particles peak at the solar minimum.

1.5 Solar Flare

The entire range of radiation in electromagnetic spectrum is emitted by the sun during the solar flare. During solar maximum, the intensity of solar flare increases. The X-rays from solar flare can cause X-ray fluorescence from the elements on the surface of the moon. This X-ray fluorescence is detected by X-ray fluorescence detectors such a scientific CCD. Depending on the intensities, the peaks are classified as A, B, C,M or X . The fluxes are recorded by Geostationary Operational Environment Satellites (GOES 10 and 12). Nov 2003 X45 flare being the largest flare recorded.[10].

In addition emission of electromagnetic rays there are Coronal Mass Ejections (CME). Sun ejects protons, electrons and heavy ions in smaller quantities. It is the protons that cause damage to CCD, while electrons and heavy ions from sun are not significant in damaging CCD. These are the major component of exposure and largest concern of transiting space craft.

Solar proton events observed, follow a Solar X-ray peak, with a delay ranging from 15 minutes to 30 minutes. Solar proton events may be modeled using JPL solar energetic particle model.

Bibliography

[1] Boscher, D. M., S. A. Bourdarie, R. H. W. Friedel, and R. D. Belian (2003), A model for the geostationary electron environment: POLE, IEEE Trans. Nucl. Sci., 50(6), 2278 – 2283, doi:10.1109/TNS. 2003.821609.

[2] Gussenhoven, M. S., E. G. Mullen, and D. H. Brautigam, Improved Understanding of the Earth's Radiation Belts from the CRRES Satellite, IEEE Trans. Nucl. Sci., 43, 353-368, 1996a.

[3] Heynderickx, D., M. Kruglanski, V. Pierrard, J. Lemaire, M. D. Looper, and J. B. Blake, A Low Altitude Trapped Proton Model for Solar Minimum Conditions Based on SAMPEX/PET Data, IEEE Trans. Nucl. Sci., 46, 1475, 1999

[4] Birkeland, Kristian (1908). The Norwegian Aurora Polaris Expedition 19021903. New York: Christiania (Oslo): H. Aschehoug & Co. p. 720. out-of-print, full text online

[5] Heynderickx, D., J. Lemaire, E. J. Daly, and H. D. R. Evans, Calculating Low-Altitude Trapped Particle Fluxes With the NASA Models AP-8 and AE-8, Radiat. Meas., 26, 947-952, 1996b.

[6] Horne et al; Wave acceleration of electrons in the Van Allen radiation belts. Nature 437, 227-230 (8 September 2005) — doi: 10.1038/nature03939

[7] "Implication for Space Radiation Environment models from CREAM and CREDO measurements over half solar cycle" C S . Dyers etal ; Radiat Meas (1999)

[8] Dyer, C., Sims, A. and Underwood, C. (1996) Radiation Belt Observations from CREAM and CREDO, in Radiation Belts: Models and Standards (eds J.F. Lemaire, D. Heynderickx and D.N. Baker), American Geophysical Union, Washington, D. C.. doi: 10.1029/GM097p0229

[9] C.S. Dyer, P.R. Truscott Cosmic radiation effects on avionics . Elsevier. Microprocessors and Microsystems. Volume 22, Issue 8, 22 February 1999, Pages 477483

[10] Neil R Thomson, Craig J Rodger, Mark A. Clilverd (2005) Large solar flares and their ionospheric D region enhancements; AGU Publicaation, Journal of Geo-Physical Research, Volume 110, Issue A6, June 2005 June 2005

Chapter 2

Interaction of Radiation with Matter

2.1 Interaction of Photons with Matter

High energy photons interact with matter resulting in one or more of the following process

a) Photoelectric effect

b) Compton effect

c) Pair production

A discussion of the interaction of particle radiation with matter require the introduction of the concepts of quantum mechanical as well as semi-classical theory of scattering. They have been made use in explaining many physical phenomenons emerging from the interaction of radiation with matter. Hence, a discussion of scattering theory is helpful.

2.1.1 Scattering

There are elastic and inelastic scattering.

Elastic scattering

Since there is no loss of energy in-elastic scattering, The scattered energy of the gamma ray will be the same as the incident energy except for a small recoil energy taken up by the atom. There are four types of elastic scattering.

1. Rayleigh Scattering

   In Rayleigh scattering, the photon is scattered by the atom as a whole. In this process, all the electrons in the atoms participate in a coherent manner and hence called coherent scattering. No energy is transferred to the medium. The atoms are neither excited nor ionized and only the direction of the photon is changed. At relatively high energies of X-rays and gamma rays Rayleigh scattering is very small and neglected for most purposes.

2. Thomson Scattering

   Thomson scattering is the scattering of electromagnetic radiation by the charged particle. The electric and magnetic field component of the incident wave accelerates the particle. As they are accelerated, they emit radiation and thus wave is scattered.

3. Delbruck Scattering

   It is also known as elastic nuclear potential scattering. This is due to the virtual electron pair formation in the field of nucleus. This effect is very small at low energies.

4. Nuclear Resonance Scattering

   This type of scattering involves excitation of nuclear levels by incident photons, with subsequent re-emission of excitation energy.

Scattering theory

The interaction of radiation with matter can be considered as the problem of scattering. During the process of scattering the system consisting of the matter (target) and incoming particle in the initial state will undergo a transition and the system changes in to final state. The state of the outgoing particle is influenced by the potentials and fields of the particles in the system. This problem is solved using time dependent perturbation theory.

In the scattering process, since the particles is approaching the target, in a path where the potential is variable, the interaction Hamiltonian also varies as a function of time. The probability of the change of state (scattering) from initial state to final state may be written as:

$$P_{SC} = | < f|U_I(t)|i > |^2 = | < f|(\mathbf{1} - i\int_{-\infty}^{\infty} V_I(t')dt' + ...)|i > |^2 \qquad (2.1)$$

Where the propagator U_I is called scattering matrix S. Assuming V to be time independent, The first order perturbation theory will yield

$$< f|S^1|i >= -iV_{fi}\int_{-\infty}^{\infty} \exp(i\omega_{fi}t)dt = -2\pi i\delta(\omega_f - \omega_i)V_{fi} \qquad (2.2)$$

The second order contribution is given by:

$$< f|S^2|i >= -2\pi i\delta(\omega_f - \omega_i)\sum_m \frac{< f|(V|m >< m|V)|i >}{\omega_f - \omega_i} \qquad (2.3)$$

A more general pattern that emerge from the above equations for the first order and second order scattering matrix, above is

$$< f|S|i >= -2\pi i\delta(\omega_f - \omega_i) < f|T|i > \qquad (2.4)$$

where, T is the scattering matrix.

$$< f|T|i >=< f|V|i > + \sum_m \frac{< f|(V|m >< m|V)|i >}{\omega_f - \omega_i} + ...; \qquad (2.5)$$

The probability of scattering shall be, $P_S = 4\pi^2 < f|T|i >^2 \delta^2(\omega_f - \omega_i)$; Using the definition of the Dirac delta function and integrating, we write,

$$\delta^2\omega = \frac{1}{2\pi}\int_{-\infty}^{\infty} dte^{i\omega t}\delta(\omega) = \lim_{t\to\infty}\frac{t}{\pi}\delta(\omega) \qquad (2.6)$$

Hence,

$$P_S = \lim_{t\to\infty} 4\pi t < f|T|i >^2 \delta(\omega_f - \omega_i) \qquad (2.7)$$

The rate of scattering is defined as $W_s = P_S/(2t)$
Where, $2\pi < f|T|i >^2 \delta(\omega_f - \omega_i)$; For a continuum of final states with a density of state $\rho(\omega_f)$, we need to integrate the expression for the isolated final state above, to write as :

$$W_s = 2\pi \int 2\pi < f|T|i >^2 \delta(\omega_f - \omega_i)\rho(\omega_f)d\omega_f = 2\pi \, |< f|T|i >|^2 \, \rho(\omega_i) \quad (2.8)$$

(This is Fermi's Golden rule).

Scattering cross section

Scattering cross section may be defined as the ratio of the rate of scattering to the incoming flux of particles.

ie., $\frac{d^2\sigma}{d\Omega dE} \propto \frac{W_s(\Omega,E)}{\Phi_{inc}}$;

The system consists of two entities. The incoming particles and the medium. If the incoming particle is some radiation of momentum $\overline{k}$, The unperturbed Hamiltonian for the system is,

$H_0 = H_R + H_M$

When time $t = \mp\infty$, the two systems are separate with separate eigen states given by:

$|i >= |k_i, m_i >$; and $|f >= |k_f, m_f >$; with energies $H_R|k_i >= \hbar\omega_i|k_i >$; $H_R|k_f >= \hbar\omega_f|k_f >$, $H_M|m_i >= \varepsilon_i|m_i >$; and $H_M|m_f >= \varepsilon_f|m_f >$;

where the total energies are given by: $E_i = \hbar\omega_i + \varepsilon_i$ and $E_f = \hbar\omega_f + \varepsilon_f$.

Rate of scattering

The rate of scattering is given by the expression above as

$W_{fi} = 2\pi < f|Ti >^2 \delta(E_f - E_i)$.

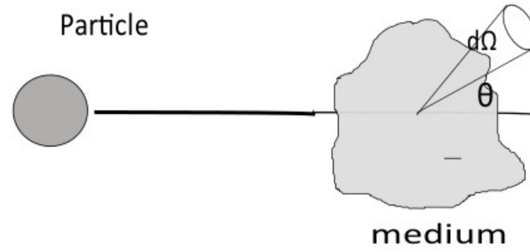

Figure 2.1: Scattering of particles

Since state of radiation changes as a continuum while that of the medium (target) is left in one or more definite states, there must be a distinction between the change of states of the two systems. Hence, the final state is separated in to two sub systems. The partial projection of radiation states alone can be written as $T_{K_f,K_i} =< K_f|T|K_i >$. To make the sense of continuum, we write the delta function as an integral of exponentials,

$$W_{fi} = \frac{2\pi}{\hbar} < m_f|T_{K_f,K_i}|m_i >< m_i|T^{\dagger}_{K_f,K_i}|m_f > \frac{1}{2\pi\hbar}\int_{-\infty}^{\infty} e^{i(\omega_f-\omega_i)t} e^{i(\varepsilon_f-\varepsilon_i)t/\hbar} \quad (2.9)$$

Since, $e^{-H_Rt/\hbar}|m_i >= e^{-\varepsilon_i t/\hbar}|m_i >$ (also holds good for m_f also)

$$< m_f|T_{K_f,K_i}|m_i > e^{i(\varepsilon_f-\varepsilon_i)t/\hbar} =< m_f|e^{H_Rt/\hbar}T_{K_f,K_i}e^{-H_Rt/\hbar}|m_i >=< m_f|T_{K_f,K_i}(t)|m_i(2.10)$$

Hence, the expression for the rate of scattering becomes

$$W_{fi} = \frac{1}{\hbar^2}\int_{-\infty}^{\infty} e^{i(\omega_f-\omega_i)t/\hbar} < m_i|T^{\dagger}_{K_f,K_i}(0)|m_f >< m_f|T_{K_f,K_i}(t)|m_i > \quad (2.11)$$

This is the expression for the rate as a correlation of transition of events. In terms of final density of states the average rate of scattering, could be written as

$\overline{W_s} = \Sigma_f W_{fi}\rho(E)dEd\Omega$; where $(E) = (\frac{L}{2\pi})^3\frac{k}{\hbar^2} = (\frac{L}{2\pi})^3\frac{\sqrt{2mE}}{\hbar^3}$; the symbols have the usual meaning. The summation is performed, considering that the target is left in more than one final state.

The incoming flux is defined as the number of scatterer per unit area in unit time.

$\Phi = \frac{N}{At}$;
Since $t = \frac{L}{\upsilon}$; in a region of length L, the flux $\Phi = \frac{\upsilon}{L^3}$.
For photons $\Phi = \frac{\upsilon}{L^3}$;
For massive particles like neutrons $\upsilon = \frac{\hbar k}{m}$, hence $\Phi = \frac{\hbar k}{mL^3}$;

Scattering of photons by atoms

In this process, the incoming photons interact with atom to get an outgoing photon. The Hamiltonian corresponding to quantized electromagnetic field is :

$H = \frac{P^2}{2m} + \hbar\omega(n+\frac{1}{2}) = \frac{1}{2m}(p - \frac{eA}{c})^2 + \hbar\omega(n+\frac{1}{2})$; The interaction Hamiltonian can be separated to write as $H = H_0 + V = \frac{P^2}{2m} + \hbar\omega(n+\frac{1}{2}) + [-\frac{e}{2mc}(p.A + A.p) + \frac{e^2}{2mc^2}A^2]$; where V is the quantity in the square bracket .

If the interaction involves many electrons , the interaction Hamiltonian is $V = \Sigma_i - \frac{e}{2mc}(p_i.A(r_i) + A(r_i).p_i) + \frac{e^2}{2mc^2}A(r_i)^2$

The scattering transition rate is given by $W = \frac{2\pi}{\hbar}|K_1^2 + K_2^1|^2\rho(E_f)$ where, K_1^2 is the second order contribution from $V_1 = -\frac{e}{2mc}\Sigma_i p_i.A$ and K_2^1 is the first order contribution from $\frac{e^2}{2mc^2}\Sigma_i A_i^2$

Scattering : A semi- classical picture

Classically, scattering may be viewed as the effects of interaction of electromagnetic wave with an oscillating dipole. We take the frequency of electron attached to atom to be ω_0. The additional force exerted on the electron due to electromagnetic wave is $F = eE(t)$, $E(t)$ being the oscillating electric field $E_0\sin(\omega t)$

The equation of motion of electron is

$$m_e\ddot{x}_e = -kx_e - eE(t) \rightarrow \ddot{\ddot{x_e}} + \omega_0^2 = -\frac{e}{m_e}E(t)$$

The solution to this equation can be written in the form $x_e(t) = A\sin(\omega t)$. Then we have the equation $(-\omega^2 + \omega_0^2)A = -\frac{e}{m_e}E(0)$

ie.,

$$A = \frac{1}{(\omega^2 - \omega_0^2)}\frac{e}{m_e}E(0)$$

The power radiated due to accelerated charge is given by $P = \frac{2}{3}\frac{e^2}{c^3}a^2$ where the acceleration is given by:

$a = -\omega^2\sin(\omega t)$; Substituting for a, we get the radiated power as:

$$P = \frac{1}{3}(\frac{e^2}{m_ec^2})^2\frac{\omega^4}{(\omega_0^2 - \omega^2)^2}cE_0^2$$

In terms of cross section the radiated power can also be written as $P = \sigma I_0$; where I_0 is the radiation intensity, given by $I_0 = \frac{cE_0^2}{8\pi}$

Hence, the cross section for interaction of electromagnetic field with atom (expressed in SI units) is given by: $\sigma = 4\pi r_e^2\frac{2}{3}(\frac{\omega^2}{(\omega_0^2 - \omega^2)})^2$.

2.1.2 Photo electric effect

Photoelectric effect is the ejection of electrons from an atom by a photon above threshold frequency. Consider that the atom has atomic number Z with differential cross section $\frac{d\sigma}{d\omega} = \frac{W_{fi}}{\phi_{inc}}$ where W_{fi} is the rate of scattering and ϕ_{inc} is the

incoming flux. As explained above,

$$\phi = \frac{number of protons}{time \times area} = c/L^3$$

where L^2 is the area and $t = L/c$. As per Fermi Golden rule,$W_{fi} = \frac{2\pi}{\hbar}\langle f|V|i\rangle^2\rho(E_f)$; Where, $\rho(E_f)$ is the density of states in terms of the momentum of the scattered electron. The density of states of electrons is given by the density of the momentum states in the cavity L^3. Since, $\rho(E_f)dE_f = \rho(p)d^3p = (\frac{L}{2\pi\hbar})^3p^2dpd\Omega$.
Putting, $E_f = \frac{p^2}{2m}$, we get $dE_f = \frac{pdp}{m}$.
Hence,

$$\rho(E_f) = (\frac{L}{2\pi\hbar})^3 mpd\Omega. \tag{2.12}$$

To calculate the transition matrix element$\langle f|V|i\rangle$,where

$$V = -\frac{e}{mc}\vec{A}.\vec{p}. \tag{2.13}$$

The photon eigen states are $|1_{k\lambda}\rangle$ and $|0_{k\lambda}\rangle$ that of the electron momentum eigen states in position representation are $\psi_i(\vec{r}) = \langle\vec{r}|i_e\rangle$ and correspondingly $\psi_f(\vec{r}) = \langle\vec{r}|f_e\rangle$.
The matrix element between the initial and final states of electron and photon is then

$$V_{if} = -\frac{e}{mc}\langle f_e|\langle 0_{k\lambda}|\Sigma_{h\xi}\sqrt{\frac{2\pi\hbar c^2}{L^3\omega_h}}[a_{h\xi}e^{i\vec{h}r} + a_h^{\dagger}\xi e^{-i\vec{h}r}]\epsilon_{h\xi}.\vec{p}|1_{k\lambda}\rangle|i_e\rangle \tag{2.14}$$

$$V_{if} = \Sigma_{h\xi}\frac{e}{m}\sqrt{\frac{2\pi\hbar}{L^3\omega_h}}\langle f_e|(0_{\vec{k}\lambda}a_{h\xi}1_{\vec{k}\lambda}\rangle + \langle 0_{\vec{k}\lambda}a_{h\xi}1_{\vec{k}\lambda}\rangle e^{-i\vec{h}.r})\epsilon_{h\xi}.\vec{p}|i_e\rangle \tag{2.15}$$

Only one term is surviving , which is for (h=k and $\xi = \lambda$)

$$V_{if} = -\frac{e}{m}\sqrt{\frac{2\pi\hbar}{L^3\omega_k}}\langle f_e|e^{ik.r}\epsilon_{k\lambda}.\vec{p}|i_e\rangle \tag{2.16}$$

The position representation of $|i_e\rangle$, $|f_e\rangle$ and the momentum operator, we get

$$\langle f|V|i\rangle = -\frac{e}{m}\sqrt{\frac{2\pi\hbar}{L^3\omega_k}}\int_V d^3\vec{r}\Psi_f^*(\vec{r})e^{ik.r}\epsilon_{k\lambda}(-i\hbar\nabla\Psi_i(\vec{r})) \tag{2.17}$$

For hydrogen like atoms,the initial bound state wave function $\Psi_i(\vec{r})$is given by $\frac{e^{-|r|}/a}{\sqrt{\pi a^3}}$;

The final wave function is a plane wave with momentum $\vec{q} = \vec{p}/\hbar$; and the volume $V = L^3$

$$\langle f|V|i\rangle = -\frac{e}{m}\sqrt{\frac{2\pi\hbar}{L^3\omega_k}}\frac{1}{\sqrt{L}^3}\int_V d^3\vec{r}\Psi_f^*(\vec{r})e^{i(k-q).r}\epsilon_{k\lambda}(-i\hbar\nabla\frac{e^{-|r|}/a}{\sqrt{\pi a^3}}) \quad (2.18)$$

Put $\triangle\vec{k} = \vec{k} - q$; and evaluate the integral: $\int_V d^3\vec{r}e^{i\triangle\vec{k}.r}\epsilon_{k\lambda}\nabla\Psi_i$ by parts.
$\int_V d^3\vec{r}e^{i\triangle\vec{k}.r}\epsilon_{k\lambda}\nabla\Psi_i = e^{i\triangle\vec{k}.r}\Psi_i|_{L^3} - i\Delta\vec{k}\epsilon_{k\lambda}\int d^3\vec{r}e^{i\nabla\vec{k}.r}\Psi_i(\vec{r})$
Since the wave functions should vanish at the boundaries, the first term will vanish. Putting $\triangle\vec{k}.r = \triangle kr\cos\vartheta$ as usual,

$$i2\pi\triangle\vec{k}\epsilon_{k\lambda}\int drr^2\Psi_i(\vec{r})\int_0^{2\pi} e^{\triangle kr\cos\vartheta}\sin\vartheta d\vartheta = -i\frac{\triangle\vec{k}\epsilon_{k\lambda}}{|\triangle\vec{k}|}\int_0^\infty dr\Psi_i(\vec{r})r\sin(\nabla\vec{k}.r) \quad (2.19)$$

Here the limits have been extended from zero to infinity under the assumption that $L >> a$;

$$\langle f|V|i\rangle = -\frac{e}{mL^3}\sqrt{\frac{2\pi\hbar}{\omega_k}}(-i\hbar)(-i\frac{\triangle\vec{k}\epsilon_{k\lambda}}{\triangle\vec{k}}\sqrt{\pi a^3}\int_0^\infty e^{-r/a}rsin(\nabla\vec{k}.r) \quad (2.20)$$

Which on integration (using the identity $\int_0^\infty e^{-r/a}rsin(br)dr = \frac{2a^3b}{(1+a^2b^2)^2}$) will yield:

$$\langle f|V|i\rangle = \frac{e2\pi\hbar}{mL^3}\sqrt{\frac{2\hbar a^3}{\omega_k}}\frac{\triangle\vec{k}\epsilon_{k\lambda}a^3}{(1+a^2\triangle\vec{k}^2)^2} \quad (2.21)$$

$$\frac{d\sigma}{d\Omega} = \frac{32e^2a^3q(\vec{q}.\vec{\epsilon_k})^2}{mc\omega_k(1+(a^2\triangle\vec{k}^2))^4} \quad (2.22)$$

When the energy of the incoming photon is much less than electron binding energy, we have $a\triangle k \gg 1$. Hence, the scattering cross section may be written as:

$$\frac{d\sigma}{d\Omega} = \frac{32e^2a^3q(\vec{q}.\vec{\epsilon_k})^2}{mc\omega_k(a^2\triangle\vec{k}^2)^4} \propto a^{-5} \quad (2.23)$$

Here,a is the Bohr radius which has Z^{-1} dependance. Hence, the photo electric effect cross section has Z^5 dependance.

2.1.3 In-elastic or Incoherent scattering.

Compton scattering

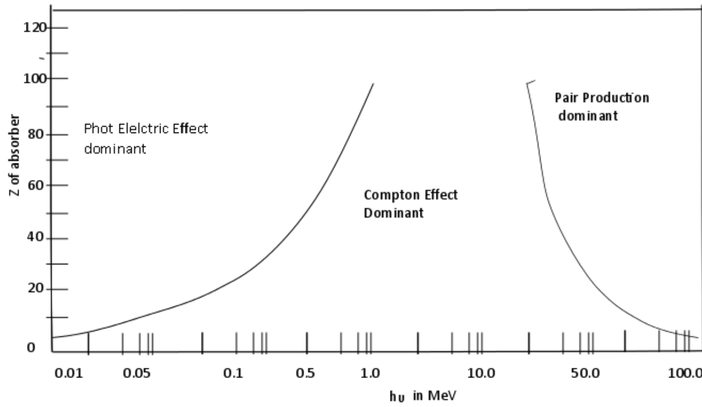

Figure 2.2: Relative importance of three major types of gamma ray interactions. (R D Evans, The atomic nucleus, Mc.Graw-Hill Book Company)

In Compton effect, the incident X-ray or gamma ray will transfer some of its energy to the bound electrons in is known as Compton Shift. The principle of conservation of energy and momentum help us to deduce the relationship between the energy transfer and scattering angle for a given interaction and is given by:

$$h\nu' = \frac{h\nu}{1 + \frac{h\nu}{m_0c^2}(1 - cos\theta)} \tag{2.24}$$

where m_0c^2 is the rest mass energy of the electron 0.511 MeV and θ is the scattering angle . The probability of Compton scattering per atom of the absorber depends on the number of electrons available at scattering targets and therefore increases nearly with atomic number (Z). The differential cross section for the process is given by the formula obtained by Klein and Nishima predicts that at a given angle, the cross section decreases with increase in photon energy. ie;

$$d\sigma/d\Omega = r_0^2[\frac{1}{1 + \alpha(1 - cos\theta)}]^3(\frac{1 + cos^2\theta}{2}.\frac{1 + \alpha^2(1 - cos\theta)^2}{(1 + cos^2\theta)(1 + \alpha(1 - cos\theta} \tag{2.25}$$

where $\alpha = \frac{h\nu}{m_0c^2}$ and r_0 is the classical electron radius. The total cross section can be expressed as $\sigma = \int_0^\pi \frac{d\sigma}{d\Omega} 2\pi sin\theta d\theta$

The relative importance of each of the above process is represented in figure 2.2.

The three major types of gamma ray interaction are:

2.1.4 Photo nuclear interaction

Pair production

The process of pair production describes transformation of a photon in to an electron-positron pair. In order to conserve momentum, this can only occur in the presence of a third body, usually a nucleus. More over, to create a pair, a photon must have at least energy of 1.022 MeV. The excess energy carried by the photon above 1.022 MeV gets converted to the kinetic energy of the electrons and positrons so created. Practically, pair production is significant for energies twice that of this energy. Hence, pair production is predominantly confined to high energy gamma rays. The cross section of pair production varies as Z^2 [1]

If atoms are neither excited nor ionized during pair production, then it is called elastic pair production. If the atomic electrons are excited, the process is called inelastic pair production. If the atom is ionized, then the process is known as triplet pair production.

Photonuclear absorption

In photonuclear absorption process, the incoming gamma ray interacts with the nucleus of the absorber atom and the nucleus will be excited leading to subsequent disintegration of the nucleus through emission of nuclear particles or radiation. This is also known as nuclear photodisintegration. It starts typically about 10 MeV. The cross section for this process is generally negligible compared to the photo electric effect as the dimension of the nucleus is very small compared to the atomic size.

Photo meson production

In the presence of nucleus high energy gamma rays may cause production of meson. Meson production requires photon energies above 150 MeV. Even then cross section are negligible.

2.1.5 Gamma ray attenuation

The result of the above interaction is the loss of gamma ray quanta in the medium and hence, part of the gamma ray intensity will be lost on traversing through the medium. If I_0 is the intensity of the gamma ray before entering the medium, then after traversing a distance 'x' in the medium, its intensity would have reduced to I_x given by $I_x = I_0 e^{(-\mu x)}$, where μ is the absorption coefficient.

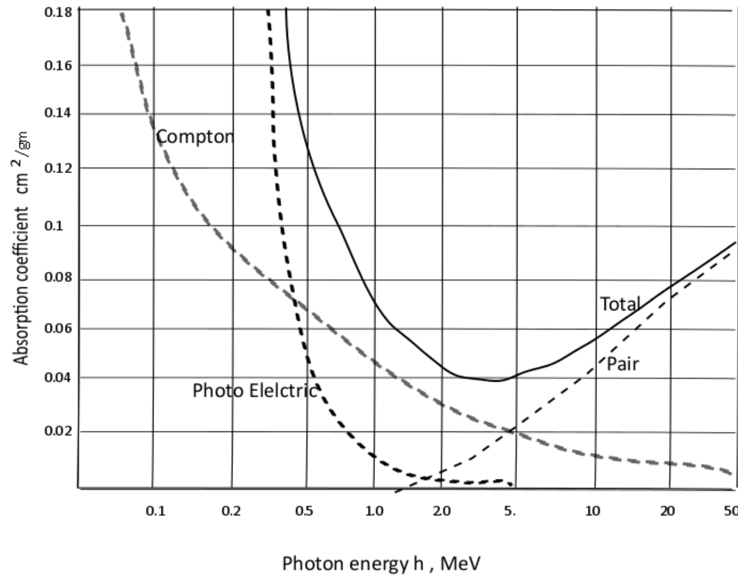

Figure 2.3: Contribution to total mass absorption coefficients from Photoelectric effect, Compton effect and Pair production. (H A Enge,1966, Introduction to nuclear physics, page 193, Addison Wasely Publishing(Co.))

The total attenuation of the photon is the sum of the contribution from the cross section of all process. $\sigma_{tot} = \sigma_{photon} + z.\sigma_{Compton} + \sigma_{pair}$ The relative importance of each of the above pair at different gamma ray energies is represented in Figure 2.3 Where we have multiplied compton cross section by Z to take in to account the 'Z' electron per atom.

$$\mu = N\sigma$$

$\mu = \sigma(\frac{N_a \rho}{A})$ where Na is the Avogadro's number, ρ is the density of the material and A is the molecular weight. This is more commonly known as Total Absorption Coefficient.

2.2 Interactions of Particles with Matter

Heavy charged particles such as alpha particles interact with matter primarily through coulomb forces between their positive charge and the negative charge of orbital electrons within the absorber atoms. Upon entering any absorbing medium the charged particle immediately interacts simultaneously with many electrons. The impulse, thereby, will excite the electron to higher energy state within the absorber atom (excitation) or the electron will be completely removed from the atom (ionization).

2.2.1 Stopping power

In each collision a part of the kinetic energy of the incoming particle will be transferred to the electron, the particle will lose its energy through successive collision in the absorber atoms as it traverse the thickness of the absorber. Finally the particle will be stopped in the absorber. The energy lost by the particle depends up on the energy of the incoming particle, charge states of the incoming particle as well as the absorber atoms and also on the excitation / ionization potential of the absorber atom. Energy lost by the particle as it traverse unit distance through the absorber is described as the specific energy loss $-(\frac{dE}{dx})$ and generally expressed as *stopping power* . The linear stopping power S for a charged particle in a given absorber is defined as the *differential energy loss* for that particle within the material divided by the corresponding differential path length and is given by Bethe's formula

$$S = \frac{-dE}{dx} = \frac{(z^2e^2NZ)}{(4\pi mE_0^2 meV^2)}[log_e\frac{(2MeV^2)}{h\nu} - log_e(1 - \frac{V^2}{C^2}) - \frac{V^2}{C^2}] \quad (2.26)$$

Where

V and E represents the velocity and energy of particle respectively
x is the distance travelled by the particle
e and Ze represents charge of electron and the particle respectively
m_e, is the electron rest mass; 'n' the charge density of target electrons
ρ the density of the material;
Z,A ,N_a is the atomic number , mass number and Avogadro number.

2.2.2 Range of charged particle

As the heavy charged particle moves through a medium, it excites and ionize the atoms that comes in to contact losing its kinetic energy in every successive collisions and finally stops in the medium after traveling through some distance. The distance traveled by the charged particle in the medium before it comes to rest is called the range of that particle.

2.2.3 Interaction of electrons

As energetic electrons approach the matter it will exchange its energy with bound electrons of the atoms and also with nucleus. Further, the energetic charged particle also lose its energy, by radiating energy in the presence of charged particle. Bethe equation gives the specific energy loss due to collision $-(dE/dx)$ is equal to

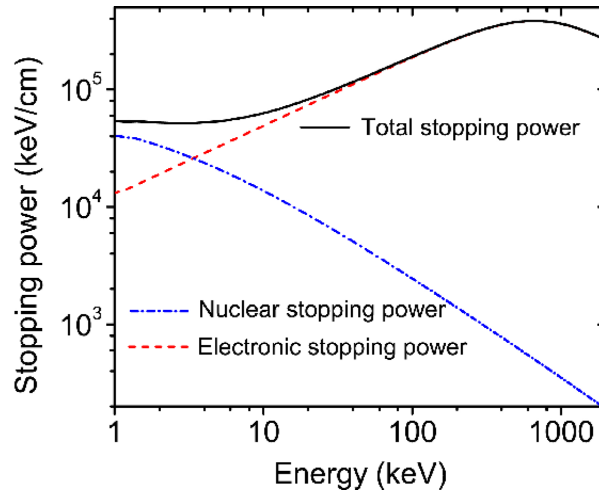

Figure 2.4: Stopping power. Nuclear and electronic contributions. NIST data. [www.nist.gov/pml/stopping-power-range-tables-electrons-protons-and-helium-ions]

$$\frac{2\pi e^4 NZ}{(m_0 v^2)}[ln\frac{m_0 v^2 E}{2I^2(1-\beta^2)} - ln2[2\sqrt{1-\beta^2} - 1 - \beta^2] + 1 - \beta^2 + 1/8\sqrt{1-\beta^2} \tag{2.27}$$

The symbols have usual meaning. Apart from this, electrons will be accelerated and deflected in the presence of a potential. This accelerated electron will radiate energy. The specific energy los by radiation emission is given by:

$$-(dE/dx) = \frac{NEZ(Z+1)e^4}{137 m_e^2 c^4}(4ln\frac{2E}{m_e c^2} - 4/3) \tag{2.28}$$

Hence, the total stopping power of the electrons will be the sum of the specific energy loss due to collision and that due to radiation

ie; $dE/dx = (dE/dx)_c + (dE/dx)_r$

Since, large deviation in the path is observed, definite range can not be defined. Relatively larger path length in the absorber is possible. This depends on the density of the absorber also. Therefore some of the elelctrons may even be scattered in the backward direction also.

Critical energy

The energy loss due to radiation strongly depends on the absorbing material. For each material we can define a critical energyE_c, at which the radiation loss equals the collision loss. Thus for $E = Ec, (dE/dx)_r = (dE/dx)_{coll}$ Above this energy, radiation loss will dominate over the collision - ionization losses and vice versa below E_c . An approximate formula for E_c is : $E_C = \frac{800}{(Z+1.2)}$ in MeV

Radiation length

Since the range of electron is not well defined, it is expressed as radiation length. Radiation length is the distance over which the electron energy is is reduced by a factor of 1/e due to radiation loss only.ie,

$$-dE/E = N\phi_{rad}dx \tag{2.29}$$

where $\phi_{rad} = 4Z^2r_e^2X[ln(183Z^{-1/3}) + 1/(18) - F(z)]$; where F(z) is a function of atomic nucleus. Considering the high energy limit where the collision loss can be ignored relatively to radiation loss,ϕ_{rad} is independent of E so that $E = E_0exp[\frac{-x}{L_{rad}}]$ Where x is the distance traveled and $L_{rad} = \frac{1}{N\phi_{rad}}$ is the radiation length. Using equation 2.29 we get,

$$\frac{1}{L_{rad}} = [4Z(Z+1)(\frac{\rho N_a}{A}]r_e^2x[ln(183Z^{-1/3}) + 1/18 - F(z)] \tag{2.30}$$

Bremsstrahlung

Electron with energies $\gg$ 1MeV will be radiating a considerable fraction of energy in the form of X-rays during inelastic collision with atomic nuclei. Bremsstrahlung, therefore, correspond to energy radiated per unit time in the form of electromagnetic radiation when a charged particle is moving with a very high speed ($\sim 3 \times 10^8$) m/s which may approach the velocity of light. In the case of electrons, when they are moving near the nucleus, their path will be slightly bent under the influence of nuclear field and give rise to emission radiation which is proportional to square of acceleration .

2.2.4 Positron interaction

Positrons loose energy in the same way as electrons. The coulomb forces, which constitute the major mechanism of energy loss for both electrons and heavy charged particles , are present for both positive and negative charges on the particle.

2.3 Interaction of neutrons

Neutron radiation is often called indirectly ionizing radiation. It does not ionize the atoms in the same way as protons, photon, or electrons do. However, neutron interaction may lead to the emission of gamma ray and nuclear particles through nuclear reaction and cause more ionization in other atoms. The interaction of neutron with nuclei induce the following reaction $(n,\gamma),(n,n),(n,p),(n,\alpha),(n,f)$ so that the out going fission fragments may

further interact with matter causing secondary interaction. They have more penetrating power asβ radiation. Intense bombardment with neutron creates dislocation in the materials leading to embrittlement or swelling of the metal and other materials. Fast neurons, having higher energy, are produced by nuclear process, such as nuclear fission. A thermal neutron is a free neutron with a most probable kinetic energy of ($\sim 0.025eV$). The average energy loss of energetic neutron in matter is called Lethargy(u) is given by $\overline{\Delta u} = \xi = \int_{E_0}^{E} ln\frac{E}{E'}P(E \rightarrow E')dE'$ Where E and E' are the energies before and after collision. The average increase in lethargy per collision is an important quantity which often appears in the calculation of slowing down of neutrons ie,

$F^{(i)}(E) = \sum_s^i(E)\phi(E) = \frac{\sum_s^i E}{\sum_s(E)}F(E)$ Where $\sum_s^i(E)$ is the macroscopic scattering cross section of the nuclei.$\sum_s(E)$ is the total macroscopic scattering cross section and $F(E)$ is the total collision density. The total collision density at E is therefore $F(E) = \sum_i \int_{\varepsilon}^{\varepsilon/\alpha i} \frac{(F^(i))(E')dE')}{(1-\alpha_i)E'}$ where$F^i(E')dE'$ collision with nuclei of the i^{th}type. α_i is the slowing down constant of the ith nuclei. Therefore,$\frac{(F^(i))(E')dE')}{(1-\alpha_i)E'}$ neutrons are scattered within the energy range dE per second.

Bibliography

[1] JR Greening , Fundamentals of Radiation dosimetry. 2nd Edition, Taylor and Francis, pp 15;

[2] MIT Open Courseware, https://ocw.mit.edu/courses/nuclear-engineering/22-51-quantum-theory-of-radiation-interactions-fall-2012/lecture-notes /MIT22_51F12_Ch.pdf

[3] V.K. Thankappan, Quantum Mechanics (Third Edition)ISBN 10: 812243357X / ISBN 13: 9788122433579, Published by New Age International (P) Limited, 2012

[4] Kenneth and Krane - Introductory Nuclear Physics, John Wiley and Sons.Inc. ISBN 0-471-80553-X (1988)

[5] Nicholas Tsoulfanidis and Sheldon Landsberger, Measurement and detection of radiation , 4 th edition, ISBN-10: 1482215497

[6] Glenn F. Knoll, Radiation Detection and Measurement, (Third Edition, 1999) John Wiley and Sons Inc. ISBN 10: 812243357X / ISBN 0-471-07338-5

Chapter 3

Radiation Effects in Materials

In this chapter, the effects produced by radiation on the material through interaction and thereby the changes in the various properties of the material are discussed. The extend of this defects depend on the nature, mass, charge, and the energy of the incident particle and the type of the material. The effects will be considerable, in the case of solids. In the case of crystals the orientation of crystal plane has significant effects. The effects produced in liquids and gases will be easily died out due to the relative random motion of the particle and the freedom of motion of the particle.

The interactions of gamma rays and electrons are primarily with electrons of the atom. The interaction with the nucleus is negligible. Heavy ions,ionize the atoms through electronic interactions and exchange relatively larger energy with the atoms in the solid and dislodge the atoms from the crystal lattice. This will, in turn, change the electrical, thermal and other physical properties of the material. This is called radiation damage. A neutron, however, does not interact with electrons, but, interact with the nucleus and produce secondary effects.

3.1 Effects of Interaction of Electromagnetic Radiation

High energy radiations like X-rays, gamma rays on interaction with crystals can produce considerable effects including the displacement of the atom from the lattice. Photo electric effect and Compton effect produce electron hole pair. Pair production causes enhancement in the electron positron pair density or a plasma in the electron path. This will cause additional electric charges and

electric pulses. Some of the electrons and holes will recombine in due course of time before being collected. In the case of polymers, it is found that, gamma rays can break the polymer chains or even the chemical bonding. Gamma rays also cause deformation and creation of additional side chains in polymers. Polymer properties are highly influenced by cross linking and the chain scission in the polymer introduced by the radiation. O.L Crutis [1]observed that the life time of the minority charge carriers are varying with energy density of the gamma radiation.

Thermo gravimetric analysis indicates that polymer decomposes by chain breaking and observed its activation energy on gamma radiation. Melting temperature, heat resistance, mechanical and structural properties are also changed. Seitz [2] was the first to apply in a systematic manner the collision theory to the evaluation of irradiation effects in solids. Seitz also calculated the minimum energy necessary to displace an atom in a typical solid and found to be around 25 eV. This displaced atom may also have kinetic energy and can induce further collision in other lattices.

3.2 Effects of Heavy ions

Heavy ions can impart relatively larger energy to produce secondary and tertiary effects. Low energy radiation will be generally dissipated within a few layers of surface atoms and the major effects will be surface damage. The surface damage can produce amorphization of the surface atom and considerably vary the surface properties. As the energy increase, the particle may travel deeper in to the material, loose its energy and get trapped in the material producing submerged guest atoms within the material. Atoms trapped in the deeper layer may even cause formation of nano clusters around the atoms. Further, this particle will produce interaction effects like displacement along the path of the particle. If the irradiation is done in the direction of crystalline axis, the particle can penetrate deep in to the crystal without producing much structural damage along the path of the particle. The interaction of electrons are also found to produce similar effects in materials. Basically, the above effects will be seen along the path of the particle in the form of electron hole pair due to ionization, energy deposition in crystals, molecular bond ruptures, atomic displacements etc.

The displaced atom usually has a considerable kinetic energy. When it moves

through the lattice it undergoes additional collisions with other atoms in the lattice. Since, the energy transferred in such collision is small, the result is simply a temporary effects of vibrational energy. But, if the energy transferred is considerable, then, additional secondary atoms may also be displaced. The secondary atoms in turn may displace tertiary atoms and so on. Eventually, all the kinetic energy of the original primary displaced atoms will be dissipated and a number of vacancy - interstitial pairs are formed. Kinchin and Pease [3] have proposed that the collision between a moving atom and a stationary atom may occur in the manner, such that, the originally stationary atoms get displaced and the moving atom is trapped in to the vacancy thus produced. These replacement collision will occur with a greater probability than normal displacements.

The particle dissipate its kinetic energy along its path during in-elastic collision without causing displacement of atom. Hence, temperature shoots up to a very high value along the path of the particle. This thermal spike is highly significant, if the moving particle is an atom or a fission fragment. Thermal spike may result in the annealing out of the defects previously introduced. This is the radiation annealing effect. It may also accelerate process such as diffusion. As a rule, they do not produce defect pairs.

Another kind of localized effects has been suggested by Brinkman [4] is the displacement spike. This is supposed to occur towards the end of the path of fast displaced atom or a fission fragment. Brinkman estimates that the mean free path of successive displacement is then comparable to, or even smaller than, the inter-atomic distance. As a result, a rapid succession of adjoining displacements occur and a substantial void is formed surrounded by a region of full interstitial atoms. This highly unstable configuration rapidly collapses with a result in melting or intermixing of atoms.

Still another notion has been introduced by Seitz , the plasticity spike. It occurs in conjunction with thermal or displacement spikes and is the result of stresses set up by the thermally expanded volume of spikes. A rough estimate indicates that these stresses may be sufficient to create new dislocation loops . However several such loops may cross each other and collapse in a random manner and a permanent plastic deformation in the material will remain.

The electronic excitation and ionization may lead to a variety of effects, depending on the material irradiated. As mentioned before, its influence in metals is practically nil, because of large supply of free electrons which heal up any effects produced. It may happen , however, that a fast electron is ejected by an

energetic X-ray and it in turn may produce atomic displacement.

In semi conductors the ionization effects may alter profoundly the carrier concentration by producing free electrons and holes. In dielectric material such as alkali halides, the electrons and holes are produced as evident from color center formation. A very interesting effect of the ionization in alkyl halide is the possibility of the formation of lattice defects without the occurrence of any collisions. This is evident from the rapid decrease of density of alkyl halide on irradiation with X-rays, which by themselves has much too low energy to displace atoms directly. Two mechanism for this effect have been proposed. One of them suggested by Seitz is based on the fact that an edge dislocation can be pictured as internal boundary of an incomplete plane of atoms in a crystal. In an alkali halide a pure edge dislocation is a sequence of positive and negative ions. Such a dislocation may have “jogs”. Jogs are incomplete plane bounded not by a straight line, but by a line with steps. These jogs are favorable to adding or removing ions from the incomplete plane. If an ion from an adjoining normal plane of ions is added to a jog, then a vacancy is formed and this vacancy can now diffuse away from the jog. Naturally each jog accepts alternatively positive and negative ions, Thus creating positive and negative ion vacancies in equal numbers.

Another mechanism has been suggested by Varley[5]. In this case, the ionizing radiation ionizes (perhaps through an Auger effect) a halogen atom, multiply. Thus, the originally negative ion become positively charged. Being surrounded by six positive metallic ions, it finds itself in an energetically highly unfavorable position and thus easily displaced to an interstitial site, in which, it presumably becomes neutralized. This mechanism leads clearly to the formation of negative ion vacancies and interstitial halogen atom.

An extremely important consequence of irradiation is, its influence on all processes which are diffusion controlled. Diffusion in solids, as is well known, depends on concentration of such lattice defects as vacancies and interstitial and on their mobility. It is clear that irradiation influences both. It increases the number of point defects above the equilibrium concentration, and also, through the heat energy released in thermal and displacement spikes, It may increase their local mobility. Since, lattice defects usually anneal out rapidly, the acceleration effect occurs mainly during irradiation, i.e., when defects are formed and disappear at a certain rate, a steady state of increased defect concentration is attained. It is clear that, accelerating effects , if any, will be predominant at low temperatures where the normal diffusion is hardly measurable. At high temper-

ature, the additional diffusivity will play a small role. Dienes and Damask [6] have analyzed, the nature of enhancement of diffusion, with various mechanism of defect elimination. It appears that, if the defects anneal out by migrating to surface or dislocation, then the enhanced diffusion is directly proportional to defect generating flux. On the other hand, if the predominant effect is defect recombination, ie., interstitial falling in to vacancies, then enhancement is proportional to the square root of the flux.

In the absence of other radiation, however, gamma irradiation may produce well-measurable effects in metals. The transmission of momentum is negligible by the direct scattering of electromagnetic radiation on atoms.

3.3 Illustrative Example

3.3.1 Metals

Studies of irradiation of metals are particularly suitable for their evaluation of point defect concentration. This kind of defect affect electrical resistivity. It appears that, each defect pair contributes a certain amount to the total resistivity. For instance, 1% of defects would contribute about 3 micro-ohm cm to the resistivity of copper.

As a typical case the variation in resistivity with the beams flux for copper,silver and gold irradiated with a deuteron beam of 12 MeV is shown in figure 3.1 The slope of the curves is in agreement with the theory for three metals. The slight curvature can be explained in terms of small amount of radiation annealing. The main uncertainty besides, the exact theoretical value of the resistivity increase per defect, is the number of defect produced near the threshold energy, E_d . Usually, one assume that, if the energy, transferred in an elastic collision is less than E_d , no displacements are produced. But, if it is higher, then all such collision lead to displacements. Actually, a more refined theory should take in to account of the fact that the probability of a displacement is a rather slowly varying function of the energy and also that it will depend on the crystallographic orientation of the transmitted momentum. In fact, if the struck atom moves in a direction not too different, from a direction of closely packed atoms, then, even though its energy may be higher than E_d, it will transmit so much of it to its neighbors that it will not be displaced. This so-called “focusing effect”may play a significant role in comparing theory with experiment.

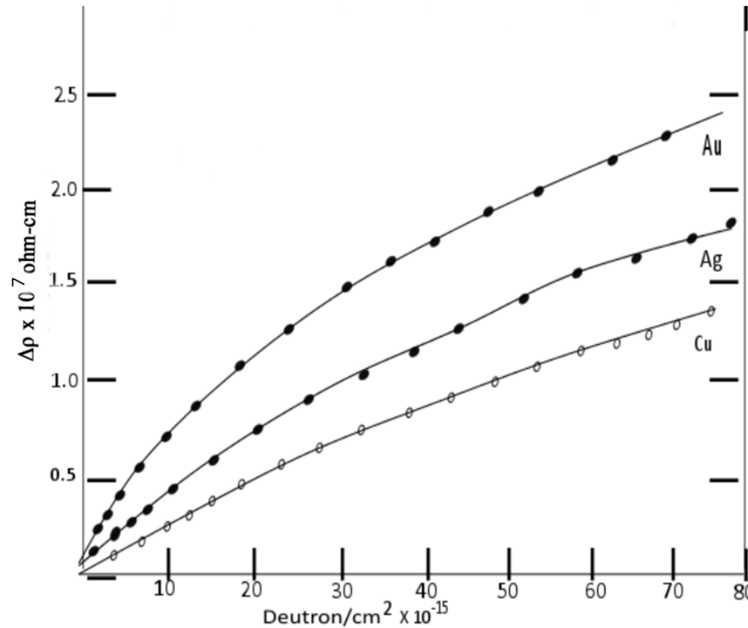

Figure 3.1: Variation of resistivity with deutron beam flux. ASTM technical publication, No 208, Sept.20,1956.

Figure.3.2 shows increase of the resistivity of a tungsten wire as a function of the energy, E, of its incident protons.[7]

When a pair of defects is formed in a metal, then the atoms surrounding a vacancy move in a little and an atom surrounding an interstitial atom move out considerably. As a result, the average lattice parameter as measured by X-rays is increased and the whole crystal undergoes expansion. All these effects anneal out on warming. Figure(3.3) shows the gradual decrease for the changes in length, in lattice parameter, and in resistivity of copper on heating. The striking effect is the rapid drop near 40° K and also the fact that, all three properties seem to be annealed out simultaneously. This indicates that they have the same origin. One may tentatively identify the various peaks corresponding to the recombination of interstitial and vacancies separated by progressively greater distance in the crystalline lattice.

It can be seen that, all the defects will be annealed out by the time the room temperature is reached. Actually, clusters of defects lead to exceedingly stable defects such as the, so-called, Cottrell-Lomer[8]-[9] dislocations or barriers. Thus defects can be removed only by slow diffusion processes and are stable up to the few hundred degrees above room temperature.

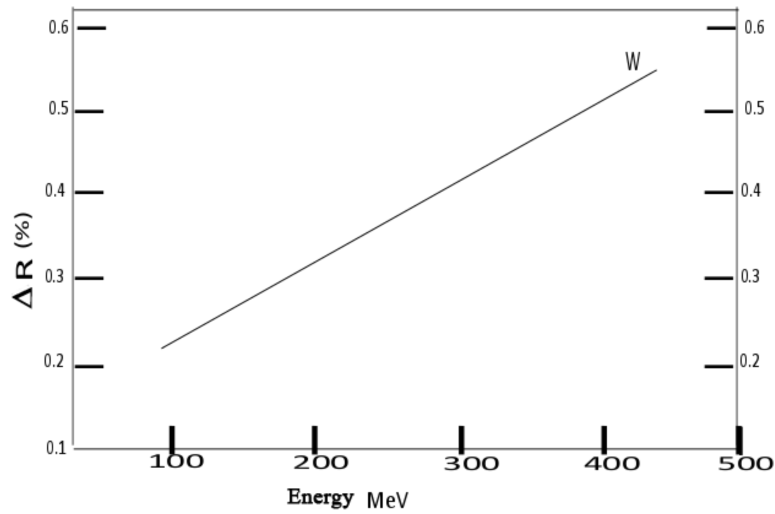

Figure 3.2: Increase of resistivity of of a tungsten wire with energy of beam flux; www.astm.org/Standards/electronics-standards.html

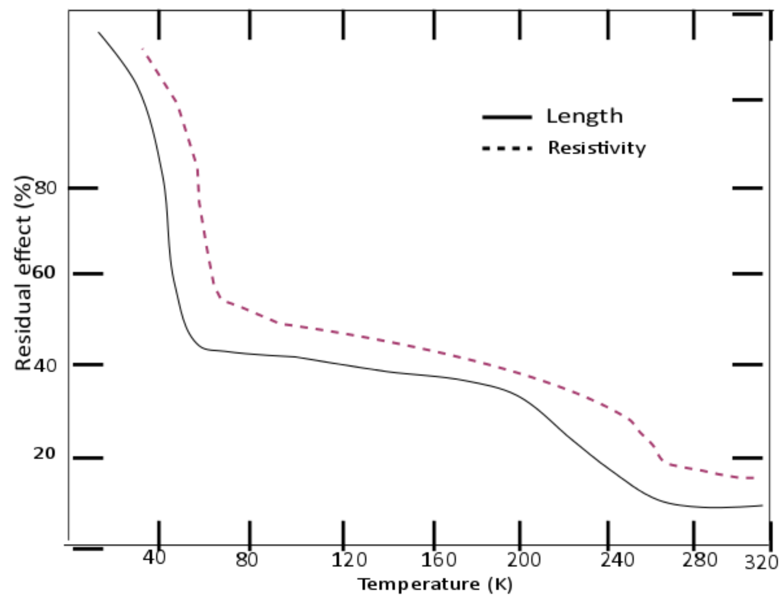

Figure 3.3: Effect of heating on length and resistivity of irradiated copper; ASTM data

3.4 Basic mechanism and their trends

3.4.1 Total dose effects in semiconductors

A dielectric layer in semi conductor devices consists of oxides and nitrides. Electron hole pair will be created in these layers due to the effect of ionizing radiation. Total dose effect depends on the creation of electron hole pair and the subsequent generation of traps near the interface or within the dielectric of the semi conductor devices. In Metal Oxide Semiconductor devices, the trapped charges cause flat band shift, threshold voltage shift or surface leakage current. The trap generation is due to the reason that, the electrons and holes created in the dielectric layer have different mobilities. Electrons will be swept out immediately to the positive electrode while holes which follow a hopping movement are not removed from the dielectric layer immediately. They get trapped near the interface or in the oxide volume. Hence, the associated fixed positive charge. The presence of positive charge (holes) near the interface requires that gate voltage to be adjusted more negative values to maintain the negatively charged inversion layer in the channel for the operation of the MOS devices.

The hole trap distribution in the oxide layer depends up on the variation of electric field in the oxide with time. The charge state influences the local quasi static Fermi level. The concentration of trapped charges will vary with changes in the applied voltage and the charge specific relaxation time. The dose rate is also an important parameter for the ionization effect in addition to the total dose effect, due to annealing of the charge state .

3.4.2 Displacement damage

The high energy particles or high energy photon can dislodge a silicon atom from the lattice of silicon crystal. This is known as displacement damage. About 20 eV of energy is required to remove an atom from the lattice of silicon. Displacement damage also cause defect clusters. The energy of the incident particle is reduced during the displacement effect. Hence, displacement damage can be related to Non-ionizing energy loss (NIEL). However, NIEL also depend on the particle type and energy. NIEL values have been calculated for most of the particles. During the interaction with X-rays, momentum conservation does not happen, as the threshold energy is 250 KeV for photons. Hence, X-rays do not cause direct displacements. ^{60}Co gamma rays cause displacement damage

primarily through compton electrons and are very less damaging ($\sim 10^{-3}$) than that of a neutron.

Sometime displacement can cause a change in doping characteristics . At some instances, it can create trap centers near the band edges, so that, charges can be captured and released after some time.

Displacement damage also cause the creation of mid gap states which facilitate transition of electron from valance to the conduction band. If the state is formed in the depletion region, reverse bias leakage current will increase. In forward biased state or in the non-depleted regions, mid gap state facilitate recombination.

3.4.3 Single event effects

Single event effect arise from the interaction of single particle, protons, neutrons or heavy ions with the semi conductor device causing either transient or permanent effects.

Collection of charge in p-n junctions

It is possible to have a pulse of current due to charge collection in p-n junction . The mechanism involved is easily understood. High energy protons and heavy ions loose energy in materials mainly through ionization process. As they pass through p-n junction, electron hole pair (e-h pair) are created along the path forming a track of charges. Out of these charges some of the electron and holes will recombine and some of them will be pulled in to the junction contacts. Charges are even collected from other side of the junction through tunneling and diffusion causing a current pulse of short duration at the internal circuit nodes which is struck by the particle.

The magnitude of the charge produced inside p-n junction depends on ion properties such as energy, type and charge densities. It also depends on the volume of the physical device, which determine the path length over which the charges are created, deposited and collected. The sensitivity of the electronic circuit to the current impulse is also important in recording the magnitude of the charges.

The prompt charges are collected within 200 picoseconds . The delayed charges, which are collected over a period extending above 1 microsecond is largely due to diffusion. Single event effect generally cause a delayed charge response. In case of high energy particles hitting the device, the passage of ions will affect the circuit . For any specific device, there is a critical charge for the ion passing through it, which shall upset the circuit .

When high energy particle pass through electronic devices, there can be effects which change the state of stored data in devices . Single Event Upset (SEU) and Multiple Bit Upset (MBU) etc. are examples. However these changes can be reset to normal by initialization of the storage device . There are potential catastrophic events which cause destruction of the device in most cases . Single Event Latch-up (SEL) belong to this category. Latching effect can lead to catastrophe, only after some time. Hence, it is possible to save the device, if latch-up is corrected in time. Single Event Hard Errors (SHE) are also catastrophic. This is due to failure of internal circuit element within complex circuit. The hard errors may be due to gate rupture in most cases.

3.4.4 Single event upset (SEU) and Multiple bit upset

SEU occurs in storage devices. When charge deposited by heavy ions exceeds the critical charge for the device, a change of state within the memory element can happen which may loose or distort the data stored. Miniaturization has increased the the possibility of upset.

When the device is bulky, such as that in the case of DRAMS or SRAM, Multiple Bit Upset can happen. The reason being that, the charge that diffused in the substrate could be collected by the circuit elements

3.4.5 Latch-up and Snap back

In CMOS devices, the junction isolation regions can cause a parasitic bipolar transistor that forms a four layer region. These bipolar structures are not involved in normal circuit operation. But this four layer bipolar structure get triggered by transient currents and exhibit properties of an SCR latch-up. Special guard band and clamp circuits are provided at input and output terminals to prevent latch-up occurring in standard circuit applications. However, in radiation environment, this protection will no longer useful as transient signals

are not confined to I/O terminals. Transient current pulses can be generated by heavy ions in the internal elements and the latch-up get triggered. Since, the latch up has the same nature of an SCR latch-up, the four region structure is switched in to conducting mode till the power is switched off. If the latch-up state is continued, the increased current cause heating of the device structure and cause localized damage in the silicon. Heating also cause damage in the metallization region.

Latch-up is of much concern in space application, since the device get damaged permanently. It is advisable to avoid a latch-up prone circuit. But it may not be possible, always. Another method shall be to use intelligent circuit to detect the latched-up state automatically to switch off or restart the system immediately. Device scaling increases the latch-up susceptibility. Latch-up is highly sensitive to temperature of the device. Hence, testing of latch-up is done at high temperatures expected in the device application.

Snap back is another effect due to the sufficient gain of parasitic bipolar transistor in extremely low dimension MOS devices to affect the device operation. Snap back effect is the reduction in the break down voltage of parasitic transistor caused by the injection of minority carriers from the source through diffusion in to the well region. A small increase in current is observed in the device as a result of the snap back. Snap back is not very sensitive to temperature. The recovery from snap back could be achieved through sequencing voltage signals and supply voltage need not be reduced as in the case of latch-up.

3.4.6 Single event hard errors

Single event hard errors are most possible when the device dimensions are very low. In this case, it is possible to have interaction even with a single ion to produce a catastrophic damage. A charge deposition within the gate oxide can lead to this effect. Micro-dose can cause increase in leakage current in transistors within VLSI circuit. This can cause failure in some type of circuits particularly in DRAM and SRAM.

The gate rupture in power MOSFET can be a cause of single event hard errors. it may be caused by a short spike in the gate region of an individual transistor. This error is important in memory cells and FPGAs. A heavy ion permanently alters the gate array.

The probability of the above phenomenon occurring in space is extremely low and insignificant due to current advancement in radiation hardening technology applied in the space grade devices. However, as the device is scaled down to smaller dimension, the mechanism become important, because of the expected decrease of threshold LET at these dimensions.

3.4.7 SEE rate calculations

SEE depends on the cross section of the device, particle flux, distribution and the device specific values such as critical charge , sensitive area, sensitive volume etc. The distribution depends on the solar flare activity, radiation belt activity and shielding provided. From the knowledge of the above parameters and values , it may be possible to calculate the upset rate by applying proper simplifying assumptions.

Computer codes such as CRUP and CREME can be used to calculate the final error rates/bit-day.

The calculation involved may have assumptions and uncertainties, which work for devices with nearly ideal cross section and sensitive volume. But the methods are less successful for highly scaled devices. The approach used in various assumptions are outlined below.

Particle distribution

The particle distribution of the galactic cosmic ray is assumed to follow Heinrich curve, which provides several distribution of flux versus LET corresponding to solar maximum, solar minimum , a 10% possibility for worst case flare and a worst case flare distribution(rarely used). An unusual solar flare event can cause much larger increase in solar distribution which will increase the upset or latch-up rate.

Chord length distribution

A cosmic ray can strike an Integrated Chip from an angle. It is important to take in to account the way that the particle intercepts the total charge collection volume as they pass through in different location and angle. These details have

been worked out for simple parallel piped geometries and can be used for the distribution of chord length within the volume. The chord length integral is then used along with the ion distribution and the critical charge to determine the probability that the particle in the environment will produce an upset.

Cross section

Measurement of cross section are available only at fixed values of LET and usually it become necessary to adjust some of the results to account for the experimental result, including the cosine dependence for ions that have angle other than normal incidence. Most cross sections rise gradually with increasing LET.

Bibliography

[1] [1]0.L. Curtis,Jr.,J.W.Cleiand,and J. C.Pigg"Effectof Irradiation on the Hole Lifetime of n-Type Germanium,"Bull.Am.Phys.Soc.2,SeriesII, 157 (1957)

[2] Seitz, F. (1949) On the disordering of solids by action of fast massive particle. Discuss. Faraday Soc. Vol 5 p 271 ,
(1949)

[3] Kinchin G. H. & Pease R. S. The displacement of atoms in solids by radiation. Rep Prog Phys 18, 151 (1955).

[4] John A. Brinkman, On the Nature of Radiation Damage in Metals,J. Appl. Phys. 25, 961 (1954)http://dx.doi.org/10.1063/1.1721810

[5] J.H.O. Varley, A new interpretation of irradiation-induced phenomena in alkali halides,Journal of Nuclear Energy, (1954),Volume 1, Issues 12, 1954, Pages 130-143

[6] G. J. Dienes1 and A. C. Damask,Radiation Enhanced Diffusion in Solids, J. Appl. Phys. 29, 1713 (1958), http://dx.doi.org/10.1063/1.1723032

[7] G.H. Kinchin, M.W. Thompson, Irradiation damage and recovery in molybdenum and tungsten,Journal of Nuclear Energy (1954),Volume 6, Issue 4, May 1958, Pages 275-284

[8] A.H. Cottrell LX. The formation of immobile dislocations during slip, The London, Edinburgh, and Dublin Philosophical Magazine and Journal of Science: Series 7, Volume 43, Issue 341, 1952 pages 645-647, DOI:10.1080/14786440608520220

[9] W.M. Lomer, A dislocation reaction in the face-centred cubic lattice,The London, Edinburgh, and Dublin PhilosophicalMagazine and Journal of Science: Series 7,Volume 42, Issue 334, 1951 ,pages 1327-1331,DOI:10.1080/14786444108561389

Chapter 4

Semiconductor Technology for Space Applications

4.1 Semiconductor Devices

The advancement in Semiconductor physics is based on the theories of the structure of atom and principles and applications of quantum mechanics. Rutherford scattering experiment was the first successful experiment to probe in to the atom. A very thin foil of gold was bombarded by a beam of alpha particle from a radioactive source and the angular distribution of the scattered particles from gold foil is observed. From the observation, Rutherford was able to propose a new model of the atom which can beautifully explain the experimental result. However, Rutherford model has to be modified due to the disagreement with electromagnetic theory. Later, Bohr introduced another model for the atom which appears to be a modification of Rutherford model. But, Bohr model is significantly different from Rutherford model in concepts and theory. Bohr model was accurate in explaining hydrogen spectra. However, level splitting observed in later experiments could not be accounted by Bohr's model. A more correct account of these experiments was elucidated by the advent of quantum mechanics by W. Heisenberg and E. Schrodinger. Heisenberg's Uncertainty Principle limits the measurement of position and momentum of the particles simultaneously.

$$\Delta p.\Delta x \geq \frac{h}{2\pi};$$

$$\Delta E.\Delta t \geq \frac{h}{2\pi};$$

Where Δp, Δx, ΔE, and Δt are the uncertainties in the momentum, position, energy and time respectively. The state of particle is described by wave

function in the Schrödinger equation. The wave function depends on quantum numbers namely the Principal quantum number, Sub-orbital number,and Magnetic quantum number and Spin quantum number. The one dimensional Scrödinger equation is represented by;

$$i\hbar\frac{\partial\psi}{\partial t} = -\frac{\hbar^2}{2m}\frac{\partial^2\psi}{\partial x^2} + V\psi; \tag{4.1}$$

Where $\Psi \equiv \Psi(x,t)$ is the wave function.

$\Psi(x,t) = \varphi(t)\Psi(x)$; E is the kinetic energy of the particle.

For free particle, the potential energy V vanishes. Hence time dependent Schrödinger equation reduces to:

$$\frac{\partial^2\psi}{\partial x^2} + k^2\psi = 0 \tag{4.2}$$

Where k=$\frac{\sqrt{2mE}}{\hbar}$; $k = 2\pi/\lambda = p/\hbar$; Where p is the momentum of the particle.

4.1.1 Energy bands in solids

When two atoms are completely isolated, there is no interaction between the wave function. They can have identical electronic structure. Electrons can have discrete energy levels, as predicted by Bohr's postulate. As the distance between the atoms are made smaller, as that in a solid, the wave functions will interact and the energy levels of the electrons will split in to multiple discrete energy levels of the combined atoms. In solids, several atoms are confined in a small region. Hence, the number of energy levels becomes so large, to form a continuous energy band. Each silicon atom has a structure $1s^2, 2s^2, 2p^6, 3s^2, 3p^2$. Figure (4.1) shows the atomic structure of silicon atom.

The outer most shells have 4 electrons which enter in hybridization and become identical, but they will have different states as per Pauli's Exclusion Principle. Thus N atoms in a volume will have electrons with 4N states. As the distance between the atoms are further reduced, the bands will split in to two. The upper band being the conduction band and the lower band, the valance band. The energy gap between the bands is called forbidden gap E_g. In the solid, there will be no electrons with energy belonging to that of the forbidden energy.

Forbidden band or band gap (E_g) is the energy band between valance band and conduction band(Figure 4.2). $E_g = E_c - E_v$; Where E_c is the energy of the

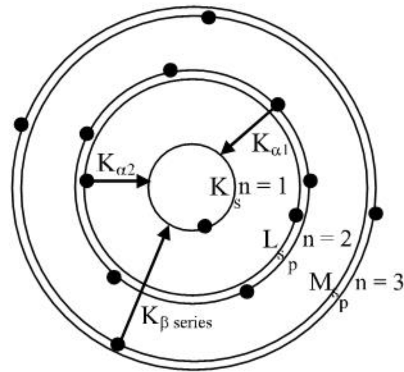

Figure 4.1: Silicon atomic structure - Possible X-ray florescence transitions

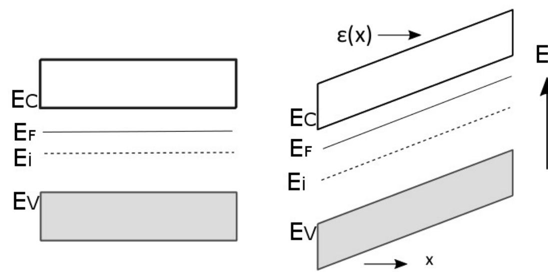

Figure 4.2: Energy band diagram with and without electric field

conduction band minimum and E_v that of the valance band maximum. At 0 K, electrons occupy in the lowest energy band. The 4N states of valance band now become full and the conduction band become empty. Hence no electrons are available for conduction. Hence at 0 K,the semiconductor will act as a perfect insulator. The intrinsic level or the Fermi level of intrinsic semiconductor E_i is given by:$E_i = E_v + E_g/2$. Band gap of germanium and silicon are 0.67 eV and 1.11 eV respectively. The band gap of III-V semiconductors like InP and GaAs are 1.35 eV and 1.43 eV respectively.

The energy gap in semiconductor will be less than 4 eV. For an insulator like SiO_2 the energy gap is 9 eV. For that reason, the conductivity of a semi conductor can be increased by exciting electrons of the valance band to occupy the conduction band creating electron hole pair in the crystals. Some of the electrons are excited even at room temperature. Hence, at room temperature, the conductivity of the semiconductor will be higher than that of an insulator.

4.1.2 Direct and Indirect band semiconductors

The plot of the energy of electron as a function of $\overrightarrow{k}$, in the principal direction of the crystal is shown in figure (4.3) for direct band gap and indirect band gap semiconductors.

For direct band semiconductors electrons in the conduction band minimum and the valance band maximum will have the same momentum. Hence, the same value of K. But, for indirect band gap semiconductors, the above electrons will have different values of k. since the momentum $p = \hbar k$; are different for the conduction minimum and valance maximum , the electrons in the conduction band cannot combine with a hole in the valance band by releasing a photon. Hence, electrons first transfer in to an intermediate state, Er by the release of a phonon and from there, it will transfer to valance band releasing a photon. Ge and Si are indirect band semiconductors.

4.1.3 Effective mass of the electrons and holes

Since the electrons in the crystal interact with periodic potential of the lattice, the wave motion of the electron is affected by the potential. Hence, a correction is applied to the mass of the electron to account for the interaction of the periodic potential during its motion in the crystal.

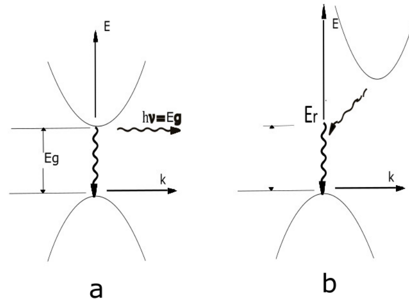

Figure 4.3: Energy of electron as a function of k. (a) Direct band and (b) indirect band semiconductors

The energy of the electron $E = \frac{\hbar^2 k^2}{2m}$; is parabolic with k. We get $\frac{d^2E}{dK^2}=\frac{\hbar^2}{m}$; Therefore the effective mass of the electron in the band $m_e^*=\frac{\hbar^2}{\frac{d^2E}{dK^2}}$;

Similarly the effective mass of the holes m_h^* account for the charge transport of the holes in the valance band.

The effective mass of the electrons and holes in silicon crystal are $1.1m_o$ and $0.56m_o$, respectively, where m_o is the electron rest mass.

4.1.4 Hole conduction

In a semiconductor specimen of volume V with N number of atoms there must be 4N states in the valance band and 4N states in the conduction band. At 0K, all the states of valance band is filled with electrons. For every electron with a velocity υ_j, there is another electron with velocity $(-\upsilon_j)$. Hence, current density due to holes must be zero. Current density due to holes $J = -\frac{q}{v}(\Sigma_{k=1}^{4N}\upsilon_k) = 0$ for filled valance band.

4.1.5 Excess carriers in semiconductors

Excess carriers in semiconductors are charges present in the semiconductor in excess of their thermal equilibrium value. Excess carries can be generated by photon excitation, electron bombardment, injection across p-n junction etc.

4.1.6 Photo generation

This is the process of generating excess carriers when photons are incident on semiconductors. If the photon energy is larger than the band gap of the semiconductor, the energy of the photon is absorbed by the electron in the valance band creating an electron hole pair. The energy of the electron, become that of the conduction band. As a result, an electron is generated in the conduction band and a hole is generated in the valance band in excess of their thermal equilibrium value.

If light of intensity I_0, falls on one face of a sample of thickness t, then the amount of light (photon) transmitted given by $I(t) = I_0 e^{-\alpha t}$ where α is the absorption coefficient. The absorption coefficient depends on the energy of the incident wave. When excess carrier concentration is small compared to the equilibrium majority carrier concentration, it is said to be low level injection. In high level injection, the excess carrier concentration is comparable to majority carrier concentration

4.1.7 Transient decay of excess carriers

In a direct recombination process, electrons in the conduction band falls in to the vacant state (holes) in the valance band by the release of energy in the form of photon. The rate of decay is proportional to the population of electron and holes at any time t. Let, Δn and ΔFp are the initial excess concentration of electron and holes at t=0. Since, the electrons and holes recombine in pairs, after a time t, the instantaneous values of carrier concentration δn(t) and δp(t) are also equal. The net rate of change of conduction band electron concentration is equal to the thermal generation rate minus recombination rate. ie.$-\frac{dn}{dt} = \alpha_r(n(t)p(t) - n_i^2)$;.... where n_i is the intrinsic carrier concentration or thermally generated carriers.

Here, $n(t) = n(0) + \delta\ n(t)$ and $p(t) = p(0) + \delta p(t)$

With this substitution, the above equation become;$-\frac{d\delta n(t)}{dt} = \alpha_r([n(0)+\delta n(t)][p(0)+\delta p(t)] - \alpha_r n_i^2)$; with $\frac{dn_0}{dt} = 0$.

ie, $-\frac{d\delta n(t)}{dt} = \alpha_r[(n(0) + p(0))\delta n(t) + \delta^2 n(t)]$; by $n(0)p(0) = n_i^2$

For low level injection $\delta^2 n(t)$ will be negligible compared to other terms. For

p-type semiconductor, $n(0) + p(0) \simeq p(0)$; Hence, $-\frac{d\delta n(t)}{dt} = \alpha_r p(0)\delta n(t)$

The above equation suggests an exponential decay of excess carrier in a n-type semiconductor. The above equation in exponential form is written as $\delta n(t) = \Delta n.e^{(-t/\tau_n)}$; where τ_n is the minority carrier life time. Δn is the excess carrier concentration at t=0. Similarly, $\delta p(t) = \Delta p.e^{(-t/\tau_p)}$. Thus, the excess majority carriers and minority carriers recombine at the same rate during direct recombination process.

4.1.8 Recombination mechanism

In the case of direct band semiconductors, like InP and GaAs, the electron in the conduction band minimum directly falls in to the hole in the valance band maximum. Generation and recombination are continuous process in a semi conductor.

In the case of indirect recombination process, impurity atoms other than donors and acceptors introduce localized energy levels deep in the band gap near the band edges. These intermediate levels effectively reduce the band gap and enhance recombination process. The location in the band gap can act as a trap for electron or hole. The trapped electron will be de-trapped after some time. There can be electron trap centers or hole trap centers.

4.1.9 Auger recombination

Auger recombination is a process involving three particles. In one way 2 electrons and one hole are involved. Otherwise, two holes and one electron are involved. The recombination process is depicted in figure (4.4).

In the case of electron-electron-hole(e-e-h) process, the electron in the state 1 in the conduction band recombine with hole in the state 1* in the valance band . In this process the energy released is transferred to the electron 2 in the conduction band which in turn excited to the state 2* in the conduction band. The electrons then return back to conduction band minimum from the state 2* by imparting kinetic energy to the lattice atoms. A similar process occurs in (h-h-e) recombination process with holes in the valance band take the position of electrons in the conduction band.

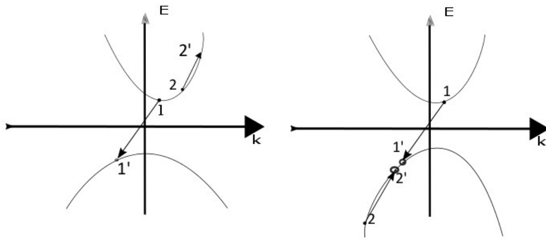

Figure 4.4: Auger recombination

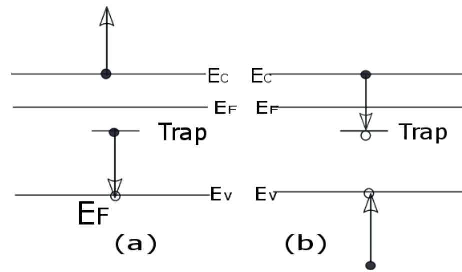

Figure 4.5: Trap aided Auger recombination

There is another process by which the trapped electron makes a transition to the valance band by giving its energy to the electron in the conduction band. This is more significant in heavily doped n- type semiconductor with concentration of traps below Fermi energy level. This process is called as trap aided (e-e-h) auger recombination process. Similarly, there can be hole trap aided (h-h-e) auger recombination process in which is significant in heavily doped p-type semi conductor. Figure (4.5) shows trap aided Auger recombination.

4.1.10 Origin of Traps centers

Impurities in the semiconductor, imperfection due to radiation damage and unsaturated bond near the surface are the known causes of traps. Impurity atoms always introduce trap centers in the middle of the band gap. However, this can be controlled by using high purity semiconductors. The traps introduced by radiation are of great importance . Energetic particles like protons and electron displace atom from their position in the lattice creating vacancies and interstitial. These lattice defects act like deep impurities. The nature of the traps created depends on the radiation dose. However, radiation induced traps are subjected to annealing, even at room temperature over a long period

of time.

Surface traps are due to unsaturated bonds at the surface. The reason is that,the lattice is not extended beyond the surface. This irregularity will create energy levels within the forbidden gap which are normally dense. These states are called surface states. Surface traps will be present even when there is the presence of an oxide coating on the surface. The density of the surface states on bare clean surface is in the range of $10^{15}/cm^2$. With oxide coating the surface,the trap density reduces to $10^{12}/cm^2$. The reason being that, some of the bonds get saturated by the oxide layer.

4.1.11 Diffusion of charge carriers

When excess charge carriers are generated in a semi conductor, there may be non-uniformity in the distribution of generated charge carriers. This will cause movement of charge carriers from the region of high concentration to region of low concentration resulting in diffusion current.The expression for diffusion current density due to electron $J_n(x)$ and that due to holes $J_p(x)$ are given by:

$J_n(x) = qD_n\frac{dn}{dx}$;

Where D_n is the electron diffusion constant and $n(x)$ is the electron distribution.

Similarly, $J_p(x) = qD_p\frac{dp}{dx}$;

Where D_p is the hole diffusion constant and $p(x)$ is the hole distribution; q is the charge of the carriers.

The total diffusion current due to electron and hole diffusion is

$$J = J_n(x) + J_p(x)$$

When a carrier gradient exist in a semiconductor at equilibrium, an electric field is created. This is called built in field.

4.1.12 Einstein relation

The ratio of the diffusion constant D_p to the mobility μ_p of electrons and holes are equal under thermal equilibrium. ie., $\frac{D_p}{\mu_p} = \frac{D_n}{\mu_n} = \frac{kT}{q}$

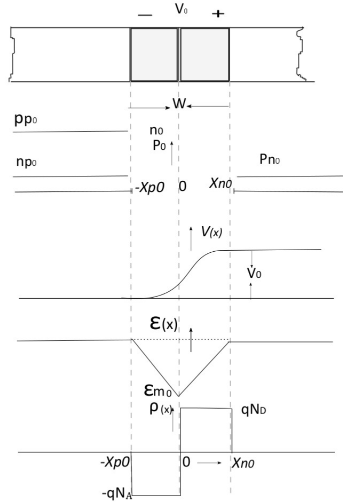

Figure 4.6: Distribution of Charge carriers, Charge density, Electric potential and Electric field

4.2 Junction Diodes

A junction diode is characterized by a p-region, n-region and a depletion region over a semiconductor wafer. The depletion region is in the middle region where there are no mobile charge carriers. There are different technology to achieve the configuration of a junction diodes, which are not discussed here. The junction diode can conduct current only when it is forward biased, which is achieved by connecting positive potential to the p-side of the diode and negative potential to the n-side of the diode. The distribution of charge carriers, potential ,electric field and charge density is depicted in the figure (4.6).

4.2.1 Electric field distribution in a diode

Since Poisson's equation relation is applied to depletion region, we get; $\frac{d\varepsilon_(x)}{dx} = \frac{\rho}{\epsilon}$; Where $\frac{\rho}{\epsilon}$ is the ratio of change density to the dielectric constant of semiconductor. For the p-side of the depletion layer, we have $\rho = qN_A$.

Hence, $\frac{d\varepsilon_(x)}{dx} = \frac{qN_A}{\epsilon}$; on integration,

$\epsilon_x = \int -\frac{q}{\epsilon} N_A dx + C$

With $\epsilon_x = 0$ at $x = X_{p_o}$ where X_{p_o} is the width of the depletion region towards p-side of the junction, we get, $\epsilon_x =$ -$\frac{q}{\epsilon} N_A(x + X_{p_o})$; $-X_{p_o} < x < 0$. Ref.[1],[32].

Applying Poisson's equation on n-side of the depletion region; $\varepsilon_x = -\frac{q}{\epsilon}N_D(x - X_{n_o}); 0 < x < X_{n_o}$. At $x = 0$, the electric field is maximum. Hence, $\varepsilon_m = -\frac{q}{\epsilon}N_A X_{p_o} = \frac{q}{\epsilon}N_D X_{n_o})$ Hence,

$$\varepsilon_x = \varepsilon_{m_0}(1 + \frac{x}{X_{p_o}});$$

in the region of the depletion region towards p-side. Also,

$$\varepsilon_x = \varepsilon_{m_0}(1 - \frac{x}{X_{n_o}});$$

in the region of the depletion region towards n-side.

4.2.2 Electric potential distribution in a diode

We assume that, the potential $V_{p(x)} = 0$ at $x = -X_p$. We have, $V_{p(x)} = -\int \varepsilon_x dx$ in the p-side of the depletion region where $\varepsilon_(x) = \varepsilon_m(1 + (\frac{x}{X_{po}}))$;

Substituting for ε_x and integrating, by taking $V_{p(x)} = 0$ at $x = -X_p$; we get, $V_{p(x)} = -\varepsilon_m(x + \frac{x^2}{2X_{P_O}} + \frac{X_{P_O}}{2})$; on the p-side of the depletion region and $V_{n(x)} = -\varepsilon_m(x - \frac{x^2}{2X_{n_O}} + \frac{X_{P_O}}{2})$; on the n-side of the depletion region

4.2.3 The Ideal Diode equation

The current in a p-n junction is $I_n + I_p$. Since, I_n and I_p are constant in the depletion region, it can also be evaluated as the sum of the minority carrier diffusion current at the edge of the depletion layer. The potential drop in this region is negligible, so that minority carrier current in this region is by diffusion only. Figure (4.7)depict this situation. An ideal diode equation given below is based on the following assumption.

1. The length of the neutral regions on either side of depletion region are long compared to depletion region.
2. Depletion region has no mobile charge carriers and the region outside the depletion region is perfectly neutral
3. The junction is step graded or abrupt
4. Low level injection condition exists when diode is forward biased

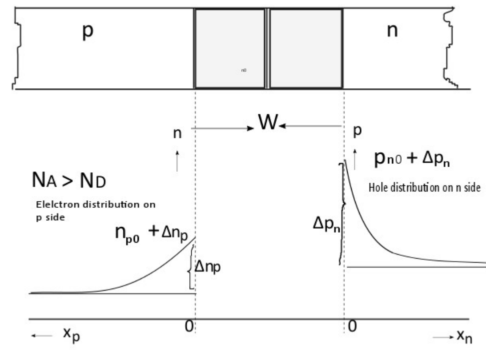

Figure 4.7: Minority carrier distribution across forward biased PN junction

5. The impurities are completely in the ionized state
6. Contacts at the ends are perfectly ohmic contacts and minority carrier density at the contact are at the equilibrium value
7. There is no generation or recombination within the depletion region
8. The applied voltage is DC for the diode current equation

With above assumption, the equation for a diode can be written as:

$$I = qA(\frac{D_p}{L_p}P_{n_o} + \frac{D_n}{L_n}n_{p_0})(e^{\frac{qV_a}{KT}} - 1) \tag{4.3}$$

Where,D_p and D_n are the diffusion constant for holes and electrons; L_p, L_n are the electron diffusion length and hole diffusion length respectively. P_{n0} is the equilibrium hole concentration on the n-side and n_{p0} is the equilibrium electron concentration on the p side. V_a is the applied bias voltage.

For short diodes,it is taken that,the length of the neutral region of the diode on the n-side,$W_n << L_p$ and that on the P-side of the diode,$W_p << L_n$. here, $W_n$and W_p are the width of the depletion region on the n-and p-side. The diode equation may be approximated to

$$I = qA(\frac{D_p}{W_n}P_{n_o} + \frac{D_n}{W_p}n_{p_o})(e^{\frac{qV_a}{KT}} - 1) \tag{4.4}$$

The above equation may be written as

$$I = I_0(e^{\frac{V_a}{\eta V_T}} - 1) \tag{4.5}$$

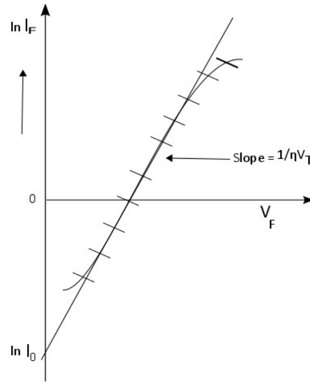

Figure 4.8: Ideal diode characteristics with current in log scale

Hence,

$ln(I) = ln(I_0) + V_F/\eta V_T$ where $V_F$is the applied forward voltage. The graph of the above equation is shown in figure (4.8). On the graph,ηV_T is identified as the reciprocal of the slope in the linear region.η is called ideality factor and its value is between 1 and 2. For silicon at room temperature, the value of η is 2. For germanium $\eta = 1$.

4.2.4 Depletion layer capacitance

The junction capacitance may be considered as the parallel plate capacitance with separation between the plates as the depletion layer width W. The junction capacitance is given by $C_j = \frac{\epsilon A}{W}$. The junction capacitance decreases with increase in reverse bias.

4.3 Bipolar Junction Transistor (BJT)

BJT is a device with three regions and two junctions. It has a P region sandwiched between two N regions or a N region sandwiched between two P regions. The central region is the base. Others are called collector and emitter depending on the doping profile and size. The width of the middle region is very small and it is lightly doped. For this reason very few recombination is possible in the base region. The emitter, which is heavily doped, can inject minority carriers across the reverse biased base collector junction which is collected by the collector. Hence, emitter and collector current are almost equal.

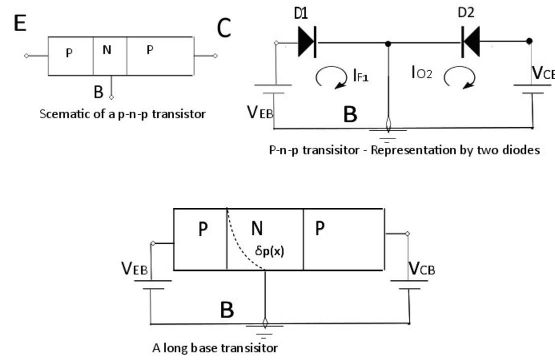

Figure 4.9: PNP transistor structure

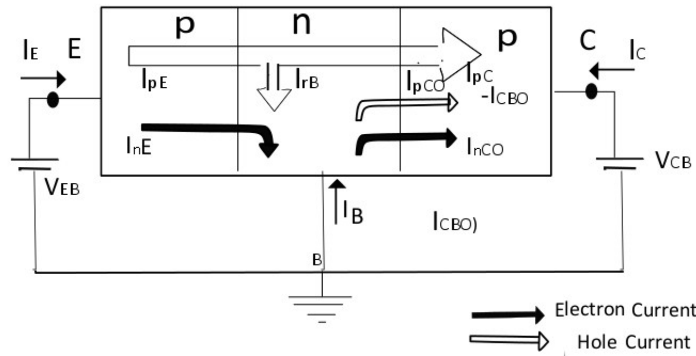

Figure 4.10: Current components in a forward biased pnp transistor

4.3.1 Current flow in a transistor

For a transistor, for proper operation in active mode, base emitter junction must be forward and base collector junction must be reverse biased as in figure (4.9). In the p-n-p transistor, holes are injected from emitter in to the base region and electrons from base to emitter. A very small number of injected holes at the base will recombine with electrons at the base constituting the base current and remaining portion goes to the collector region constituting the collector current. The collector current is also caused by the minority carrier current I_{CBO} , which is also known as the reverse saturation current across the base-collector junction or the leakage current across collector base junction. Figure 4.10 shows the current components in transistor. Figure (4.11) shows the different transistor configurations. The components of currents in a transistor are:

1. Emitter current due to holes injected from emitter to base (I_{pE})
2. Emitter current due to electrons injected from base to emitter (I_{nE})
3. Base current due to recombination (I_{rB})
4. Collector current due to holes reaching the collector (I_{pC})
5. Reverse saturation current of collector base junction (I_{CBO})

The current through the terminals are:

1. Emitter current $I_E = I_{pE} + I_{rE}$
2. Collector Current $I_C = -(I_{pC} - I_{CBO})$
3. Base current $I_B = -(I_{rB} + I_{nE} + I_{CBO})$

4.3.2 Transistor - Ebers model

Ebers model depicts a large signal model of BJT by which it is possible to represents the terminal currents of transistor in common emitter, common collector and common base configuration. To represent the various currents in a transistor using this model, the following symbols are used for representing parameters.

1. V_{BE} and I_B Common emitter input voltage and input current
2. V_{EB} and I_E Common base input voltage and input current
3. V_{BC} and I_B Common vollector input voltage and input current
4. V_{CE} and I_C Common emitter output voltage and output current
5. V_{CB} and I_C Common base output voltage and output current
6. V_{EC} and I_E Common collector output voltage and output current
7. I_{ES} Reverse saturation current of emitter base diode with collector shorted to base
8. I_{CS} Reverse saturation current of collector base diode with emitter shorted to base

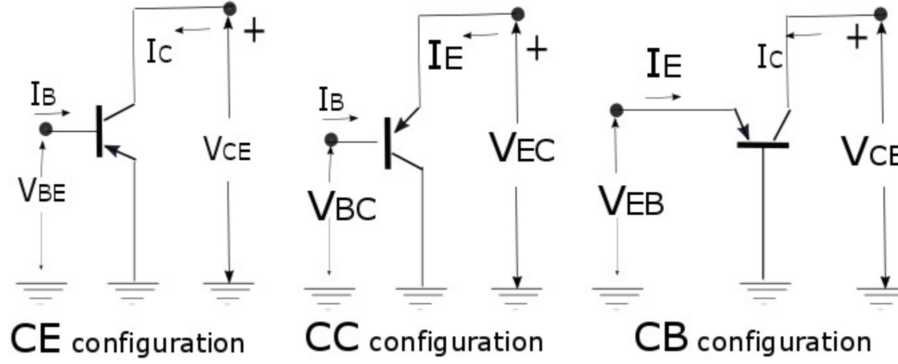

Figure 4.11: Common emitter, common collector and common base configuration

9. α_F Current amplification factor When emitter base junction is forward biased and emitter base junction is reverse biased

10. α_I Inverse alpha is the current amplification factor, when collector base junction is forward biased and emitter base junction is reverse biased

The terminal current can be represented in terms of these parameters. Here I_{ES} and I_{CS} are negative for n-p-n transistors and positive for p-n-p transistors . The Ebers Moll equation are: Refer to figure (4.12)

$$I_E = -[I_{ES}(e^{V_{EB}/V_T} - 1) - \alpha_I I_{CS}(e^{V_{CB}/V_T} - 1)] \tag{4.6}$$

$$I_C = -[I_{CS}(e^{V_{CB}/V_T} - 1) - \alpha_F I_{ES}(e^{V_{EB}/V_T} - 1)] \tag{4.7}$$

Multiplying I_E with α_F and adding with expression for I_C above, we get

$$\alpha_F.I_E + I_C = -I_{CS}(1 - \alpha_F\alpha_I)(e^{V_{CB}/V_T} - 1) \tag{4.8}$$

$$I_C = -\alpha_F.I_E - I_{CS}(1 - \alpha_F\alpha_I)(e^{V_{CB}/V_T} - 1) \tag{4.9}$$

If the emitter is open $I_E = 0$ and I_C is given by

$$I_C = -I_{CS}(1 - \alpha_F\alpha_I)(e^{V_{CB}/V_T} - 1) \tag{4.10}$$

$$I_C = -I_{CBO}(e^{V_{CB}/V_T} - 1) \tag{4.11}$$

where $I_{CBO} = I_{CS}(1 - \alpha_F\alpha_I)$

Similarly, $I_{EBO} = I_{ES}(1 - \alpha_F\alpha_I)$

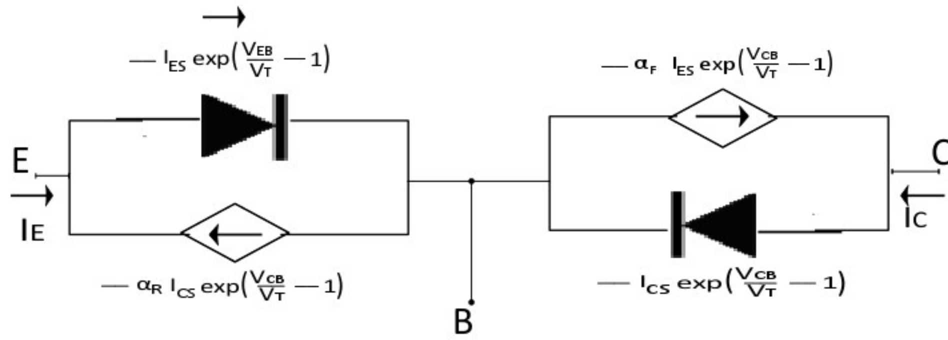

Figure 4.12: Ebers Moll model of p-n-p transistor

4.3.3 Transistor characteristics

Common base configuration

A p-n-p transistor configuration is shown in figure (4.13) and that of n-p-n transistor is shown in figure (4.14)

Input characteristics can be evolved from Ebers equation with V_{CB} held constant as below.

$I_E = -I_{ES}(e^{V_{EB}/V_T} - 1) - \alpha_I I_{CS}$. For p-n-p transistors I_{ES} and I_{CS} are negative. The curves are similar to the characteristics of p-n junction. But, as V_{CB} is increased for a given V_{EB}, we find that, as I_E increase, the curve shifts towards left . The reason is that, the increase in V_{CB}, causes a decrease in depletion layer width. This will cause the minority carrier concentration gradient to increase. Hence, I_E and I_C increase.

Keeping I_E constant, Ebers equation for output characteristics is written as,

$$I_C = -\alpha_F I_E - I_{CBO}(e^{V_{CB}/V_T} - 1) \tag{4.12}$$

When collector base junction is sufficiently reverse biased, which is often the case, and with $I_E = 0$, we get $I_C = I_{CBO}$. When I_E is not zero, then, $I_C = -\alpha_F.I_E + I_{CBO}$, when V_{CB} reverse biased. See figure (4.15) for the nature of collector current.

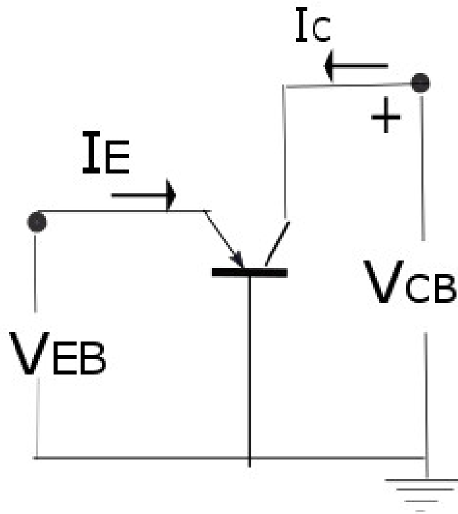

Figure 4.13: Transistor configuration(p-n-p)

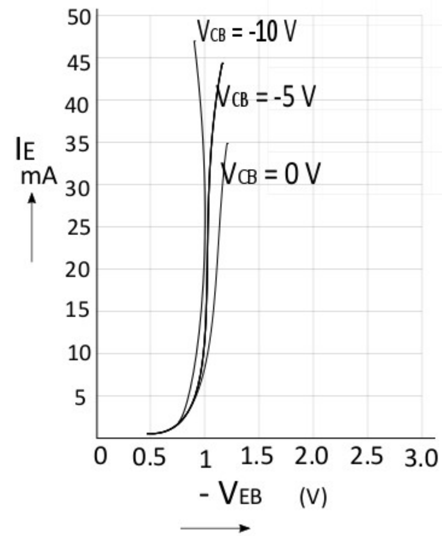

Figure 4.14: Input characteristics (p-n-p)

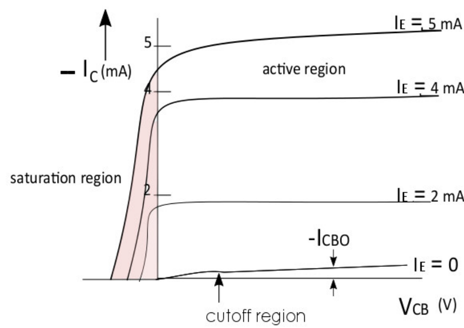

Figure 4.15: Output characteristics of p-n-p transistor - common base configuration

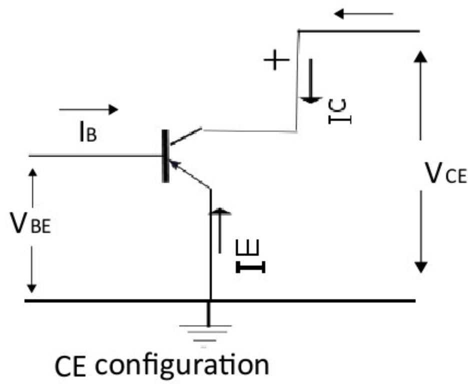

Figure 4.16: p-n-p transistor- common emitter configuration

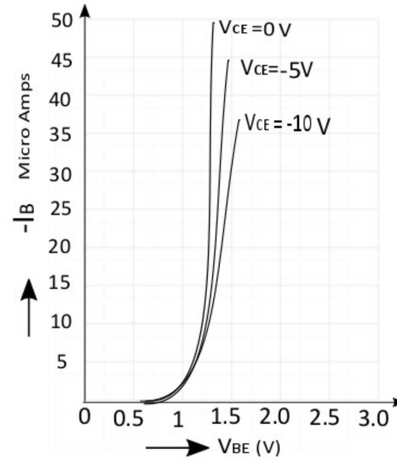

Figure 4.17: p-n-p transistor- common emitter characteristics

Common emitter configuration

The input characteristics of common emitter configuration can be evolved from Ebers equation, keeping V_{CE} constant. By assuming large reverse bias on collector base junction, we write $I_B = I_E - I_C$. Hence,

$$I_B = I_{ES}(1 - \alpha_F)(e^{\frac{V_{EB}}{V_T}} - 1) - I_{CS}(1 - \alpha_I) \tag{4.13}$$

For p-n-p transistors I_{ES} and I_{CS} are negative. I_B decreases with increase in V_{CB} due to width modulation. The input characteristics shift towards right with increase in V_{CE}. See the CE configuration of p-n-p transistor in figure (4.16) and and its output characteristics in figure (4.17)

The output characteristics in common emitter configuration is the plot of I_C as a function of V_{CE} . As V_{CE} is increased, I_C increases, due to reduced forward bias on collector base junction up to the point C (saturation). When V_{CE} is further increased, there is no corresponding increase in I_C, due to increased reverse bias at collector base and transistor enters the active region of operation. Due to base width modulation, however, I_C increases as V_{CB} increases.

$$I_C \cong I_S(e^{\frac{V_{EB}}{V_T}} - 1)(1 + \frac{V_{CE}}{V_A}) \tag{4.14}$$

Where V_A is the early voltage got by extrapolating the curve to meet on voltage axis.

Gummel Pool model

Gummel pool model takes in to account of several second order effects such as base width modulation, recombination in the emitter base depletion layer, high injection effects etc; as against Ebers model. This model is the basis for SPICE (Simulation Program with Integrated Circuit Emphasis).

A non-uniform doping in the base causes non-uniform electric field in the base region which aids the current flow through the base. Hence, current due to holes injected from emitter to base may be written as:

$$I_{pE} = qA\mu_p p(x)\varepsilon - qAD_p\frac{dp(x_n)}{dx_n}; \tag{4.15}$$

Assuming $,nx(n) = N_d(x_n)$, The built in electric field $\varepsilon(x) = -\frac{kT}{q}\frac{1}{N_D(x)}\frac{dN_D(x)}{dx}$
Hence,

$$I_{pE} = qA\mu_p p(-\frac{kT}{q}\frac{1}{n}\frac{dn}{dx_n)} - qAD_p\frac{dp}{dx_n} \tag{4.16}$$

$$I_{pE} = -\frac{qAD_p}{n}(p\frac{dn}{dx_n} + n\frac{dp}{dx_n}); \tag{4.17}$$

$$I_{pE} = -\frac{qAD_p}{n}(\frac{d(pn)}{dx_n}); \tag{4.18}$$

[since,$\frac{D_p}{\mu_p} = \frac{kT}{q}$]

$$\frac{I_{pE}.n}{qAD_p} = \frac{d(pn)}{dx_n}); \tag{4.19}$$

Integrating this equation from emitter base junction (0) to collector base junction(W_B) assuming hole current I_{pE} is almost uniform in the base region.

$$-I_{pE}\int_0^{W_B}\frac{ndx_n}{qAD_p} = \int_0^{W_B}\frac{d(pn)}{dx_n}dx_n \tag{4.20}$$

$= pn|_0^{W_B};$

Since, $pn = n_i^2 e^{\frac{qV}{kT}}$

$$-I_{pE}\int_0^{W_B}\frac{ndx_n}{qAD_p} = n_i^2 e^{\frac{qV}{kT}|_0^{W_B}} \tag{4.21}$$

$$ie; -I_{pE}\int_0^{W_B}\frac{ndx_n}{qAD_p} = n_i^2(e^{\frac{qV_{CB}}{kT}} - e^{\frac{qV_{EB}}{kT}}) \tag{4.22}$$

$$I_{pE} = \frac{qAD_p n_i^2(e^{\frac{qV_{CB}}{kT}} - e^{\frac{qV_{EB}}{kT}})}{\int_0^{W_B} ndx_n}; \tag{4.23}$$

$\int_0^{W_B} ndx_n = Q_{GB}$ is called Gummel Number

$$I_{pE} = \frac{-qAD_p n_i^2(e^{\frac{qV_{CB}}{kT}} - e^{\frac{qV_{EB}}{kT}})}{Q_{GB}}; \tag{4.24}$$

For proper operation of transistor, V_{CB} has to be negative. Hence,

$$I_{pE} = \frac{qAD_p n_i^2(e^{\frac{qV_{EB}}{kT}})}{Q_{GB}}; \tag{4.25}$$

Similarly, emitter current due to electron from the base is

$$I_{nE} = \frac{qAD_n n_i^2(e^{\frac{qV_{EB}}{kT}})}{Q_{GE}}; \tag{4.26}$$

Where Q_{GE} is called the Emitter Gummel Number. In Gummel Pool model, currents are expressed in terms of net integrated charges in the base emitter region. Hence, this model can easily handle non-uniform doping.

The generation recombination effect in the base emitter depletion region at low current level is also accounted in Gummel Pool model. If η is the ideality factor, then the base current injected in to the emitter is

$I_E \propto I_{nE} \propto e^{\frac{qV_{EB}}{kT}}$; As generally large, emitter current injected to the base is not affected by generation and recombination. Hence, $I_C \propto I_{pE} \propto e^{\frac{qV_{EB}}{kT}}$;

For low V_{BE} and I_C the current gainβ is given by,

$$\beta = \frac{I_C}{I_B} \propto \frac{e^{\frac{qV_{EB}}{kT}}}{e^{\frac{qV_{EB}}{\eta kT}}} \propto e^{\frac{qV_{EB}}{kT}(1-\frac{1}{\eta})} \propto I_C^{(1-\frac{1}{\eta})} \tag{4.27}$$

Figures (4.19) shows the dependence of β on I_C in different base region as suggested by Gummel Pool Model. At high current, β decreases due to excess majority carrier in the base and at low injection levels, β deceases due poor injection efficiency.

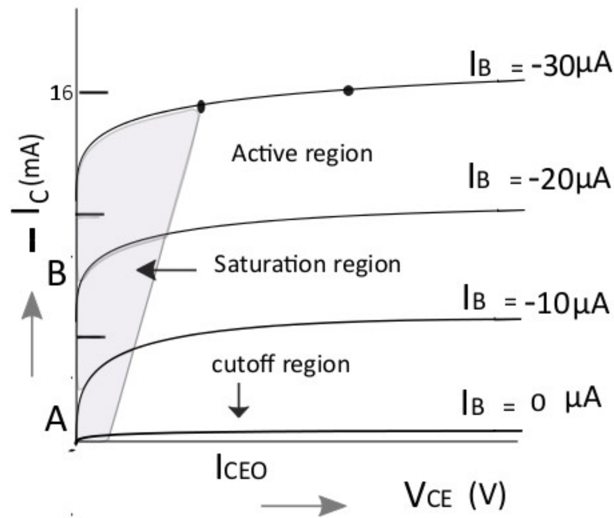

Figure 4.18: Output characteristics of a p-n-p transistor

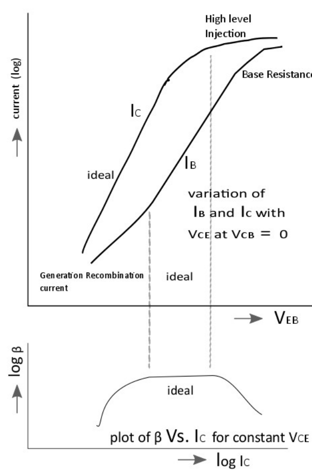

Figure 4.19: (Above)Variation of I_B and I_C with V_{BE}; (Below) Plot of β Vs. I_C for constant V_{CE}

4.4 Charge Coupled Devices(CCD)

A CCD sensor is the first solid state image sensor. It functions to convert light intensity information in to charge, then charge in to analogue voltage. Analogue voltage will then be converted in to digital number

CCD was invented in 1969 by W.S. Boyle and G.E Smith at Bell Telephone Laboratories. The first announcement about the invention was appeared in Bell System Technical Journal[2]. It was first invented as a semiconductor counter part of magnetic bubble memory. But later it became popular as an imaging device and used form digital camera to huge astronomical observatories. A competitor to CCD is CMOS sensor. A solid state device with less power consumption and low cost

Caltech 4 shooter CCD camera system was used to photograph 'Crab nebula' which was used in ground based Hale telescope [3]. This was one among the earliest result obtained using CCD in astronomy.

The solar X-ray Telescope (SXT) camera system aboard the Japanese Solar A space craft utilizes virtual phase CCD from TI, which has sent down millions of images of sun since its launch in 1991 The Chandra Space observatory providing Advanced X-ray Astrophysics facility (AXAF) has a large X-ray telescope that include the advanced CCD X-ray image spectrometer[4]. The Camera has provided high resolution X-ray images of active galaxies, supernovas, quasars etc, simultaneously measuring the energy of the incident X rays.

Operation of CCD

In a three phase CCD, the gates are arranged parallel with every third gate is connected to the same clock driver. Thus one pixel consisted of a triplet of gates. Each gate in the triplet is separately connected to phase1, -2, and -3 of clock. A three phase CCD consists of 2 D array of such triplets.

The charges are created in the depletion layer of MOS capacitor, when intercepted by photons. The name 'charge coupled' has come from the fact that, in the CCD operation the charges stored in the depletion layer of the MOS capacitor is spilled over to the very closely placed adjacent capacitor and thus move about the CCD through proper manipulation of the clock pulses at the gate. A charge to voltage amplifier detects the charges and gives out a voltage

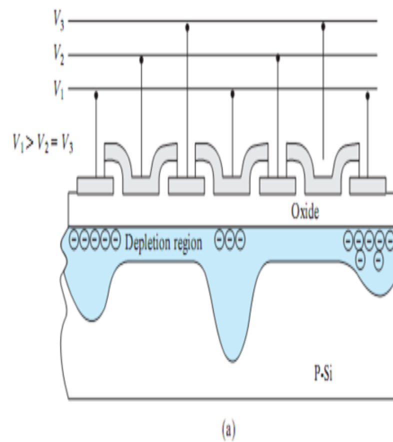

Figure 4.20: Clock voltage determine the the depth of potential well for the collection of charges

pulse. CCD is a serial device where the charge packets are read one at a time.

During integration of charges two vertical phases are biased high (phase-1 and phase-2,say) so that the electrostatic potential in this region become high relative to the third low biased (phase-3) gate. These phases may be called collecting phase as signal electrons are collected in these phases as CCD is exposed to light. The third phase which is biased at a lower potential (at this instant) may be called barrier phase as it separate the charges being collected on either region of this phase. Vertical registers are separated by channel stops formed by potential barrier to prevent spread of signals from one register to the other. See figure (4.20).

In CCD operation clocking is made for vertical shift of charges through vertical registers. For each clock a line of vertical pixels are transferred to horizontal register or serial register. Before the next line of vertical registers is shifted, the horizontal registers are transferred to to the output amplifier from which charges are converted to voltage pulses for readout. The device is serially read out line by line, pixel by pixel to form a serial data of the charge image of the object formed on the CCD when exposed to light reflected by the object.

CCD - Functional details

The function of CCD detector is through the following processes.

1. Charge generation

2. Charge Collection
3. Charge transfer
4. Charge measurement

Charge generation

Charge generation is technically the ability of the CCD to intercept a photon to generate charge. The charge generation efficiency is termed as Quantum efficiency(QE). An ideal CCD will have 100% QE. But in practice QE depends on wavelength showing a remarkable fall in the near infra red region and the blue wavelength region. Charge generation take place in the silicon body of the CCD. When photon interacts with this material, it creates free electrons through photoelectric effect. Interacting photons with sufficient energy will excite electrons in to conduction band. A photon of energy between 1.1 eV and 3.1 eV will generate a single e-h pair while energy above 3.1 eV will create multiple electrons. The quantum yield $\eta = E_{(eV)}/E_{(e-h)}$, where $E_{(e-h)}$ is the energy required to generate on electron hole pair, which for silicon is, 3.65 eV/e^{-}.

CCD respond to a wide spectrum of wavelength ranging from far Infra-red to X-ray. Special optical materials can be used to extend it further[5]. Charge generation in a typical CCD is at a high peak near 6500$\mathring{A}$ and drops off gradually as the wavelength is reduced due to absorption by the gate material. In the UV region, CCD ceases to function properly as the photons are almost absorbed by the gate material. But in the X-ray region near about a wavelength of 10$\mathring{A}$, CCD become again operational making it an excellent X-ray detector.

Special phosphor coatings are made on the surface of CCD to improve the sensitivity of CCD in the UV region. Anti-reflection coating helps to improve QE, as silicon crystal reflects half the fraction of light falling on it.

Charge collection

The amount of charge collected in the CCD depends on the number of charge collecting pixels in the CCD, the charge capacity of each pixel and the charge collection efficiency of each pixel. Today's CCDs have a pixel array size of 4096X 4096 (typically) which give excellent resolution for most of the applica-

tion comparable to a photographic film. Electrons has to be collected by the pixels without spreading to the neighboring pixel. Confining charges to single pixel is an issue of sensitivity . The charge leakage between pixel is called cross talk which is caused by *field free materials* existing farthest from the gate. Charges generated in this region feel a weaker electric field and thus have a higher probability of diffusing into neighboring gate pixels. Cross talk appears when the incident photon spectrum has components of longer wavelength such as near IR as well as near UV shorter wavelength. The near IR wavelength will penetrate deeper in to the silicon while near UV wavelength will not penetrate much. The problem of cross talk could be minimized in back illuminated CCDs.

Charge transfer

The charge transfer is the process of transferring the charge collected by a pixel to its neighboring pixel. This is accomplished by manipulating suitable voltage on parallel sequence of gates. The charge transfer efficiency of todays CCDs are better than 99.9999%. Understanding *charge transfer inefficiency* (CTI) is understanding the charge transfer process. The charge transfers are due to *fringing field* between phases, *thermal diffusion* and *self induced drift*. Out of these, the process of thermal diffusion and self induced drift are slow process. In scientific applications, CCD scan is done at a low rate, so that, the charge transfer due to thermal diffusion and self induced drift will also be accounted in the process. Hence charge transfer efficiency is the most. In other application where the scanning has to be at a higher rate (∼1000 frames / second) CTE will suffer because thermal diffusion and self induced drift require finite time to move electron completely from one frame to the other.

Some CCD will have small number of traps to prevent achieving 100% efficiency. These traps will absorb charges and release them after a delay. Traps near the output amplifier are more disastrous. However traps can be minimized by careful design and fabrication of CCD .

Traps are created in CCDs when energetic particles such as protons, electrons, neutrons, heavy ions or gamma rays hit CCD which is the problem faced by CCDs used in the space mission. However, such traps could be annealed by heating the device number of times cyclically. Bulk traps are due to impurities or lattice defects in the silicon bulk which could be minimized with high purity silicon crystal.

Charge measurement

In CCD operation the charges are clocked onto a small capacitor (Charge sense node) connected with output MOSFET amplifier. The charge to voltage converter amplifier will generate voltage pulses corresponding to the charge stored for each pixel as the charges are clocked on to the charge sense node. The typical charge sensitivity of the output amplifier is $25\mu V/electron$. Read noise has to be reduced to enjoy the charge sensitivity. Thermal noise is generated within the CCD. Dark current is the result of thermal noise. This can be reduced by cooling the CCD. However, the noise coming from the output amplifier electronically cannot be completely eliminated.

4.4.1 CCD theory

CCD is built using the array of MOS capacitors. Charge collection and charge transfer are accomplished using this MOS structure. MOS capacitor is more comparable to surface channel CCDs, Surface channel CCD s are rarely used nowadays. 'Buried channel CCDs' are more common in which an n-type silicon layer is added to a p-MOS capacitor structure forming an n-p MOS structure. Accumulation, Depletion and Inversion are the various bias conditions under which CCD is operated.

4.4.2 Accumulation (When gate is negatively biased)

The structure of p-MOS capacitor is simple. It has a p type substrate, a gate insulator dielectric, and a conductive gate metal composed of poly-silicon. Figure (4.21) depicts the accumulation process in CCD and (4.22) shows the accumulation band diagram.

When gate is given a negative voltage, holes will accumulate at Si-SiO2 interface which forms a highly conductive region near the interface. However, the silicon layer will be at ground potential and a capacitance will be formed due to this effect. The gate capacitance associated with accumulation is $C_{ox} = \epsilon_{ox}/d$, where ϵ_{ox} is the permittivity of silicon dioxide and d is the thickness of the gate insulator.

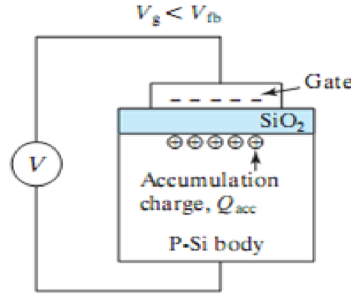

Figure 4.21: Accumulation of charges

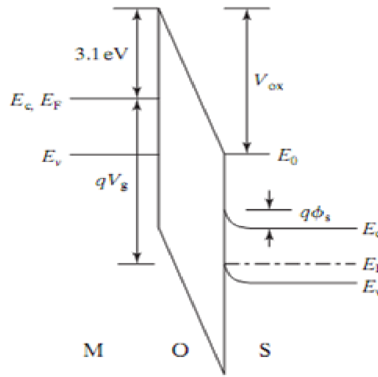

Figure 4.22: Accumulation - Band diagram

4.4.3 Depletion (When gate is positively biased)

As against accumulation, when positive bias is given to the base, the positively charged holes will be driven from the surface forming a depletion layer. The bias condition is shown in figure 4.23 where potential V is plotted against the depth in to silicon region. Refer figure (4.23).

The number of holes driven out could be immediately written as $Q_i = qN_AX_d$ where $Q_i$is the ionized acceptor charge concentration (C/cm^2) beneath the depleted MOS gate. X_d is the depletion depth (cm) and N_A is the acceptor doping concentration ($atoms/cm^3$). The non-conductive depletion region will now act as an insulator with a capacitances of $C_d = \epsilon_{si}/x_d$. The net gate capacitance C_T relative to the substrate in the depletion state is the series equivalent of both oxide capacitance and depletion capacitance. $1/C_T = 1/C_{ox} + 1/C_d$. This overall capacitance determine the clock driver requirements and power dissipation of the CCD. Figure (4.24) depicts the gate bias condition to achieve depletion.

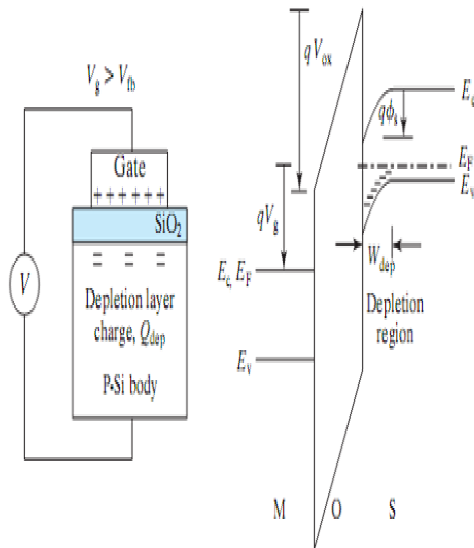

Figure 4.23: Depletion of charges

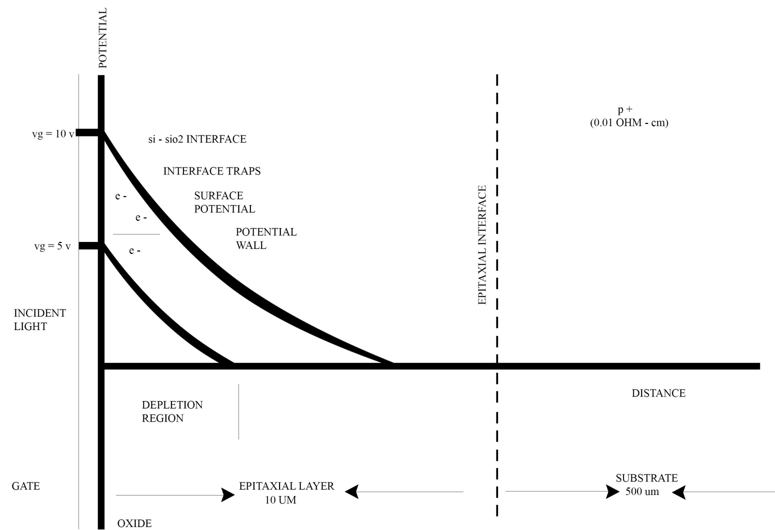

Figure 4.24: Gate bias conditions to achieve depletion

Surface Channel Potential Well

A model for the potential generated in the silicon for the MOS capacitor in the depletion state can be solved using Poisson differential equation. $d^2V/dx^2 = \rho/\epsilon_{SI}$ where V is the voltage and ρ is the charge density. Under depleted state, the value of $\rho = N_A$. Assuming the boundary condition V = 0 , $dV/dx = 0$, at $x = x_d$ and integrating for V , we get $V = qN_A(X - X_d)^2/2\epsilon_{SI}$.

At the $Si - SiO_2$ interface , where the value of x = 0, we find that, potential is greatest. $V_s = qN_A(X - X_d)^2/(2\epsilon_{SI})$ Hence,

$E_s = -qN_A x_d^2/\epsilon_{SI}$;

The voltage drop across the gate oxide and silicon relative to substrate potential is,

$V_G = V_{ox} + V_s$ where V_{ox} is the gate oxide voltage drop. Hence,

$V_G = E_s.d + V_s$. Substituting for V_s and E_s from previous equations. We get,

$V_G = (qN_A X_d/\epsilon_{ox}).d + (qN_A/2\epsilon_{SI}).X_d^2$.

Solving for X_d, the depletion length is,

$X_d = -(\epsilon_{SI}/C_{ox}) + \sqrt{(\epsilon_{SI}/C_{ox})^2 + \epsilon_{SI}V_G/2qN_A}$.

Thus, the depletion length increases with square root of gate voltage for a given doping concentration. When charge is collected by the potential well, the effective voltage on the gate drops .Then, depletion region also become smaller. Thus the effective voltage $V_Q = V_G - q.Q/C_{ox}$; where Q is the signal charge collected at the $Si - SiO_2$ interface (e/cm^2).

Buried Channel Potential well

In surface channel operation, charge is stored and transferred along the surface of the semiconductor. Due to this reason, signal charge is trapped at the $Si - SiO_2$ interface. This will affect charge transfer efficiency of the CCD adversely. Hence, buried channel CCD is introduced.

In the buried channel CCD, charge packets are collected and transferred through the channel region beneath the surface. Due to high CTE of the buried channel

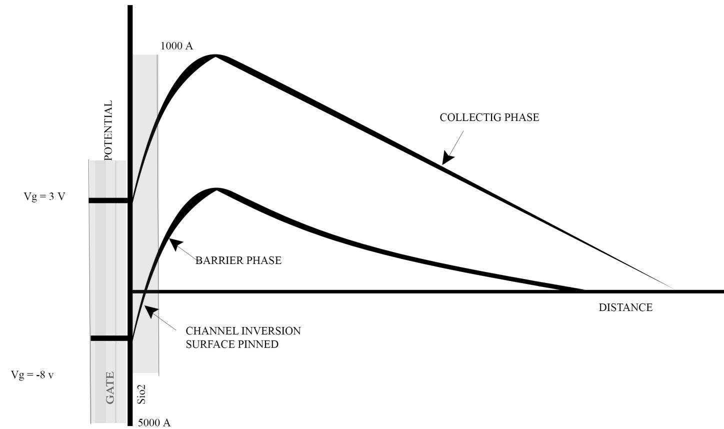

Figure 4.25: Buried channel-potential maximum shown beneath the surface

CCD, scientific CCDs use this technology, in which a thin n region is introduced beneath the surface region. This will shift the position of the potential maximum to the region below the surface layer as shown in figure (4.25).

Buried channel model

Potential distribution in the gate and silicon could be solved using poisson's differential equation. Assuming depletion approximation,$\rho = qN_A$ and $\rho = qN_D$, We write

$$\frac{d^2V}{dx^2} = 0, (inside \quad oxide, ie, -d < x < 0) \tag{4.28}$$

$$\frac{d^2V}{dx^2} = \frac{-qN_D}{\epsilon_{SI}}, (inside \quad channel, ie, 0 < x < t) \tag{4.29}$$

$$\frac{d^2V}{dx^2} = \frac{qN_A}{\epsilon_{SI}}, outside \quad channel, above \quad depletion \quad area, t < x < t + x_p \tag{4.30}$$

Where t is the n- channel depth. qN_D is the charge density of the ionized donor atom. x_p is the depletion width. Applying boundary condition ,

V(x = -d) = V_G - V_{FB},

where V_{FB} is the flat band voltage due to fixed charges in the oxide layer. The condition for the continuity of potential may be written as

$$V(x = 0^-) = V(x = 0^+) \tag{4.31}$$

$$V(x = t^-) = V(x = t^+) \tag{4.32}$$

$$V(x = [t - x_p]) = 0 \tag{4.33}$$

$$\frac{dv}{dx}(x = t^-) = \frac{dv}{dx}(x = t^+) \tag{4.34}$$

The corresponding electric field through each region may be calculated by differentiating V1, V2 and V3. Thus,

$$E_{ox} = \frac{-qN_D x_n}{\epsilon_{ox}} \tag{4.35}$$

$$E_n = \frac{-qN_D(x - x_n)}{\epsilon_{SI}} \tag{4.36}$$

$$E_p = \frac{-qN_A(x - (t + x_p))}{\epsilon_{SI}} \tag{4.37}$$

Since $dv/dx(x = t^-) = dv/dx(x = t^+)$

On integration, we solve the above differential equation as

$$V_1 = V_G - V_{FB} - E_{ox}(x + d); (-d < x < 0); \tag{4.38}$$

$$V_2 = V_{max} - \frac{qN_D}{2\epsilon_{SI}}(x - x_n)^2; (0 < x < t); \tag{4.39}$$

$$V_3 = \frac{qN_A(x - (t + x_p))^2)}{2\epsilon_{SI}}; (t < x < (t + x_p)); \tag{4.40}$$

To get surface potential V_s, put x = 0 ($V_j = V2$)

$Vs = V_{max} - \frac{qN_D}{2\epsilon_{SI}}(x_n)^2$ where x_n is the position of the potential maximum. $x_n = t - x_pN_A/N_D$ where t is the depth of n region and x_p is the depth of depletion region. At $x = t, V_j = V_3$. Hence by the equation above, the depth of depletion region $x_p = \sqrt{(2\frac{V_j\epsilon_{SI}}{qN_A})}$

Electric field is zero at the position of the potential maximum,(V_{max}) where the signal electrons will be collected. ie, at $x = x_n$. When $x < x_n$, electric field is positive on left side of V_{max}, which direct electrons in to silicon. Electric field is negative on right side which directs charges to the surface.

Total capacitance

The effective capacitance $= \frac{1}{C_{eff}} = \frac{d}{\epsilon_{ox}} + \frac{t-x_n}{\epsilon_{SI}}$;

The effective storage capacitance is defined by the capacitance between the gate electrode and the centroid of the signal charge packet. In the absence of potential the effective capacitance is the series combination of the oxide and the depletion capacitance of width $t - x_n$.

4.4.4 Inversion and pinning (When gate is driven negatively)

When CCD gate is driven negatively, the surface potential decreases till it become equal to substrate potential (Vs = Vsub). Holes from channel stop region are attracted and collected at the Si-SiO2 interface. This is the state of inversion, because the minority are populated in the n channel. More negative gate voltage will attract more hole pinning to maintain V_s to be at zero potential irrespective of the applied gate voltage. At this condition, the potential well is not influenced by the gate voltage because the thin layer of holes at the surface is conductive to shield the silicon from gate potential. When inverted, any change in the gate bias goes directly across the gate insulator as a voltage drop.(ie Vox).

Transient events in CCD

When high energy particles are passed through CCD, coulomb scattering may be produced. The particles loose some energy by way to excite electrons to higher orbits of silicon atoms or even to ionize the atom. When ionized, the

electrons will have energies corresponding to conduction band, these electrons will be collected in the potential well giving rise to an image in the CCD. These are the transient events in CCD. Background transients are also present which may be due to radioactive atoms present in the ceramic base of the CCD or due to background radiation at the place.

Annealing

The de-trapping process of the trapped charged particle is known as annealing. The mechanism involved in the de-trapping is known to be either due to tunneling or due to thermal effects. In Tunnel annealing, electrons in the traps near the interface will tunnel into oxide layer and combine with a hole. In Thermal annealing, holes receive thermal energy to escape the trap. Distance of the trap from the interface and depth of the trap are the factors affecting emission constant. The rate of annealing varies with the dose received and the kind and energy of the particle caused the traps. In some cases, the flat band voltage may take days to stabilize.

Reverse annealing

In certain cases dark current and flat band shift increase with time after the CCD has irradiated. The increase continues for long period at constant rate. This is called reverse annealing. [6],[7]. A complete understanding of the mechanism involed in reverse annealing is yet to be clear. There are several proposals. One of the proposal[8][9][10] connected with revese annealing in MOS devices is described below. The radiation induced holes will transport or migrate through oxide layer and interact with weak H bond and break the bond. As a result,H^+ions will be liberated. This ion will drift towards $(Si - SiO_2)$ interface. On reaching interface, H^+ion will pick up an electron supplied by tunneling from the bulk silicon. This will create a neutral H atom (highly reactive). This H atom pull-out another H atom from the passivized hydrogen bond at the interface forming H_2 molecule. Thus a dangling bond is created.

The reaction may be summarized as

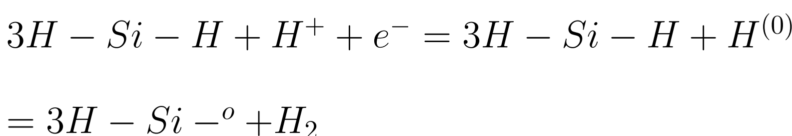

$3H - Si - H + H^+ + e^- = 3H - Si - H + H^{(0)}$

$= 3H - Si -^o + H_2$

$3HSi - H$ is the hydrogen passivized trap and $3H - Si-^o$ is the dangling bond.

4.4.5 Bulk damage

Energetic particle can dislodge Si atom out of lattice position forming an interstitial Silicon atom and a vacancy.(Frankel pair). The displaced atom is the primary knock-out atom(PKA). PKA can induce another knockout, if it has sufficient energy and this can continue to form a defect cluster.

When the energies of the incoming particle exceeds coulomb barrier of the target, they may interact with target atom and emit nucleons as a result of interaction. The emission of the nucleons is compensated by the recoiling of the atom to the extent that, the atom may dislodge from the lattice, creating a vacancy-interstitial pair. The emitted nucleon may further collide with another atom in the lattice, which may displace an atom.

For proton on silicon, non-elastic interaction will take place only when proton energy exceeds 10 MeV. Vacancies move across the crystal.[11],[12]. Most vacancy pairs (98%) combine themselves and do not form a stable defect. But this recombination may be slow. Long term annealing characteristics do occur over a time period of a year or two. The remaining vacancies(2% approx.) form the stable defect. Two such vacancies can combine to form a di-vacancy which are highly stable to high temperature annealing (over 300 degrees. Some times higher vacancy complexes can form. The energy level of these vacancies generally falls in the forbidden level.

Interface traps create energy levels in the band gap which in-turn generate dark current and hence, important. The figure (4.26) is self explanatory to describe how dangling bonds are formed. Silicon atom at the interface back bond to another silicon atom creating an Si-Si bond.(Phosphorous Center). There are open-ended dangling bonds also. Usually, dangling bond are passivated by hydrogen atom at the time of fabrication of CCD. The incorporation of H atom in interface is known as passivation. But, ionizing radiation can easily break these dangling bond or hydrogen bonds. Vacancy is created at the interface. This will produce flat band shift in a CCD and surface dark current in a CCD.

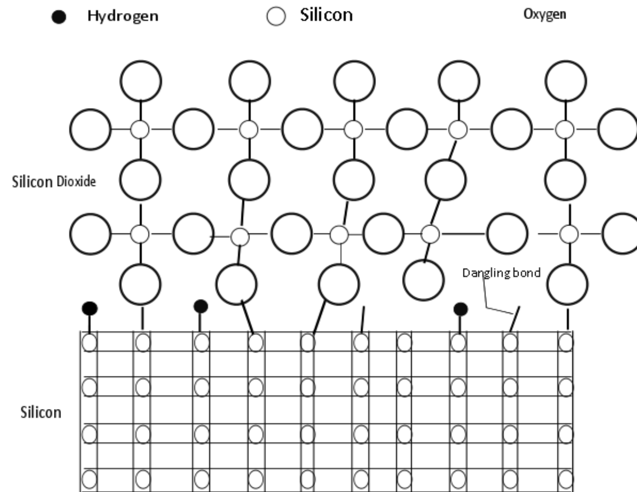

Figure 4.26: Interface state creation. Dangling bonds and H passivated bonds are shown

4.4.6 Space radiation damage to CCD

Radiation Environment in the earth near space region is different from that in the outer space.

Radiation environment near the surface of earth

It is known that, the basic mechanism that determines the earth's local space environment are identified as:

1. Solar events
2. Trapping of particles in the earth's magnetic field
3. Cosmic ray interaction with earth's magnetosphere
4. Interaction secondary radiation in the atmosphere.

Coronal mass ejection (CME) and solar flares accelerate protons and heavy ions towards the earth. There is every chance that these protons to interact with the electronic devices including CCDs in the orbiting satellites, space vehicles etc. The energy of such protons shall be very high in the order of hundreds of MeV. Heavy particles may even have energies in the order of GeV.

The proton fluence in the space is varying . During CME, the proton fluence become very high. Protons get accelerated by very high shock waves by CME.

CME generates solar wind of protons and other particles. Such events will be very frequent and accompanying proton fluence will be at very peak during solar maximum in the 11 year solar cycle.

However, due to the presence of magnetosphere almost all the particles will be deflected by the region saving earth from the bombardment due to this particle. However, outside magnetosphere these particles are every frequent and continuous. Even then during solar events, a significant portion of the particles can have presence below the magnetosphere and interact with space craft. The earth orbiting satellites can experience high doses of radiation over a period of time. This is more of concern in the high altitude orbits.

Van Allen belt is a region of space near the surface of earth where charged particles are trapped by the magnetic field of earth. The particles spiral around the magnetic field lines and moves back and forth across the poles. There are protons, electrons and heavier particles trapped in this region. The protons of this region have energies ranging from 0.5 MeV to 500 MeV. The energies of electrons also high ranging from 0.4 Mev to 8 MeV. But the heavier particles does not have much energy. Hence the threat to CCD is mostly from protons. Even shielding of CCD with Aluminum will not have much effect. The inner belt is the region surrounding the earth from an altitude of 300 km to 25000 km. This belt is composed of mostly protons. The proton of energies above 10 MeV reaches its maximum at an altitude of 7000 km

Since earth's magnetic axis and rotational axis are not aligned , there is a dip in the concentration of charged particles down to the lower atmosphere of earth above South Atlantic region. The charged particles in this region is of most concern to low orbit satellites and air craft

The outer belt is of not much concern to CCD, because this belt consists mostly of electrons. The altitude of this region ranges from 25000 km to 50000 km. The peak energy of the electrons is about 1 MeV which could be shielded by 1 cm of Aluminum. Hence, a threat to CCD from this region can be avoided by shielding CCD by thick Aluminum absorber during the transport of satellite by space vehicles through this region. However, shielding from high energy protons in the space is difficult to achieve.

During solar maximum and solar minimum the fluence from trapped electrons and protons peaks alternatively. The average counts of electrons and protons keep almost a constant over the period. But local variation of counts and fluences from this particle happens during magnetic storm. This is more common

in the outer belt. This radiation is a threat to space craft if its orbit is along the path of such local fluxes. It actually depends, how long spacecraft spend in the region of threat.

Cosmic rays are universal and omnidirectional. It consists of ions of all kind of elements with variation in the elemental abundance. It's energy is immensely high and fluence is found to be at peak during *Solar Minimum* .

There are computer codes which describe space radiation environment. If we give the space mission plan, position and trajectory, mission life time, etc. To calculate the accumulated radiation that may hit the space craft, we have to input the structure of the shielding and material description. The code will ultimately give the split up information of the working radiation environment in terms of total dose and fluence of each particle of interest.

4.4.7 Radiation units

Total dose

The unit of radiation received by a device (CCD) which cause ionization damage is described in terms of total dose. Total dose D is the average energy imparted to unit mass of the device.

$D = dE/dM.$

Radiation absorbed dose (RAD) is a unit of total dose.

1 RAD = 100 ergs/ gm = 0.01 J / Kg;

Grey (Gy) = 1 J/Kg. = 100 RAD

Same dose of protons and gamma rays will have different effect on CCD. Protons will induce more Bulk damage and less ionization damage while Cobalt-60 will produce ionization damage and less bulk damage. Hence, ionization damage and bulk damage are determined separately

Dosimeters

To measure total dose imparted to CCD, Si diodes, Calorimeter, Thermo-luminescence detector etc. are used. CCD itself can be used as a detector to measure the dose received when there is no bulk damage to CCD

Measurement of particle radiation dose

Fluence is a used in measuring particle dose. If F is the Fluence of the particle the corresponding dose can be calculated using the formula $D = K.F.S$ where K is a constant $= 1.6 \times 10^{-15}$; S is the stopping power of the particle; $S = dE/dX$, where the energy exchange dE is measured in $(MeV cm^3/mg)$ and dX in cms.

Stopping power may be converted to energy loss /unit length. for example, in CCD, energy loss $1eV/\mathring{A} = 2.32\times$(Stopping Power). Stopping power of a particle in silicon depends on the type of the particles and the energy. Region of maximum energy transfer for proton and CCD take place at the region of Bragg;s peak.

Source of X-ray

In our experiments, we used Fe^{55} X-rays to characterize CCD. X-ray can be shielded by using aluminium mask. We used mask to shield X-ray limiting it to fall only on one quadrant of CCD.

There is other advantage of using Fe^{55} for CCD characterization. Fe^{55} X-ray is mono-energetic. Range of Fe^{55} X-ray in silicon is 0.4 micrometer. The dose absorbed by the gate dielectric is different from that of the silicon bulk. This is called *dose enhancement.*

Dose enhancement $= \sigma_{Si}/\sigma_{ox}$; where σ_{Si} is the cross section of Si to the X-ray events and σ_{ox}, that for oxide. For Fe^{55} , 5.9 KeV X-ray on Silicon, the cross section is 1.45 cm^2/ gm and for the oxide = 106 cm^2/gm.

The dose relationship between the gate dielectric and the epitaxial region is $D_{Ox} = \frac{\sigma_{Ox}\rho_{Ox}}{\sigma_{Si}\rho_{Si}}$ where density of oxide $\rho_{Ox} = 2.2$ gm/cm^3 and that of silicon ρ_{Si} is 2.32 gm/cm^3.

Ionization damage

The number of e-h pair generated in the oxide layers is proportional to oxide volume. Hence, Oxide thickness become one of the important parameter. .The Field Oxide in the Channel Stop Region is very much thicker than gate oxide region. Radiation experiments have shown that there is a large flat band shift at the interface between this oxide region. The type of gate dielectric is also an important parameter causing ionization damage. SiO_2 and Si_3N_4 have good radiation tolerance. Radiation damage tests are conducted using thick and thin field oxide devices to compare the influence of oxide thickness in the ionization damage produced. UV charging is another method to study the ionization damage caused to the device. The principle of this method is that, negative flat band shift caused by ionizing radiation could be reversed by UV radiation.

Displacement damage

The displacement damage is very low as the particle pass through silicon. The probability of interaction can be understood in terms of the mean free path. The mean free path of 1 MeV proton is $\lambda = \frac{A}{N_A \rho \sigma}$ where σ is the is the interaction cross section. For 1 MeV proton $\sigma = 3.5X10^-20cm^2$. ρ is the density in gm/cm^3. The value of $\lambda = 5.74\mu m$. Mean free path is very large. Hence, probability of interaction is extremely small. If we assume no ionization loss, the range of protons (1 MeV) is calculated to be 27.3 cm. But due to the ionization loss, the actual range is only in the order of micro meters. This shows that, ionization loss is much greater than NIEL.

When displacement of atom occurs from the lattice position a vacancy interstitial pair is created along with liberation of energy. The displacement energy $E_p = \Lambda E_T$. Here,E_T is the threshold energy for proton (eV) and $\Lambda = \frac{4Am_p}{m_p + A^2}$ where A is the atomic weight (28). The displacement cross section $D_T = \frac{N_A \sigma N_{pri} x}{A}$ Where D_T is the displacement of the particle; A is the atomic weight of the target (g/mole), σ is the particle cross section; x is the path length, ρ is the silicon density and N_{pri} is the primary knock out.

4.4.8 Bulk damage equivalence

Radiation tests performed on different CCDs have established that, NIEL/SRIM curves are capable of predicting CTI degradation using single equivalent proton energy. A radiation environment can be sampled by allocating energy bins and the fluence of a definite particles belonging to that bin in a tabular form as as in

The displacement due to the protons with energy corresponding to each energy bin at a definite fluence is studied and tabulated corresponding to the bin number. The $displacement/cm^2$ is the product of fluence and displacement.

The average displacement /proton is the ratio of the total displacement caused by various protons in the radiation environment and the total number of protons in the environment. The energy of a single photon producing the same displacement / proton can be obtained by interpolation from proton transfer data. The fluence of the proton could be then estimated for the required displacement corresponding to radiation environment.

In the radiation test performed on CCD, the data obtained for the space radiation environment for the specified space mission plan is used create the radiation environment data. The tests performed on CCD are usually made with an equivalent fluence of single energy proton in the lab.

CCD characteristics and measurements are done to investigate Quantum Efficiency (QE), charge collection efficiency (CCE), and charge transfer efficiency(CTE). Measurements are done as an average over a number of pixels. The limitations to these measurements are the variation in the intensity and stability of the source and also the variation of the focus of the beam. But, CCD Characterization using X-ray photons can overcome these limitations. In contrast to visible light, charge generation due to X-ray are very much localized. Typically, charges generated by X-ray photons are limited in the pixel on which the X-ray photon hits. However, a photon may be rarely absorbed below depletion region which may diffuse to neighboring pixel. The result is the degradation of CCE. An imperfect charge transfer from the target pixel to lag during successive transfers will cause the X-ray events recorded with a tail due to delayed charge. The size and shape of this tail is an indicator of CTE performance. Thus, X-rays is used to characterize the CCD performance such as CCE and CTE.

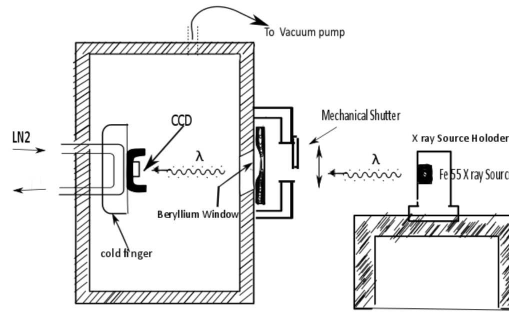

Figure 4.27: Experimental setup to expose CCD to Fe^{55} X-rays

Source of X-ray used for the study

Fe^{55} Soft X-ray has become the standard source for the measurement of CTE. During the radioactive transfer of Fe^{55} in to Mn, K electrons are absorbed by the nucleus. An X-ray is generated when the electrons drops from either L or M shell to fill the empty K shell. These are known as Kα rays. Photoelectric absorption of Mn X-ray by CCD ejects an electron of energy $(E - b)$, where E is the energy of X-ray and b is the binding energy of K shell electron of silicon. $(E - b)$ = (5.9-1.78). This photo electron will produce electron hole pairs through elastic collision with orbital electrons of other silicon atoms creating approximately (5900-1780)/3.65 = 1128 number of electron hole pairs. This is known as $K\alpha$ line. $K\beta$ primary line and escape peaks are generated in the similar way. Escape peak is the result of *silicon X-ray* (generated by dropping of electrons in to vacant K shell). This X-ray get absorbed by some other silicon which in turn either generate 1780/3.65 = 487 electrons or escape from CCD.

Hence there are five prominent signals generated by Fe^{55} X-rays. Figure (4.27) shows the experimental setup used for the source of X-ray. Figure 4.28 shows a typical Fe^{55} X-ray spectrum.

- Kα line 1620 e^-
- Kβ line 1778 e^-
- Kα escapes peak 1133 e^-
- Kβ escapes peak 1291 e^-
- Silicon line 487 e^-

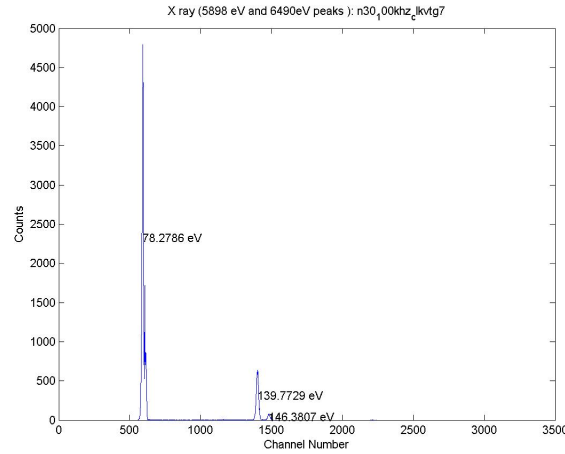

Figure 4.28: Fe^55 Spectrum

Theoretical limit of energy resolution or Fano - noise limited performance

Fano noise is the statistical uncertainty due to absorption of energy by the silicon lattice. The fano factor is therefore related to FWHM of the histogram and average energy expended to produce an e-h pair.

FWHM (eV) = $2.355[E(ev).E(e-h).Fa]^{1/2}$. Where E(ev) is the photon energy and F_a is the fano factor. The typical value of fanofactor for silicon is 0.1.

4.4.9 Generation of charge in a CCD

The charge generation in CCD is due to photo electric effect. Photo electron are responsible for the generation of e-h pairs. For the generation of charges, it has to be ensured that the incoming photons should interact with photosensitive volume of the CCD. The number of electron hole pair generated due to a photo electron is the quantum yield η depends on the energy of photo electron and other physical parameters of CCD. Quantum Efficiency QE is related to quantum yield as $QE = \eta.QE_I$ where QE_I is the interacting quantum efficiency. QE_I is the fraction of photons that is absorbed by the CCD to produce e-h pairs. Being a fraction the value of QE_I will always be less than 1. But the value will be usually large so that QE will be always larger than 1.

The causes of QE loss are identified to be the gate absorption, reflection loss and transmission loss. The photons have to pass through poly gate before they can interact with epitaxial layer. Reflection loss is applicable over a wide spectrum of wavelength. Transmission loss is important for very long and very

short wave length photons which can pass through the epitaxial layer without interaction

4.4.10 Dependence of operating temperature on QE performance

As the temperature is decreased, the photon absorption length (LA) increases. K Rajkanan and R singh explain that this is due to the increase in silicon band gap.[13],[14],[15].This characteristic is especially important in near infra red [16]. Because QE characteristics in these wavelength increases by 3.6 times over a temperature difference of 100 degrees..

4.4.11 Effect of Channel stop region in the charge generation process

When charge is generated in the channel stop region, recombination will take place. Hence charge effective charge generation is limited in this region. Even though the volume of this region is less, its effect on QE is noticeable for certain wavelength region. However, for back illuminated CCDs the channel stop has little effect on QE for any wavelength.

4.4.12 Virtual phase CCDs

CCDs show a very poor response to UV region because of the absorption at polysilicon gates. The problem could be circumvented either by using thin back illuminated design or by using UV sensitive organic phosphor coatings. Virtual phase CCDs [17][18][19] on the other hand, solve this problem, by leaving half pixel open by leaving a *virtual electrode* . This will allow the photons to enter the pixel without much absorption. Virtual phase uses 4 doped regions. Regions 1 and 2 are clocked regions. By implanting suitable n dopant, a potential step is created between region 1 and 2 so that region 1 become the *barrier* and region 2 become the *well* . Region 3 and 4 makeup *virtual phase* . Region 3 is the *virtual barrier* and region 4 is the *virtual well* . These are achieved by suitable implant of sufficient dose. Hence a step in potential is created between regions 3 and 4. A heavily p type Pinning implant is provided just below the surface region to allow the pinning of the virtual phase to ground potential. In *virtual phase* CCD the charge integration take place either under

the clocked phase when the applied voltage is high or under the virtual phase at low bias. And the charge transfer from the clocked phase to virtual phase and from virtual phase to next clocked phase take place switching the gate voltage between $-V_G$ and $+V_G$. The virtual phase CCD are superior in perfomance and reliability due to its structure and inverted mode of operation(generates less dark current). The technology is high yielding. Lesser number of clock lines required for its operation simplifies the drive electronis to a greate extend compared to multiphase CCD. However Virtual phase CCDs are difficult to fabricate due to larger number of implants with high precision is required.

Charge collection is a function of CCD before they are clocked in to the sense nodes. The capability of charge collection widely varies depending on the technology used. Well capacity is the measure of charge that could be hold by a pixel. The technology of CCDs was undercontinuous refinement to improve the well capacity. Presently, Charge collection capacity even up to $8000e^-/m^2$ has been achieved.

Charge diffusion is also a parameter which affects charge collection capacity. Charge diffusion is the process of charge spreading in to the neighboring pixel or the region of the CCD that lies outside the depletion region. This will diminish the ability of CCD to reproduce the image sharply. Charges that escape from the target pixel also causes charge collection problem.

High charge collection efficiency will lead to high signal to noise ratio since S/N ratio of an image is increased by the square root of full well or well capacity. Well capacity is given by,

$$Q_{FWC} = N_D(t - x_n) \tag{4.41}$$

Where Q_{FWC} is the well capacity, N_D is the buried channel doping concentration and $t - x_n$ is the distance between the surface of CCD and the position of the potential maximum corresponding to empty potential well. The position of the potential maximum will move towards the surface as the charge fills the well.

When the potential maximum (V_{max}) of the collecting phase of a pixel become equal to the barrier phase of the adjacent pixel, the signal charge will spill in to the neighboring pixel . This will cause charge spreading called blooming. This state of the CCD is called bloomed full well state. The bloomed Full Well

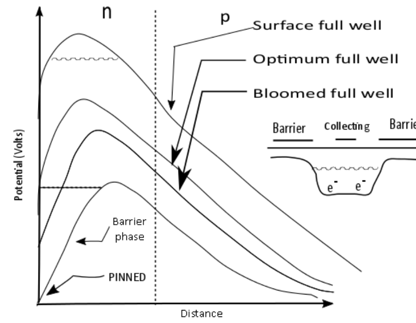

Figure 4.29: Optimum full well bias condition for collecting phase

Capacity $Q_{BFW}$is given by

$$Q_{BFW} = \frac{C_{eff}V_{CB}}{q} \tag{4.42}$$

Where C_{eff} is the effective capacitance, V_{CB} is the gate potential difference between collecting and barrier phase ($V_C - VB$). Increasing the clock voltage will increase the value of V_{CB} which in turn increase the value of full well capacity. But this is not limitless, as the increase in gate voltage will shift the potential maximum V_{max} towards the surface.

Hence, charges when fills the potential well, get opportunity to interact with $Si-SiO_2$ interface states before blooming occurs. However, due to this interaction or overflow of charges, the full well limit is considered to be exceeded. The full well at this stage is known as surface full well (SFW). The buried channel CCD now become a surface channel CCD. The optimum Full Well Capacity is the mean of BFW and SFW. During optimum full well the barrier is inverted and pinned as in figure (4.29)

Charge Collection Efficiency is based on X-rays is defined as the ratio of the average charge collected by the target to the theoretical level.

Absolute $CCE = \eta_E/\eta_i$ where η_E gives effective quantum yield and η_i is the ideal (theoretical) quantum yield[20]

4.4.13 Charge transfer

Charge transfer is an important function of a CCD by which a CCD transfers transfer the charges from one pixel to the adjacent pixel. Charge transfer efficiency is the ratio of the charge transferred to the target pixel to the initial charge stored in the transferred pixel. Typical CTE for a scientific CCD shall

be 0.99999. The lost charges from the target pixel reach the sense node at the output with a delay. Charge transfer Inefficiency (CTI) is the complement of CTE.

CTI = (1-CTE). Theoretically the amount of charge that is lost for the N stage CCD register is [21]

$$S_{N_p} + n = \frac{S_i N_p!(1 - CTI)^n CTI(N_p - n)}{(N_p - n)!n!} \tag{4.43}$$

Where Np is the number of pixel transfers and n is the trailing pixel number that follows the target pixel. S_i is the initial charge contained in the target pixel $(e^-)S(N_p + 1)$ is the charge contained in the$(N_p + n)^t h$ trailing pixel.

When N_p is very large and CTI is very small, then $N_p CTI = \lambda$, a very small and finite value. Hence , binomial (N_p, CTI) in the above equation can be replaced with Poisson (λ) equation. Hence,

$$S_{N_p} + n = \frac{(S_i(N_p CTI)^n e^(N_p CTI)}{n!} \tag{4.44}$$

Typical value for Si is $1620e^-$. When $N_p = 1/CTI$, we have , the charge stored in the target pixel ($n = 0$) become equal to the charge stored in the trailing pixel ($n = 1$). This means that, for every N_p number of charge transfers, there is a level shift by one pixel

4.4.14 The mechanism of charge transfer

Thermal diffusion, self induced drift and fringing field effect are the mechanism explained for charge transfer. [22]

Thermal diffusion and fringing fields transfer small charge packets. The charge transfer mechanism is as follows. To begin with, consider a large packet in a collecting phase. Next, the neighboring barrier phase is switched in to high and become a collecting phase. The charges that were in the initial collecting phase will be moving in to the new collecting phase by electrostatic repulsion (self induced drift). Immediately the original collecting phase will become a barrier phase. Now electrostatic repulsion begins the charge transfer. However, as the

charge density is reduced, self induced drift become less effective to transfer the charges. However, the remaining charge will be transferred by fringing field or by thermal diffusion.

The shape of the clock pulse is made with slow rise time and fall time for proper charge transfer without blooming effect. slow rise time/fall time give enough time for charges to diffuse without blooming. Thermal diffusion decays exponentially with transfer time.

The fraction of charge that remains under a phase during transfer time t is [23] $CTI_D = e^{-t/\tau_{th}}$

Where τ_{th} is the diffusion drift time constant. τ_{th} is inversely related to mobility and temperature mobility increases with decreasing temperature. Lattice scattering decreases with temperature. Decrease of lattice constant increase the mobility . The overall effect that, the mobility increases with decreasing temperature. Hence, the diffusion time will increase with KT.

Self induced drift has 1/x time dependence, because the field strength decreases as the charge is decreased. The process is not exponential. The fractional charge remaining after a transfer time t caused due to self induced drift is [24]

$CTI_{SID} = (1 + \frac{t}{\tau_{SID}})^-1$ The fractional charge remaining after a transfer time t due to fringing field is [25] $CTI_{FF} = e^(- t/\tau_{FF})$

4.4.15 Measurement of Charge transfer efficiency

$$CTE_X = (1 - \frac{S_D(e^-)}{X(e^-)N_p}); \tag{4.45}$$

where$S_D(e^-)$ is the deferred charges, $X(e^-)$ is the X-ray signal ($1620e^-$) for $Fe^5 5$ andN_p is the number of pixel transfers.[26]. The X-ray events interacting farthest from the on chip amplifier experience greatest charge loss.

CTE measurements using X-ray transfer is limited when CTE value ¿ 0.99998. Hence other methods are followed.

4.4.16 Charge Injection for CTE measurements

It is possible to electrically inject charge in to the multiphase CCD [27] with bi-directional clocking facility. The charge injected at one pixel can be moved horizontally back and forth to provide several number of pixel transfers and the charges are finally measured . The total number of pixel transfers and total charge loss can give CTE.

4.4.17 Traps

The CTE performance of a CCD is limited by the traps located in the signal channel. Charges will be attracted to these traps and released after a delay. Traps are of different types and nature.

Improper design features that produce a small potential barrier can hold signal charge. This may be called a design trap. The traps will extract a fixed quantity of charges from the signal which are to be released later tot the trailing pixels. The deferred charges will cause a tail to the point source image. Traps will deteriorate CTE to a greater extend.

Various techniques are employed to avoid design traps One way is to modify the shape of the signal carrying channel by providing constriction at the ends of the channel, instead of having a *bump* at the middle . Process induced traps are the second kind of trap. There are *localized traps* and *Spurious potential packets* induced during process. Localized traps are randomly distributed and isolated to single pixel. Spurious potential packets are due to improper shape of the potential well or or well depth within the channel[28].

All CCDs exhibit channel non-uniformity to some degree. Due to fringing field effect , this small variation in potential will not be accounted during transfers. Large CCD imagers are more affected by Spurios traps as there are several transfers.

Spurious traps can be reduced by increasing the fringing field effect. This could be achieved by elevating clock drive. The second method to go for highest operating temperature possible to collapse the charge packets due to Spurious traps. Slow clocking shall give enough time for the charges to release from the trap before the transfer. Another method shall be the addition of Fat-zero charge which fills the traps before the signal overrides through it.

Localized traps can cause serious effects on CTE. The traps are capable of holding a few number of electrons to thousands of electrons. Its presence in horizontal column can make CCD for no use. X-ray stimulation is the best method to identify traps in horizontal column. Horizontal traps could be identified by exposing CCD to low flat field of white light and reading out CCD. Large traps may require many transfers before they get filled.

Bulk traps are due to impurities or lattice defects in the crystal. A single bulk trap can hold only one electron. However, collective effect due to several traps can affect global CTE. However, high purity silicon material used for making CCD can solve the problems due to bulk trap.

The trapping and de-trapping due to bulk state depends on various factors like temperature, clock rate, trap depth etc. These factors are included in the equation [29]

$$CTI = qN_T.V_v exp(-\frac{t_{PT}}{3\tau_e})[1 - \frac{t_{PT}}{3\tau_e} - \frac{N_z t_{PT}}{\tau_e}] \tag{4.46}$$

N_T = Bulk trap density ($traps/cm^3$)

V_v =Volume of the charge packet in the potential well(cm^3)

t_{PT} is the pixel transfer period(sec)

N_z = Average number of empty pixels between x ray events (pixel / X-ray event)

τ_e = Emission constant ; $\tau_e = \frac{exp(E_T/(KT))}{(\sigma_n v_{th} N_c)}$

σ_n = electron trap cross section

N_c is the effective density of states; v_{th} is the thermal velocity of the electron= $\sqrt{3KT/me*}$ and E_T is the trap energy level below the conduction band.

4.4.18 Fat-Zero compensation

It is possible to nullify the effects of the design traps and process traps by supplying flat field optical signals to the level which satisfy the traps to be filled by the charges. Signal charges can override the traps without being trapped.

This technique is known as Fat zero compensation. Fat Zero charges also can be injected electrically using input diode.

4.4.19 Measurement of charge

A sense capacitor at the end of the horizontal register is connected to Charge to Voltage Amplifier system. The signal charge is dumped in to sense capacitor. Corresponding voltage is generated by the amplifier. Amplifier is the only active component as a part of CCD and the only component which introduce noise in to the system. Thermal noise will appear as dark current which also get amplified by the CCD. However, this noise can be reduced by cooling CCD. The various types of noise introduced by the output amplifier include reset noise, white noise, flicker noise, shot noise, Contact noise etc. Knowledge of these noises is important while doing experiments with CCD.

Johnson described thermal noise in terms of random noise power. Noise power exists in all conductors with a magnitude proportional to operating temperature . According to Nyquist, the rms noise voltage Power $V = \sqrt{4kTBR}$ where k is the Boltzman constant, T is the temperature and R is the resistance and B is the noise band width. The charge carriers can rapidly react to thermal agitation. The noise generated in different types of resistance such as contact noise (1/f noise) is due to in-homogeneity of particles in the composite material or thin film. White noise is random and has a Gaussian probability distribution. Reset noise is due to the periodic resetting of the sense node by the reset MOSFET. White noise is generated by output amplifier MOSFET. Flicker noise or 1/f noise of the output amplifier. Noise power is inversely proportional to frequency. Flicker noise is generated by surface interface states and arise because of the disruption of silicon at the surface. [30] .There are techniques to reduce flicker noise such as using crystal orientation (100) instead of (111), formation of SiO2 at the surface at high temperature etc all of which are employed in CCD.

Flicker noise generated by the noise interface states can be approximated by the equation[31]

$E_n^2 = K_1\tau_e/(1 + 2f\tau_e)^2$; where,$E_n^2$ is the noise power τ_e is the emission time constant.

$f_{3dB} = \frac{1}{(2\pi\tau_e}$ where f_{3dB} is the half power noise frequency.

From the above equation we find that noise power increases as emission time

constant increases. Deep traps causes lower frequency noise as against shallow traps. The trap energy levels at the interface mostly falls in the energy region of band gap and therefore interface states are uniformly distributed in the band gap. Hence exhibit a uniform distribution of time constant as evident from the 1/f noise signature in the noise spectrum.

Correlated double sampling is a method employed to minimize the noise. A technology often applied in CCD video systems.

Bibliography

[1] Sheng. S. Li. Semiconductor Physical electronics. Second edition. Springer p(338-357).

[2] W. Boyle and G smith Charge Coupled Devices Bell System Tech J. Vol 49; pp587-593 (1970).

[3] J Gunn etal;Optical Engineering vol 26, p 779(1987)

[4] Burke etal;Soft X-ray CCD images from AXAF; IEEE tran. Elelct. Dev. Vol 44 No 10 1633-42;(1997)

[5] D Schoder,Two phase germanium charge coupled device; Appl. Physics lett. Vol,25, No 12 (1974)

[6] Janesick, K kalaasan and T Elliot, Charge Coupled Device Charge collection efficiency and the photon transfer technique, Optical Engineering, Vol 26, No 10(1987)

[7] D. Barbe imaging devices using the charge coupled concept Proc. IEEE Vol 63 pp 38-67

[8] Phy Rev. B Vol , 7. No.10 P 4587;A radiation hard MNOS CCD for Low temperature application IEEE trans. Nucl. Sci. Vol. NS-26 No .6 (1979)

[9] N. Saks, J. Killiany , W.Baker " A radiation hard MNOS CCDfor low temperature application" IEEE Trans. Nucl. Sci.Vol(40) No 3,(1993)

[10] H Tada,J carter, Solar cell radiation hand book; JPL Publication 82-69 (1982)

[11] H Tada,J carter, Solar cell radiation hand book; JPL Publication 82-69 (1982)

[12] H Tada,J carter, Solar cell radiation hand book; JPL Publication 82-69 (1982)

[13] K. Rajkanan, R Singh and J Shewchun Absorption coefficient of silicon for solar cell calculation, Solid state Elec. Vol 22,pp 790-795(1979)

[14] G Macfarlane etal; Fine structure in the absorption-edge spectrum of Si Phy Rev vol 111 pp 1245- 1254.

[15] R . braustein , A moore and F herman, Intrinsic optical absorption in germanium silicon alloys, Phy rev. Vol 109No 3 pp 695-710(1958)

[16] V. Roberts etal; infra red absorption of silicon near the lattice edge Phy Rev. Vol 98,PP 1865-1866

[17] J Hynesec," Virtual phase charge transfer devices," US patended (No. 4229752)

[18] J. Hynesec, " Virtual phase technology: A new approach to fabrication of large area CCDs," IEEE trans.Elelctron devices Vol ED -28 No 5 (1981)

[19] J. Janesec etal; "A virtual phase imager for Galileo", proc. SPIE Vol 290(1981).

[20] J. Janesick, K kalaasan and T Elliot, " Charge Coupled Device Charge collection efficiency and the photon transfer technique," Optical Engineering, Vol 26, No 10(1987)

[21] D Buss, A Tasch and J Barton Application to signal processing in Charge coupled devices and systems, M. Howes and D. Morgan Chapter 3. pp 105-107 John Wiley (1979)

[22] E. Banghart, etal; A model for charge transfer in buried channel charge coupled devices at low temperature IEEE Trans. electron devices, Vol 38, No 5(1991)

[23] J. Carnes etal; Free charge transfer in charge coupled devices IEEE Trans. Electron devices Vol ED 9 No 6 pp 798- 808

[24] D. Barbe "imaging devices using the charge coupled concept " Proc. IEEE Vol 63 pp 38-67

[25] J. Esseer The peristaltic charge coupled device for high speed charge transfer, 1974, IEEE International solid state circuit conference of technical papers. Pp 38-29

[26] J. Janesick etal; Fano noise limited CCDs Proc. SPIE Vol 982 pp 70-85(1988)

[27] J. Orbock, D seawalt et al ; Charge transfer efficiency measurements at low signal level on STIS/SOHO TK 1024 CCDs. Proc.SPIE Vol 1242(1990)

[28] G. Tailor and P Chatterjee An evaluation of sub micrometer potential barriers using charge transfer devices,IEEE Journal of Solid State Circuits Vol. SC 18No(4) 1980.

[29] K Kim,Physics of charge coupled devices.In charge coupled devices and system. P 58, John Wiley(1979

[30] G. Alers et al; Tunneling current noise in thin gate oxide Appl Phy.Lett, Vol (69) No 19 (1996)

[31] E. Simoen and C Claeys, On the Flicker noise in sub micron siliconsilicon MOSFETs. Solid state Elelctronics Volume 43 pp 865-882.

[32] S. Sze. Physics of semi conductor devices john Wiley.p 385 (1981)

Chapter 5

Tools and Techniques Used

5.1 Common Tools and Techniques Used for the Study of Radiation Damage on Electronic Devices

5.1.1 SRIM and TRIM

In experiments, which include passage of energetic particle through material, it is very much useful to simulate certain situations using SRIM for the proper design of experiments. SRIM is the abbreviation of Stopping and range of ions in matter. This is a collection of computer codes wrapped in to GUI that calculate the interaction of ions with matter. It has been built around TRIM, a computer code that calculates the Transport of Ions in Matter . SRIM is used in many areas of radiation material science and ion implantation researches and applications. The program was developed by J.F. Zeigler and J.P. Biersack [1,2] . The first version came in 1983. In every 5 years the programs get upgraded to accommodate the latest data and to make it compatible with new computer technology and operating systems. SRIM is based on Monte Carlo Simulations namely binary collision [3] approximation with a random selection of impact parameter of the next colliding ion. We need to input the type of ions with energy, the type of target with thickness. Multiple target layers are also possible. The output of the program could be obtained as list or it is possible to get the output in the form of plots. Fig 5.1 shows a typical simulation generated by SRIM for 1 MeV proton.

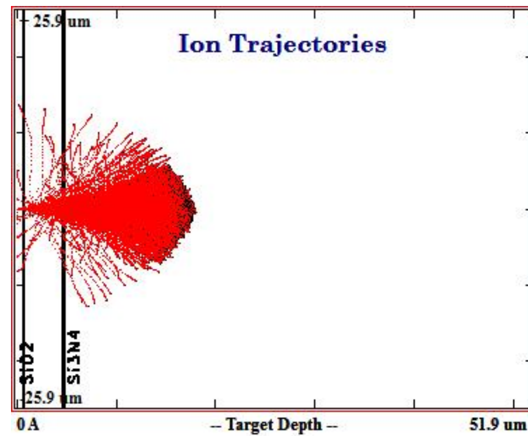

Figure 5.1: SRIM simulation showing 1 MeV proton trajectories in CCD 236

SRIM has been developed based on the modeling and parameterization of a large number of experimental data. SRIM does not take in to account of the crystal structure or the dynamic change of materials which limits its use in some cases. The other features of the code are:

1. It can give the three dimensional spread of ions in the solid such as penetration depth and horizontal straggling etc.
2. It gives concentration of vacancies, sputtering rate, ionization and phonon production in the target material.
3. Nuclear energy loss and electronic energy loss are partitioned and calculate rate of energy loss
4. Allow calculation of electronic stopping power of any ion in any material, even for the gaseous target

It is worthwhile to understand the approximation used in the code before using it for scientific work.

1. The crystal structure of the material is neglected, considering every material to be amorphous[4]
2. The binary collision is simplified without considering the influence of the neighboring atom
3. The material could be layered only in 2D. 3D combination of the material could not be used in calculations

4. The interstitial atom may recombine with vacancies. This effect is neglected.[5]

5. The radiation induced amorphization is not considered, even though this is very important in semiconductors

6. The electronic stopping power and the interaction potential are all not based on the theoretical calculation. But depends on the averaging fit basing experiment and other calculated data.

7. In the case of sputtering, the surface barrier crossing of the target atom is assumed to depend only on the energy and momentum of the atom. The chemical effects are neglected.

8. Anisotropic behavior of crystals is neglected while calculating threshold displacement energy.[6]

Current version of the SRIM works on many operating systems including Windows.

5.1.2 GEANT 4

In high energy applications such as nuclear accelerator physics, space physics and medical physics, GEANT 4 is more useful to simulate the passage of particles through materials. The development of GEANT 4 was started at CERN which then entered in a worldwide collaboration. It is useful for a range of applications in high energy physics and engineering. Space Physics groups use this program to study response of electronic instruments, thereby enhance the optimized shielding of space radiation, component effect etc. GEANT 4 is very much useful in developing space electronics and space science detector system. It can be used to simulate the radiation hazards caused to spacecraft crew , Analysis of magnetosphere propagation of Cosmic rays, micro - dosimetry, large scale simulation etc. It is also a good tool for shielding optimization. The experimental environment could be modeled in GEANT 4. Figure (5.2) shows the experimental environment created for simulation of the irradiation of CCD at TIFR. The dimensions of the experimental chamber and its surrounding are important for the correct simulation of gamma radiations produced due to scattering of proton by the target and subsequent irradiation of CCD by the scattered protons.

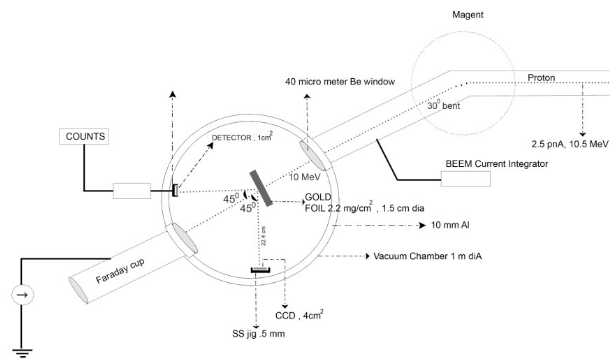

Figure 5.2: SRIM simulation showing 1 MeV proton trajectories in CCD 236

5.1.3 SPENVIS

SPENVIS system is a very useful for the space environment modeling. It is internet based tool, accessible to all. The trajectory, orbit and mission period of space vehicles are important for the calculation of space radiation hazards caused to the instrument.. It consists of an integrated set of models of the space environment. It provides help pages on the models in addition to the SPENVIS system. The SPENVIS system requires input parameters stores in a file, so that, the analysis can be performed in more than one session without losing input or output data. There is a project page to manage a runs in a simulation. SPENVIS requires creating a set of points on the space trajectory and another set of points geographic points as the input. These points are generated by the built in tools such as Orbit generator and Co-ordinate grid generator. Once the trajectory has been generated, the same data can be used by different models. The various models implemented in SPENVIS has been organized in the following packages below. The various models are:

1. Radiation sources and effects
2. Accumulation of charge on space craft
3. Atmosphere and ionosphere
4. Magnetic field
5. Meteoroids and debris
6. Database queries

7. Miscellaneous

With SPENVIS, one can generate a space craft trajectory or co-ordinate grid and then calculate

1. Geomagnetic coordinates
2. Trapped proton and electron fluences
3. Radiation doses (ionizing and non-ionizing) for simple geometries
4. Sectoring analysis for radiation dose calculation in more complex geometries
5. Calculation of damage equivalent fluences for Si, Ga As and multi junction solar cells
6. GEANT 4 Monte Carlo analyses for doses and pulse height rates in planar and spherical shields
7. Ion LET and flux spectra and single event upset rates
8. Trapped proton flux anisotropy
9. Atmospheric and ionosphere densities and temperatures
10. Atomic oxygen erosion depths

In SPENVIS magnetic field line tracing is implemented. The generation of world maps and altitude dependence plots of the magnetic fields are also implemented. Models for space craft charging are available. It is a tool to visualize panel plots of measured quantities in combination with geomagnetic and solar indices. Micrometeoroids and space debris models are implemented. On the basis of this model an impact risk analysis module is currently under development. GEANT 4 and SPENVIS can be used complementing each other for certain calculation. For example in the DESIRE project to calculate the radiation levels inside the International Space Station, they used GEANT 4 to simulate the transport of incident particles through the walls of the space station. The flux of incident particles is estimated for a given orbit with SPENVIS package. In calculating the expected dose of radiation falling on CCD under the shield during transit through the earths radiation belt and all along its trajectory and that without shield on the orbit in Chandrayan-I mission during the entire mission period, both GEANT 4 and SPENVIS package were used.

5.1.4 Deep Level Transient Spectroscopy

Deep level transient spectroscopy (DLTS), is introduced by Lang in 1974[7].Deep Level Transient Spectroscopy is an analytical method to determine the abundance, position and the kind of traps centers and deep level defects in semiconductor devices. It gives the information of the energy level and capture rate of the traps [8]. The method is very much suitable for junction devices and metal insulator semiconductor devices. During the past several decades, much experience in DLTS measurements has been accumulated. DLTS offers very high sensitivity.[9] DLTS techniques can also be used for several other studies. For example, the determination of interface density could be carried out by DLTS methods. [10]. A lot of information on this technique is available in literature.

5.1.5 Device characterizers

Various types of device characterizers are mentioned in the literature and text books [11] Electrical Characterization techniques are most important. This includes two point probes, Four point probes, Hall effect probes, Drive-level capacitance profiling (DLCP) etc. Optical characterization are based on photo luminescence, and various spectroscopic techniques. Physico-chemical property studies include electron beam, ion beam and X-ray techniques used in the solid state physics laboratories

5.1.6 ExpEyes

ExpEyes can be used as an important tool for the data acquisition and automated measurement in the laboratory. The tool is so effective that, it could be programmed to suit our requirement of measurement and control. It provides an integrated measurement environment, with programmable CRO, analogue and digital signal clock generator, amplifiers, sensor nodes, etc. built in to single system. The device can be integrated with a PC, tablet and other equipments.[12] ExpEyes is developed by InterUniversity Accelerator Centre (IUAC, Web : www.iuac.res.in), New Delhi, India, under physics with Home-made Equipment and Innovative Experiments (PHOENIX) project[13]. It is suitable for young engineers and scientists. The design is optimized to be simple, flexible, rugged and low cost. Because of low cost, it enables students to per-

form experiments both in laboratories and beyond. Hardware design is open source and royalty-free. The software is released under GNU General Public License.[14]. ExpEyes offers one of the viable methods to interface students and physical world using computer based techniques[15].

Salient features of ExpEyes Junior include [16][17]: Built-in Signal Generator and CRO, USB Powered, 12 bit Analog to Digital Converter, Microsecond timing resolution, Open Source Hardware and Free Software, Uses Python programming language[18][19] and accuratemeasurements. I used ExpEyes in my work for in-situ device characterization from remote location while the device being irradiated.

5.1.7 Development of Data acquisition systems

A data acquisition system for studying the online voltage current characteristics of transistors and other electronic discrete components has been designed for the study the effect of radiation on these devices. The system was originally designed for online study for the remote data acquisition. But later it was found that, ExpEyes could be configured to work from remote desk top and it was used for in-situ study. ExpEyes also has the advantage that it provide 12 bit resolution. However, for part of the offline study, this data acquisition system was made use.

The device may be used to study online/ offline variation in the physical parameters of electronic devices during irradiation or after irradiation.

The system has two units. The *Control Board* and a *Test Board* . They could be interconnected. Control Board measures the values of voltage across a device as well as the current flowing through the device automatically and the data is stored in its memory during the time of radiation falling on the device. It is built around an 8 bit micro controller. The Electronic device under exposure to radiation is connected to the test board. The voltage across the device and the current passing through the device are measured, scaled and sent to the control board. Linear scaling and conversion of current in to voltage is done by means of the instrumentation amplifier in the Test Board. The data in the device could be viewed, one pair at a time, through LCD display provided with the data acquisition system control board. It is possible to navigate through the data table by working the navigation keys provided with the system. Fig 5.3 and 5.4 shows the circuit diagram for the data acquisition sysytem

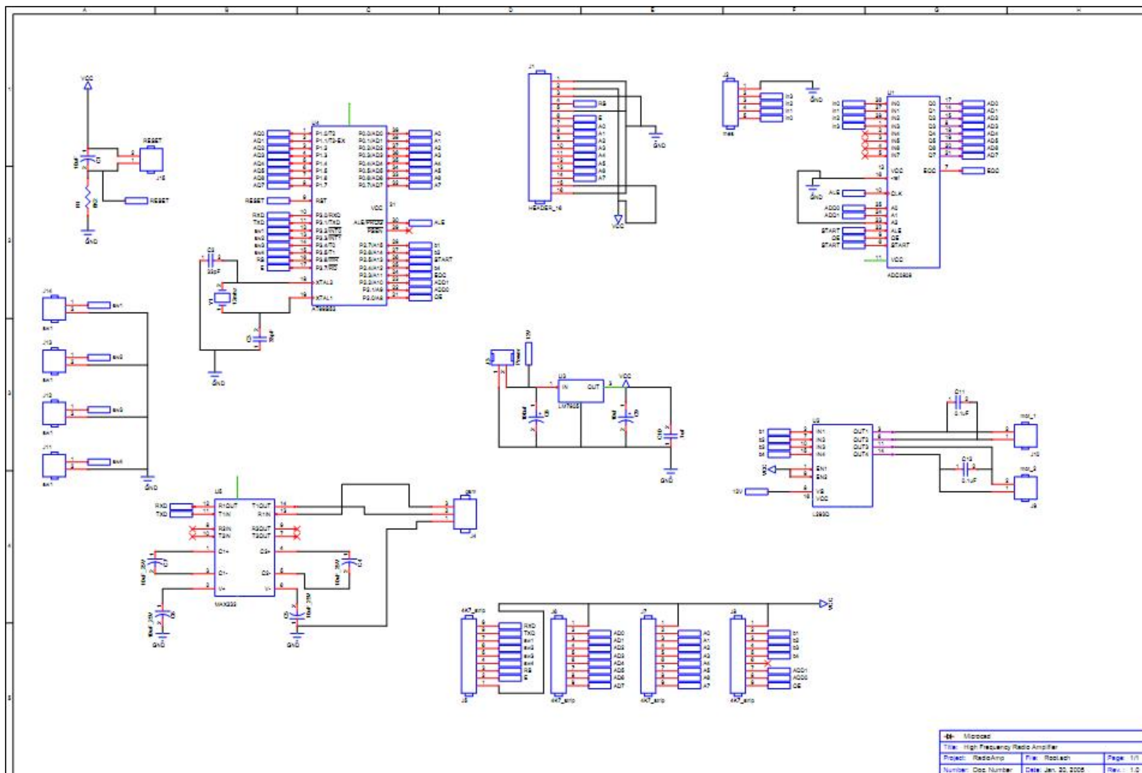

Figure 5.3: Circuit diagram - Data Aquisition System Control Board

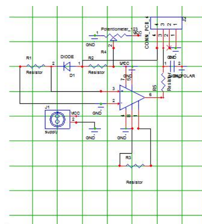

Figure 5.4: Circuit diagram - Data Aquisition System Test Board

Other analysis tools used in this work include development of codes for data analysis. Matlab codes were written for data binning. Again the binned data is fitted with expected Gaussian peaks in the CCD data analysis. The fitted data is used in the calculation of FWHM of the peaks. The codes given below were used for data binning , fitting and FWHM calculation.

```
I-Matlab Code for data binning
Code has been written for data binning 16 bit data
originally recorded  while analyzing CCD. Code for
 reading CSV data (binned data) from a file ,
 accumulate pre-defined data values in bins;
 Find energy/channel  from the known energy value
  of the peaks.  lot Gaussian fitted data,
 find FWHM and other properties of the peak.
clear all;
close all;
clc;
text=[];
textarray=[];
filename = 'n30_e anu1_cfg_295frames.csv';
rowbegin = input('Enter the bigginning line of data to read: ');
ndp = input('Enter No. of data points in the bin: ');
outfile_pathstring ='temp_vs_fwhm';
fid = fopen (filename);
if fid == -1;
    disp( 'File does not exist');
    prompt = input('Enter any key to exit ! ' ,'s');
    status = fclose('all');
    quit force;
else
  finfo = dir(filename);
  fsize = finfo.bytes;
   if fsize > 0
    S=csvread(filename, rowbegin,0);
    [m,n]=size(S);
    [pathstr,name,ext,versn] = fileparts(filename);
    out_file = strcat(outfile_pathstring,'\',name,'binned','.txt');
    f2 = fopen(out_file, 'w');
     for i=1:ndp:(m - ndp)
      fprintf(f2,'%d %d',max(S(i:(i+ndp-1),1)),sum(S(i:(i+ ndp-1),2)));
          fprintf(f2,'\n');
        end
        fclose(f2);
    end
```

```
end
%--------Plotting data
 plotData=load(out_file);
 [m,n]=size(plotData);
tmpData=zeros(m,n);
flag=0;
k=1;
for i=m:-1:1
      if flag==0
        if(plotData(i,2)>0 )
            flag=1;
        end;
    end
    if (flag==1)
        tmpData(k,1:2)=plotData(i,1:2);
        k=k+1;
    end
end
%//------------------------------------
clear plotData;
plotData=tmpData;
out_file = strcat(outfile_pathstring,'\', name, '_plot','.txt');
f4 = fopen(out_file, 'w');
[m,n]=size(plotData);
flag=0;
for i=m:-1:1
    if flag==0
        if(plotData(i,2)>0 )
            flag=1;
        end;
    end
    if (flag==1)
        fprintf(f4,'%d %d',plotData(i,1),plotData(i,2));
        fprintf(f4,'\n');
    end
end
fclose(f4);
fclose('all');
%------------------------------------------
II-Matlab Code for Gaussian fitting and FWHM Calculation.
```

```
code for reading csv data from a file , accumulate

pre-defined data values
in bins;
plot guasian fitted bin data
clear all;
close all;
clc;
%par_name =   input('Enter Parameter name: ','s');
format long e;
% fp=fopen('D:\TIFR\PRERAD\result.txt','a');
rowbegin = 500;
rowbegin_plot = rowbegin;
%rowend   = 30000;

rowend =input('Enter the right trim line of data to read(>0): ');

 rowend is hard coded for convenience
data_range = [rowbegin,0,rowend,1];
[filename1,filepath1]=uigetfile({'*.*','All Files'},'sel data File1');
  cd (filepath1);
  filename = strcat(filepath1, filename1);
  fid = fopen (filename);
     if fid == -1;
        disp( 'File does not exist');
        prompt = input('Enter any key to exit ! ' ,'s');
        status = fclose('all');
        quit force;
    end
   a=dlmread(filename, ',', rowbegin, 0, data_range);
   %s = csvread(filename, rowbegin,0,data_range);
   %a = csvread(filename, rowbegin,0,data_range);
   fclose(fid);
    %-------------------------------------
    a=load(filename);
    figure('position',get(0,'ScreenSize'))
   plot (a(rowbegin:rowend,1),a(rowbegin:rowend,2));
    m=[];
    n=[];
    p=[];
```

```
    q=[];
    [m,n] = ginput(2);
   g = [m,n];
   set(gcf,'Visible', 'off');
 rowbegin = input('Enter the begin line of data to read(>0):');
   plot (a(rowbegin:rowend,1),a(rowbegin:rowend,2));
   [p,q] = ginput(4);
   h = [p,q];
   set(gcf,'Visible', 'off');
   m = cat(1,g, h);
   m= m(:,1);
   m
   i=1;
   for i =1:3
        k = (floor(m(2*i))-floor(m(2*i-1)));
        x  = zeros(k,1);
        y = zeros(k,1);
        x = a(floor(m(2*i-1)):floor(m(2*i)),1);
        y = a(floor(m(2*i-1)):floor(m(2*i)),2);
        b  = fit(x,y,'gauss1');
        ymax(i)= b.a1;
        mu(i) = b.b1;
        sigma(i) = b.c1/1.414;
     end
   %eV is the energy of the k-alpha and k-beta lines
   ev(1)= 0;
   ev(2)= 5898;
   ev(3)= 6490;
   p= polyfit(mu,ev,1);
   evperch =(ev(3)-ev(2))/(mu(3)-mu(2));
  % evperch = p(1);
   fwhm = sigma*2.35.*evperch;
   evperch , fwhm
   figure (1);
   rowbegin = rowbegin_plot;
  % rowend =4090;
   plot (a(rowbegin:rowend,1),a(rowbegin:rowend,2));
   currentDirectory = pwd;
   [upperPath,deepestFolder]=fileparts(currentDirectory);
 title(sprintf('X-ray (5898 eV and 6490eV peaks ): %s',deepestFolder));
```

```
  xlabel('Channel Number');
  ylabel('Counts');
    for i =1:3
    str = strcat(num2str(fwhm(i)),' eV');
    text(mu(i),(ymax(i)/2.0),str);
  end
  saveas (gcf, 'CCD_TIFR_Pr_rad_15May','jpg');
  saveas (gcf, 'CCD_TIFR_Pr_rad_15May','eps');
   close all;
par_value = input('Enter value of  parameter in each spectrum :','s');
   par_value = str2double(par_value);$
   fprintf(fp,'\n\n');
   fprintf(fp,'%s\t''%2.2d\t',par_name,par_value);
   fprintf(fp,'%3.3f\t''%4.4f\t''%4.4f\t''%4.4f\t',evperch,
   fwhm(1),fwhm(2),fwhm(3));
   fprintf(fp,'\n\n');
   fclose (fp);
%   user_entry = input('prompt', 's');
 close all;
```

Bibliography

[1] J.P Biersack and LG haggmark A monte Carlo Computer Program for the transport of energetic ions in amorphous targets, Nucl. Instr. Meth. PP. (1980)

[2] J F Ziegler, J P Beirsack et al; The stopping and range of ions in matte; Pergamon press, NewYork (1985)

[3] R. Smith. Atomic and ion collision in solids and at surfaces: Thery Simulation and application. Cambridege University Press; Cambridge.

[4] M T Robinson. Channelling of enenrgetic atom in Crystal lattices. Appl. Physics letters., 2(4): 30,1963

[5] R S Averback et al; Displacement damamge in irradiated metals and semiconductors; Solid state Physics Volume 51 pp 280-405. Academic Press ; New York.

[6] P. Vajda. Anisotropy of electron radiation damage in metal crystal. Rev. Modern Physics;(1977)

[7] D. V. Lang; Deep-level transient spectroscopy: A new method to characterize traps in semiconductors; Appl. Phys. 45, 3014 1974

[8] T. J. Tredwell and C. R. Viswanathan, Solid-State Electron. 23, 1171; (1980). Dong Wang, 1 Shuta Kojima, 1 Keita Sakamoto, 1 Keisuke Yamamoto, 1 and Hiroshi Nakashima2;An accurate characterization of interface-state by DLTS for Ge metal-insulator-semiconductor capacitors with SiO2/GeO2 bilayer passivation; Jn. Appl. Phys 112, 083707 (2012)

[9] R Williams, Journal of Applied Physics; 37, 3411 (1966)

[10] CT. Sah; L Forbes; LL Rosier; AF Tasch. Journal of Solid State Electron,13,759 (1970)

[11] LD Yau and CT Sah, Phys. Status Solidi A 6, 561(1971)

[12] Ref. Dieter K Schroder; Semiconductor Material and Device Characterization,3rd Edition.

[13] A. B. Raju, Anupama Itagi, Sachin Angadi, V. Sushma and Ashok Shettar; A Low Cost Open Source Hardware Tool for Integrated Learning Experience in Laboratories; Journal of Engineering Education Transformations, Special Issue: Jan. 2015.

[14] Python Melvin Chelli, Rakesh Hirur, Shashikant Attimarad, Harish Dabade and A.B. Raju ; Closed loop Control of A DC Motor using ExpEyes . SciPy 2004 Conference - Python for Scientific Computing; http://www.scipy.org/wikis/scipy04.

[15] Roger L. Traylor, Donald Heer, and Terri S. Fiez, Using an Integrated Platform for LearningTM to Reinvent Engineering Education, IEEE Transactions on Education, Vol. 46, No. 4, pp. 409-418, Nov. 2003.

[16] [Online]. ExpEyes Junior Users Manual, Available: http://ExpEyes.in/ [Accessed: Nov. 5, 2014].

[17] [Online]. ExpEyes Junior ExpEyes-Junior Programmers Manual, Available: http://expeyes.in/ [Accessed: Nov. 5, 2014].

[18] Shakil Seerji, Enaiyat Ghani Ovy, Tasnim Alam, Ahsan Zamee, Abdur Rahman Al Emon, A flexible closed loop PMDC Motor Speed Control System for Precise Positioning, International Journal of Robotics and Automation, vol. 2, Issue 3, 2011

[19] Swaroop CH, A Byte Of Python .(Revised Edition 2005). eBook. Amazone.in

[20] Ajith Kumar B.P., Python For Education. Free ebook. IUAC, New Delhi www.expeyes.in

Chapter 6

Experimental Observation and Analysis

6.1 Study of the Effect of Space Radiation on Electronic Devices

6.1.1 Introduction

The interest of this study is limited to electronic devices that may undergo exposure to space radiation in the space vehicle. The experimental method involves detailed study of the characteristics of the device before irradiation and determines the device parameters. Then, the device was exposed to different types of radiation of known energies. The experiment was systematically repeated exposing the devices to various doses. The change in characteristics of the devices studied. The possible reason for the change of characteristics of the devices is also analyzed. A brief review of experimental studies done earlier has been examined [1]-[8].

The study was carried out in three phases, (1) Offline study of simple components diodes, zener diodes and transistors, (2) Online study of simple components and (3) Off-line study of an application device (SCD to be used for Chandrayan II), as detailed below.

1. Phase 1 Offline Study

   Offline studies were carried out for diodes, zener diodes and transistors. A set of 5 identical samples were selected for each device for each studies using photon and electron beam. The characteristics of the devices were studied before the irradiation. The samples were then, subjected to irradiation by photons of different energies at a constant dose and recorded the effect

of energy of radiation on the device characteristics. A few devices were, then, subjected to photon irradiation to different doses at constant energy to study the effect of dose on the characteristics of the device. Since the Bremsstrahlung from medical linear accelerator is used as a source of photon, energy mentioned in the discussion is the maximum energy in the Bremsstrahlung spectra

2. Phase 2 Online (in-situ) Study

   Case (1). Proper experimental setup is created for in-situ study. The characteristics of various discrete devices before exposure to radiation has been studied.

   Case (2). The characteristics of various discrete devices has been studied during irradiation.

   The experiments for phase I and Phase II were performed at a hospital radiation facility using medical linear accelerator -Seimens Primus Plus LINAC- providing 6 and 15 MeV photon. The energy, total dose and dose rate of the gamma radiation beam could be fixed from the control room. The nature of the beam spread was adjusted by automated system. The beam was made narrow and uniform with minimum spread. Dose linearity error was kept less than ± 1 [9].

3. Phase 3 Ground Simulation Test (on SCD Proposed to be Used in Chandrayan II Mission)

   The ground emulation test was conducted for the active SCD, proposed to be used in the space exploration program of Chandrayan II mission, to determine the radiation damages caused to SCDs when used in space vehicles. Annealing study of the device was also conducted after irradiation.

6.1.2 Phase - 1 Effect of radiation on discrete devices- Offline Study

The experiment was performed by using the data acquisition set up described in chapter 5. The V-I characteristics were studied before and after irradiation. The data acquisition system, designed, generates voltage which could be incremented in steps, across the device to be tested. The device was connected to the test board. The current passing through the device was measured in terms of voltage across the *precision low resistance*, connected in series with the device. The control board could fetch the instantaneous values of the voltage and current from the test board and store in its memory. The LCD display, that

form the part of the control board was used to read the data. Three different components namely, Junction diode, Zener diode and Junction transistor were used for the study. In the online study, this set up was replaced by *ExpEyes* by configuring it for remote data acquisition.

Irradiation of the devices with X-rays and electron beam were done separately. In each case, the data was taken under different doses and under different energy of the radiation. High energy X-rays from LINAC at hospital radiation facility was used for the study.

6.2 Irradiation Effect on Junction Diodes

Bremsstrahlung X-ray irradiation effect on Junction diode

- Characteristics Before Irradiation with X-rays

The p-n junction used for the study was 1N 4001. Five samples were studied. The V-I characteristics of all the five samples were plotted under forward bias and found to be having identical V-I characteristics as given by diode equation (6.1), which is shown in figure.6.1 and assured that all those selected devices are having exactly identical characteristics.

$$I = I_0.exp(eV/nkT - 1); \tag{6.1}$$

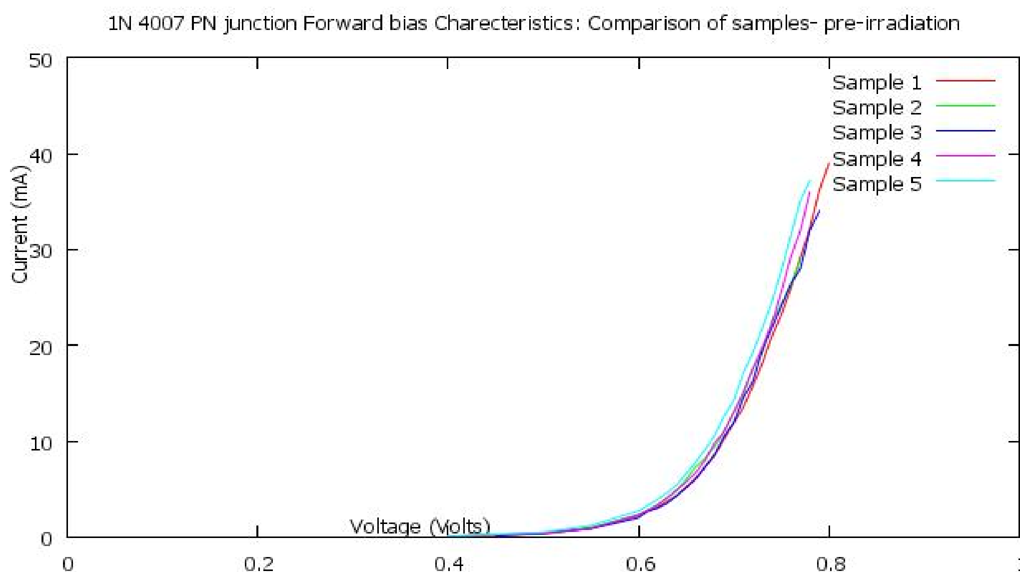

Figure 6.1: Junction diodes- Pre-irradiation characteristics of the samples

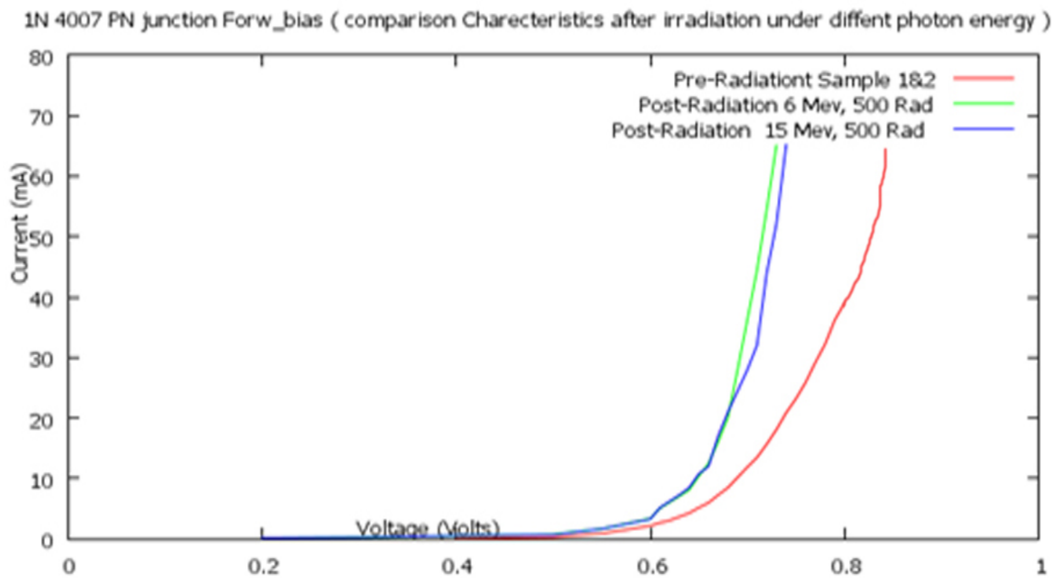

Figure 6.2: Characteristics of p-n junction after irradiation by photons of different energy at a constat dose level

Here, n is the ideality factor. The ideality factor and leakage current were comparable for all the devices.

- Characteristics After Irradiation with X-rays. Effect of photon energy of radiation.

Out of the five samples above, sample 1 was given X-ray dose of 500 rad at 6 MeV energy and sample 2 was exposed to 500 rad of 15 MeV X-ray, to study the effect of energy of radiation. The total dose, in both cases, was 500 rad. Post irradiation characteristics of these samples were studied after the exposure and plotted,in figure (6.2), along with pre-irradiation data . V-I characteristics was also plotted in logarithmic scale of current as shown in figure (6.3). From the figures it could be seen that, there is a marked decrease in the forward resistance of the diodes after irradiation and it was found to be independent of energy of the incident radiation over the given range.

- Characteristics After Irradiation with X-rays. Effect of photon dose Dose.

In order to see the effect of exposed dose, the experiment was repeated for three doses 1000, 2000 and 3000 rad at 6 MeV with rest of the samples and plotted in figure (6.4).

It is interesting to note that, there was a shift in the knee voltage on varying the doses from 1000 rad to 2000 rad. System shows identical characteristics 1000

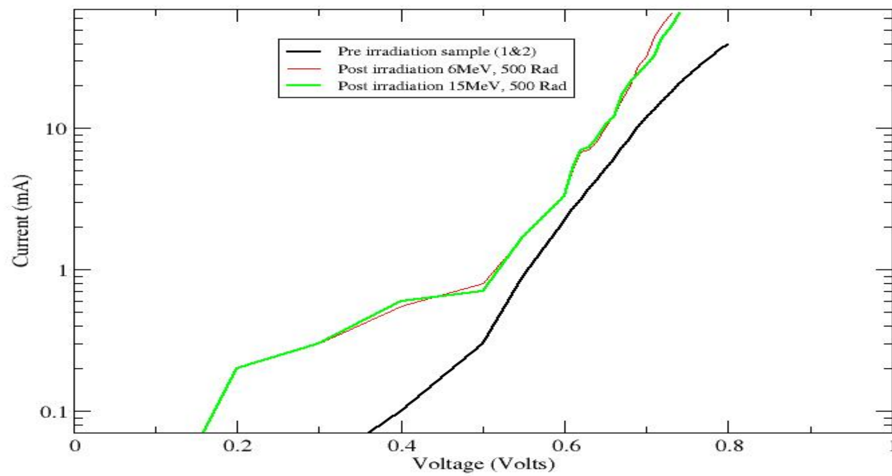

Figure 6.3: p-n Junction (1N 4001)-Comparison of characteristics after irradiation with different photon energy (current in the log scale)

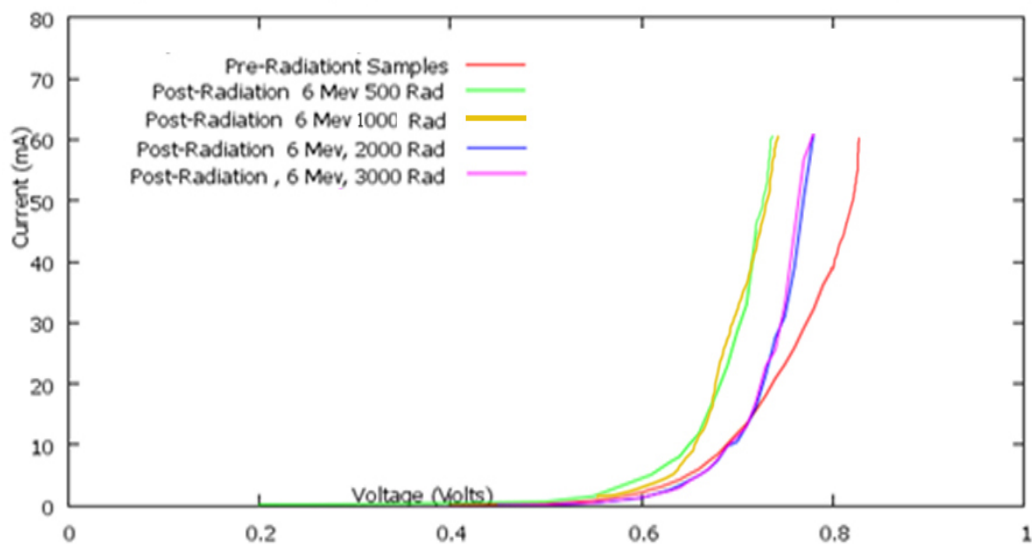

Figure 6.4: Characteristics of p-n junction after irradiation by 6 MeV photons to different doses

and shifted identical characteristics for a dose for 2000 rad and 3000 rad. At 2000 rad and above, the knee voltage shift towards the pre-irradiated position while maintaining sharp switching nature of post irradiated dose of 1000 rad.

The diode turns on at a lower forward bias voltage after irradiation of 1000 rad, but goes back to preirradiated state on further increase in dose. This nature may be attributed to the radiation annealing effect of the device. This result indicated that, the enhancement of energy did not increase the energy deposition in the device whereas the enhancement of dose has increased the energy deposition.

The dose dependence of the radiation data was plotted along with pre-irradiation data in logarithmic scale in figure (6.5) to extract the leakage current and to understand the nature of variation of band gap. The pre-irradiation plot was almost linear in the logarithmic scale. There are two regions in the plots. The upper region, which determine the slope and ideality factor of the diodes are identical at these doses. The leakage current was determined from the y intercept of the graph obtained by extrapolating the graph on to the y-axis. The pre-irradiation characteristics showed very low leakage current (I_0). Taking logarithm of the equation of diode (equation 1) on both sides, we get,

$$logI = logI_0 + (e/nkT)V;$$

The factor, (e/nkT) is the slope of the above curve and log I_0 is the intercept. It could be seen that, after irradiation, the leakage current I_0 increase. The value of log I_0 could be determined by extrapolating the graph. The slope the graph was also measured to determine the change in the ideality factor of the diode. The slope of this region is more, compared to, the pre-irradiated characteristics, suggesting, a variation of the ideality factor of the diode. However, the leakage current due to diode irradiated by 1000 rad, is more, compared to that irradiated by 2000 rad and 3000 rad. This fact, indicated that, radiation annealing has taken place at higher doses.

After irradiation, the current is found to build up from 0.2 volt or less whereas the current start building up at 0.4 volts before irradiation. This could be due to the formation of trap centers with trap energy, that, falls in between conduction band and valance band. The trap assisted conduction starts in the irradiated diode at a lower forward bias voltage. The post irradiation plots are the same for 6 MeV and 15 MeV at a dose of 500 rad. The result could be summarized as in the table 6.1.

Table 6.1: p-n Junction - Photon irradiation data

Photon irradiation of p-n junction	Log I_0 mA	Leakage current I_0	Slope	Change in slope after irradiation
Before irradiation	0.006	1.01 mA	0.064	——
After irradiation 6 MeV photon	0.12	1.32 mA	0.072	12.5%
After irradiation 15 MeV photon	0.12	1.32 mA	0.072	12.5%

It is found that, leakage current is increased after irradiation. However, there was no change of leakage current with change in photon energy, in the energy range used. Similarly, the slope, which is a measure of ideality factor showed 12.5 % change after irradiation. The ideality factor also did not show change with energy of the incident photons in the energy range used.

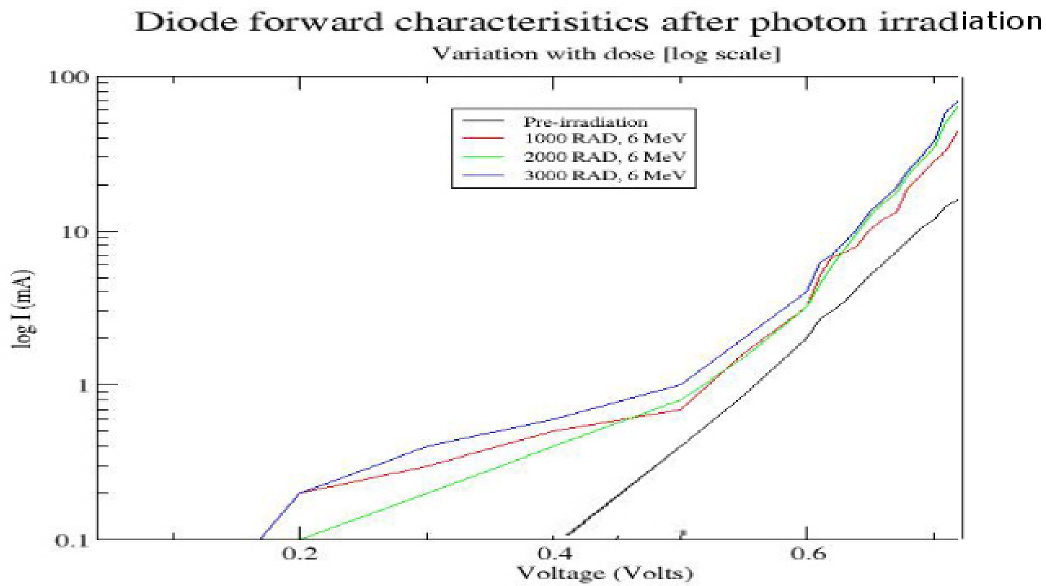

Figure 6.5: Diode forward bias characteristics after 6 MeV photon irradiation. Study of the effect of variation of dose

6.2.1 Electron irradiation effect

Study of the effect of variation of the energy of electron radiation

Similar studies were carried out for electron irradiation of p-n junction diodes. Experiment was conducted to study the effect of variation of electron dose. The electron beam was obtained from the same Linac used for the photon

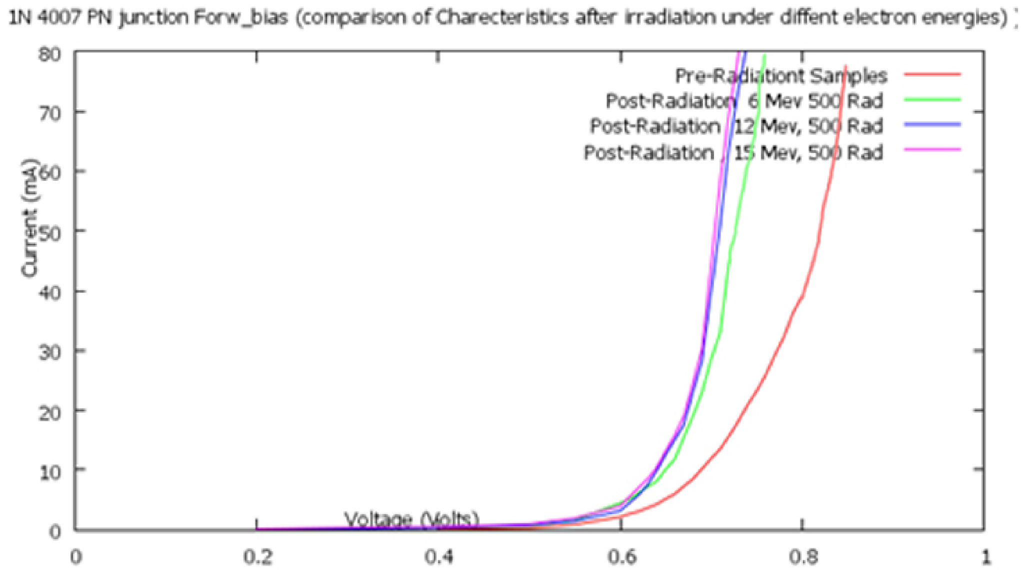

Figure 6.6: Characteristics of pn junction before and after irradiation under different electron energy

irradiation. Six samples of IN4001 diodes were irradiated with electrons beams of energies 6, 12 and 15 MeV and doses of 500 rad, 1500 rad and 3000 rad.. Sample 1, 2 and 3 were irradiated with electrons of energy 6 MeV, 12 MeV and 15 MeV respectively, to the same dose level of 500 rad each and sample 4 , 5 and 6 are used for studying the dose effect. After irradiation the device characteristics were studied. The observation are plotted in figure (6.6) for the variation of energy. The logarithmic plot of the variation of characteristics with energy is also plotted in figure (6.7) to deduce the ideality factor and leakage current. The observation for the variation of dose is plotted in figure 6.8. The logarithmic plot of the variation of characteristics with dose is also plotted in figure 6.9.

Here also, it is seen that,with variation of energy, there is no change in characteristics where as the change in characteristics is affected by the variation of dose. The electron irradiation has the similar nature of characteristics to that of the photon, both for energy variation and dose variation. it can be assumed that, the energy deposition mechanism is similar in both electron and photons.

The graph in the figures 6.7 shows that, as in the case of photon irradiation, there is an increased leakage current after electron irradiation. The leakage current due to electron irradiation has some energy dependence. However, the leakage current due to photons has little or no energy dependence in the energy range chosen. The result is tabulated in table 6.2.

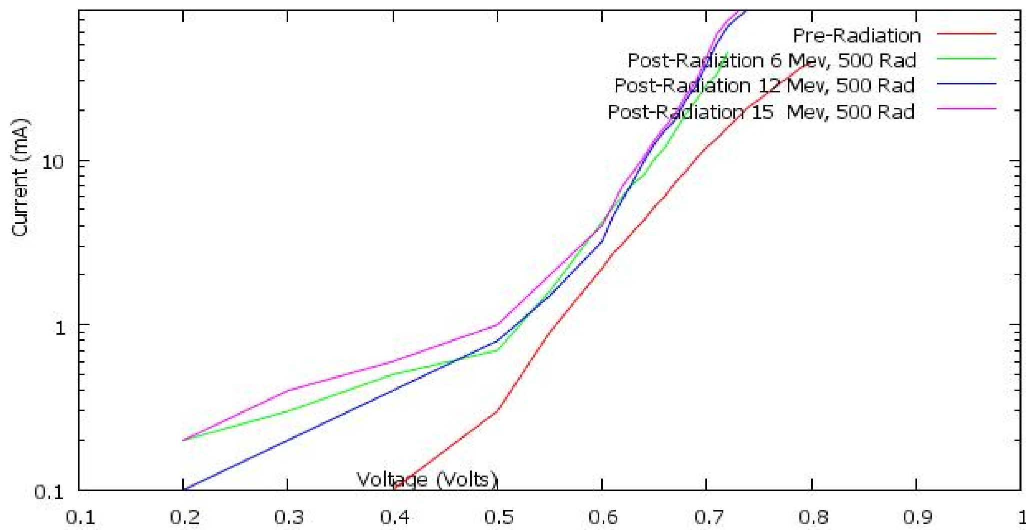

Figure 6.7: V-I characteristics of PN junction after irradiation with electrons of different energy (with current in log scale)

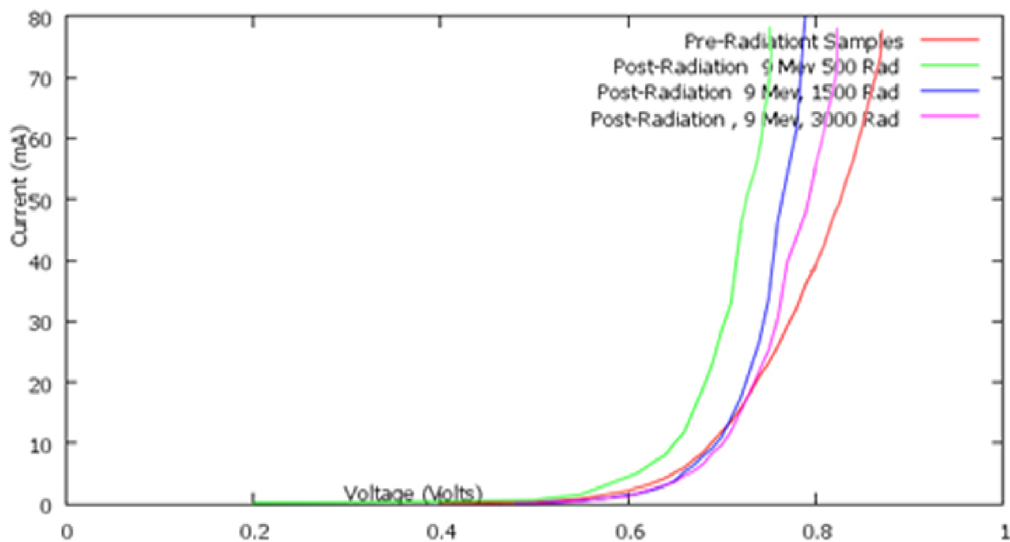

Figure 6.8: Characteristics of pn junction before and after irradiation under different electron doses

Table 6.2: PN Junction-Electron Irradiation data

Electron irradiation of p-n junction	Log I_0 mA	Leakage current I_0	Slope	Change in slope after irradiation
Before irradiation	0.005	1.01 mA	0.069	—
After irradiation 6 MeV electron	0.12	1.32 mA	0.078	13%
After irradiation 15 MeV electron	0.12	1.32 mA	0.078	13%

As in the case of photon irradiation, there were changes in the leakage current and ideality factor after irradiation of the p-n junction with electrons of comparable energy. The results are comparable in the given energy range.

Study of the effect of variation of the dose of electron radiation

Preirradiation characteristics were determined. The devices were irradiated with electron beam at doses shown above and plotted as shown in figure(6.8). All the plots suggested that, dose variation has much effect on the device characteristics. The effect is more at a lower dose in the dose range used. As the dose was increased, there was an increased annealing effect on the radiation effect on the device. At the lower dose, the device knee voltage is lower than that of preirradiated device. But, as the dose was increased, the knee voltage becomes comparable to that of pre-irradiated device. This observation indicate that, electron irradiation effect is almost identical to photon irradiation effect. Electron damage is also subjected to annealing at higher doses, as that observed in the case of, photon dose variation effect.

The exposure of p-n junction to X-rays can cause ionization damage mainly due to excess charge trapped near their $Si-SiO_2$ interface region. This phenomenon will cause the formation of an inversion region in the p side of the junction. The inversion region on the p side will have the minority charges. The accumulation of minority charges near the junction in the p side will effectively provide a screening effect on the junction potential. This will result in the reduction of junction potential which may be the cause of observed reduction in the knee voltage after irradiation of the p-n junction seen in figure . However, the characteristics at higher doses suggest that, radiation induced annealing may be due to the generation of more trap centers causing increased recovery of the diode characteristic from the changes caused by radiation at low doses.

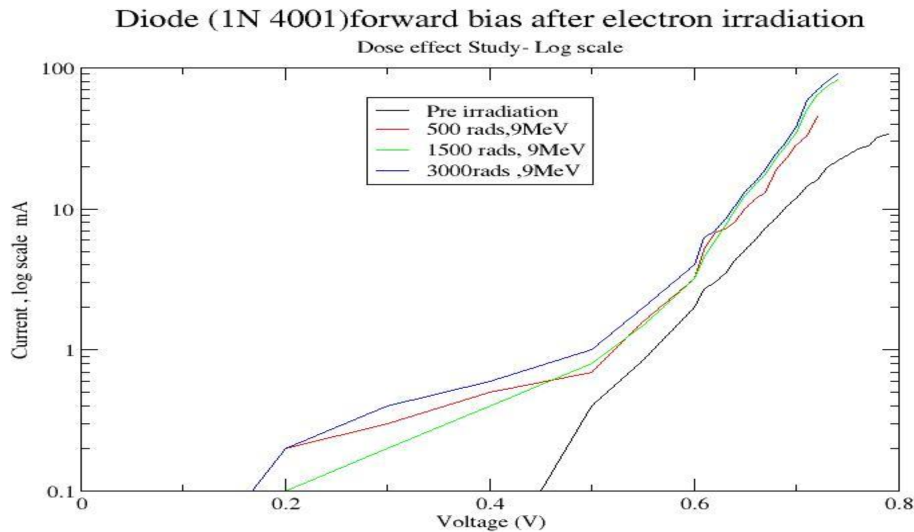

Figure 6.9: V-I characteristics of p-n junction after irradiation with electrons of different energy (with current in log scale)

6.3 Effect of Radiation on Zener Diode

Similar studies of radiation effect due to photon and electron were carried out on zener diodes. 5 zener diodes each of the same series and same characteristics were irradiated with photons and electron separately. A comparison of characteristics of the device before and after exposure to photon radiation and electron radiation at different energies and exposure to different dose levels were made. Since reverse characteristics is more important in applications effect of radiation on zener diode characteristics are also studied.

6.3.1 Zener diode - Effect of radiation under forward bias

- Zener diode-Forward Characteristics After Photon Irradiation (variation with photon energy)

5 identical samples of the device were subjected to photon irradiation. Sample 1 and 2 were exposed to photon energies 6 MeV and 15 MeV respectively and the characteristics after irradiation were plotted along with that before irradiation as shown in figure (6.10) There is a considerable deviation in characteristics before and after exposure. But,there is no noticeable change in characteristics for the variation of energy (even for significant variation in energy). The value of knee voltage of the diode is found to be decreased after irradiation. This change

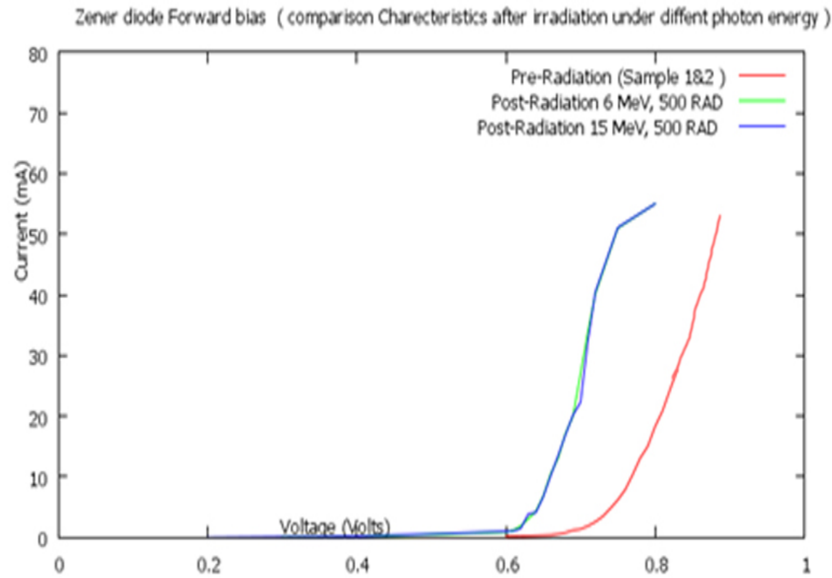

Figure 6.10: Zener diode - Forward characteristics after irradiation with photons of different energies

in the knee voltage is also found to be independent of variation of energy of the photon used for irradiation. The forward resistance is also found to be decreased after irradiation.

- Zener diode - Forward Characteristics After Photon Irradiation (variation with photon dose)

In order to study the effect of dose, samples 3-5 were, then, exposed to photon radiation. Sample 3 was exposed to 6 MeV photons at 1000 rad. Samples 4 and 5 were exposed to photons of the same energy to a dose of 2000 rad and 3000 rad respectively. After exposure, the device V-I characteristics were plotted as shown in figure (6.11) . But, in this case, it was further observed that,at low doses, the forward resistance decreases where as the forward resistance increases at high doses. The shift in the knee voltage during forward bias of the zener diode after irradiation could be understood similar to the same effect observed in the case of p-n junction. This indicates that, the device has achieved saturation effect after certain dose level. Further dose on the device did not change the device characteristics. The device got radiation hardened. This observation suggests an easy method for the radiation hardening of the device by radiation itself at the time of production.

- Zener diode - Forward Bias Characteristics After Electron Irradiation(variation with electron energy)

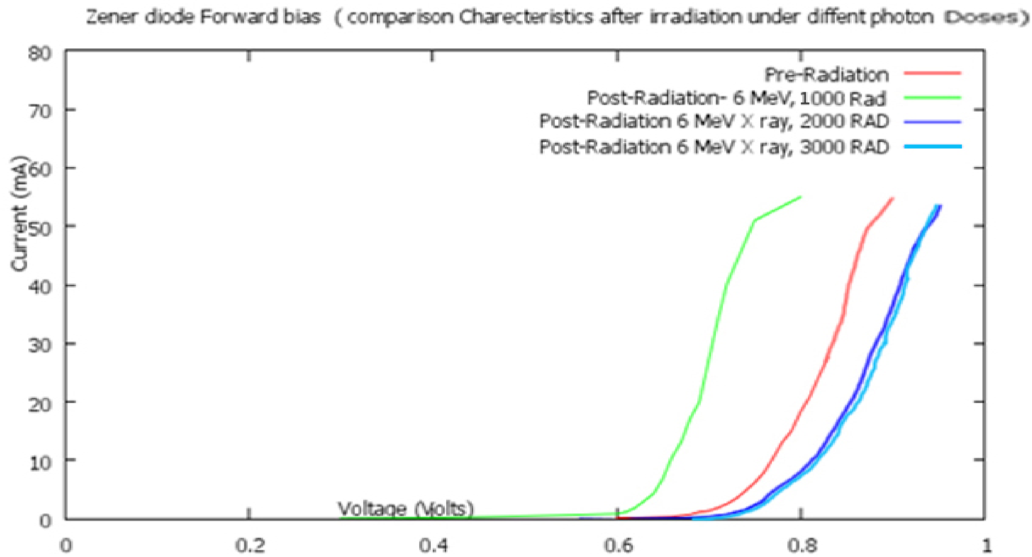

Figure 6.11: Zener diode - Forward characteristics after irradiation with photons at different doses

Similar measurements were carried out for electron exposure of zener diode also. Three Samples were exposed to electron beam energy 6 MeV,12 MeV, 15 MeV respectively. The observation are shown in figure (6.14) and respectively in figure (6.15) for three samples for varying dose 1000, 2000 and 3000 at 6 MeV. The above two graphs were drawn in log scale in figure (6.12) and (6.13) for easy analysis.

There is a change in characteristics before and after irradiation. But, there is no noticeable change in the characteristics observed among the devices exposed with different energies. It was found that, the knee voltage of pre-irradiated diode was about 0.7 Volts. After irradiation with photons at dose of 1000 rad, the knee voltage decreased to 0.6 Volts. It was also noticed that, the effect due to radiation was identical at a dose of 2000 rad and 3000 rad and the knee voltage returns to 0.7 volts at these doses. However, there is a change in the slope observed at higher electron dose. This is an indication of slight shift in the energy gap after irradiation. formation of intermediate energy state due to rare traps in the band gap region may affect the effective energy gap.

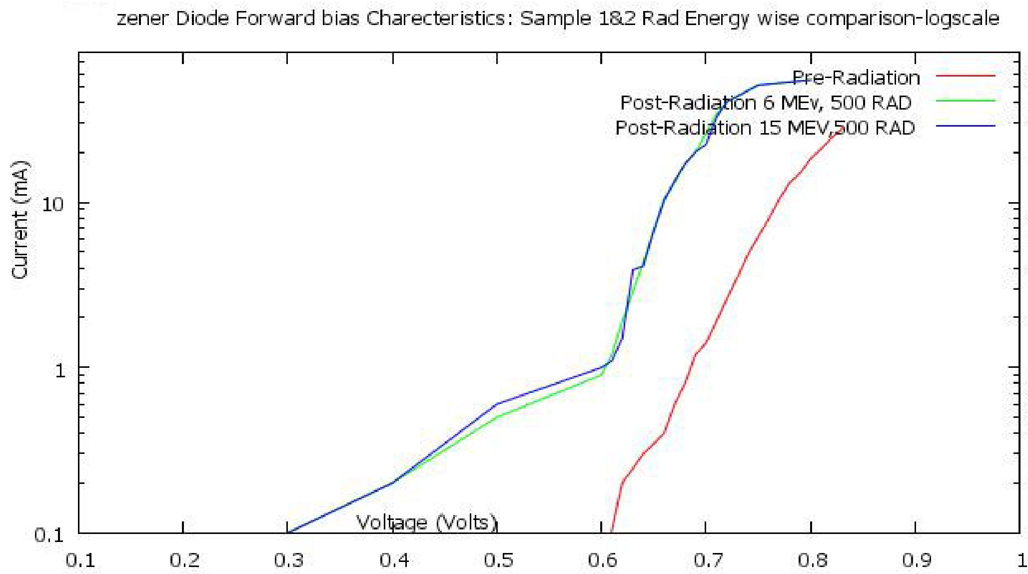

Figure 6.12: Zener diode - Forward characteristics after irradiation with photons at different energies - in logarithmic scale

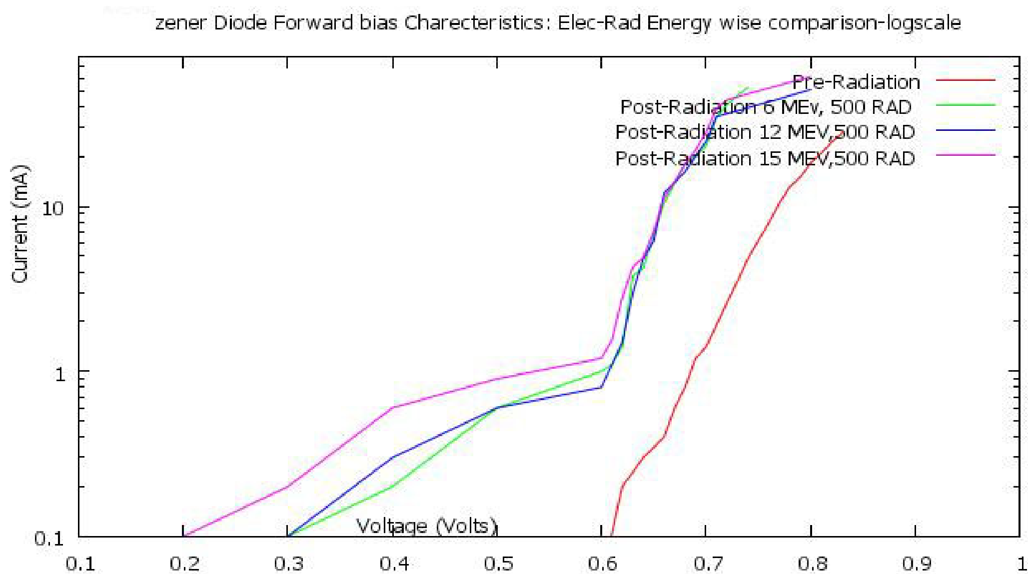

Figure 6.13: Zener diode - Forward characteristics after irradiation with electrons at different energies - in logarithmic scale

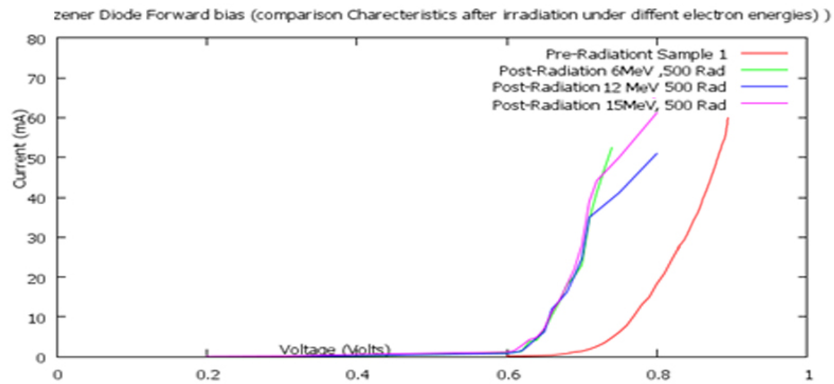

Figure 6.14: Zener diode - Forward characteristics after irradiation with electron of different energies

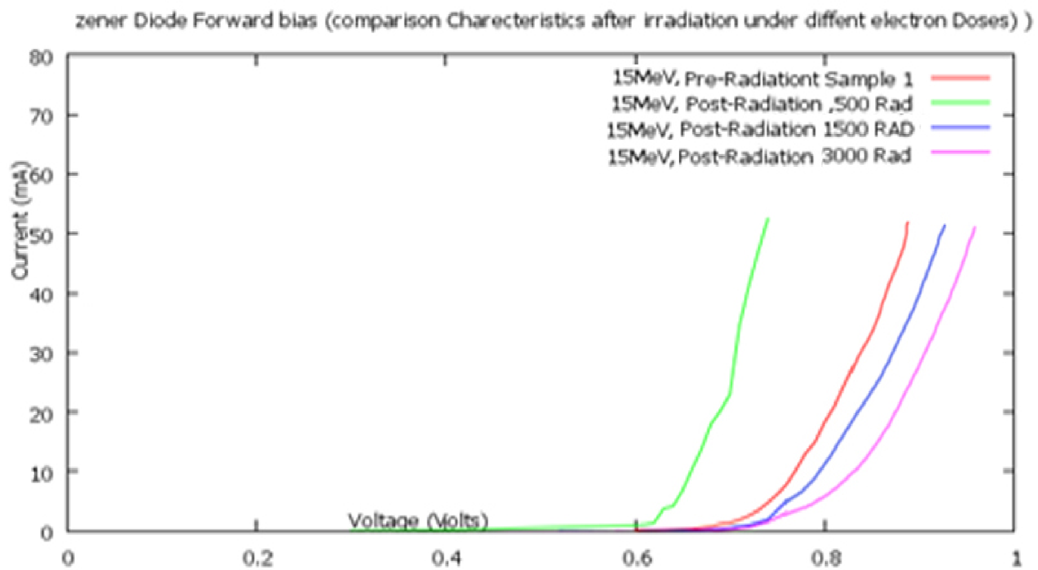

Figure 6.15: Zener diode - Forward characteristics after irradiation with electron at different doses

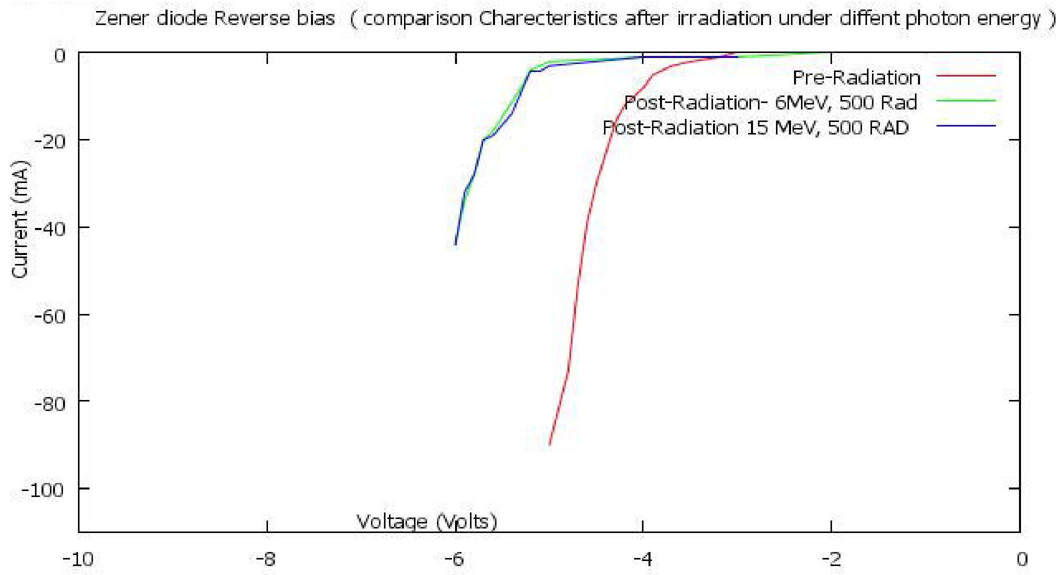

Figure 6.16: Zener diode - Reverse characteristics before and after irradiation with photons at different energies

Table 6.3: Photon irradiation-zener diode

Photon irradiation of zener diode	Log I_0 mA	Leakage current I_0	Slope	Change in slope after irradiation
Before irradiation	0.0	1.0 mA	0.11	——
After irradiation 6 MeV photon	0.02	1.04 mA	0.18	60%
After irradiation 15 MeV photon	0.02	1.04 mA	0.18	60%

Table 6.4: Electron irradiation-zener diode

Photon irradiation of zener diode	Log I_0 mA	Leakage current I_0	Slope	Change in slope after irradiation
Before irradiation	0.0	1.0 mA	0.11	——
After irradiation 6 MeV photon	0.005	1.01 mA	0.18	60%
After irradiation 12 MeV photon	0.01	1.02 mA	0.18	60%
After irradiation 15 MeV photon	0.02	1.04 mA	0.18	60%

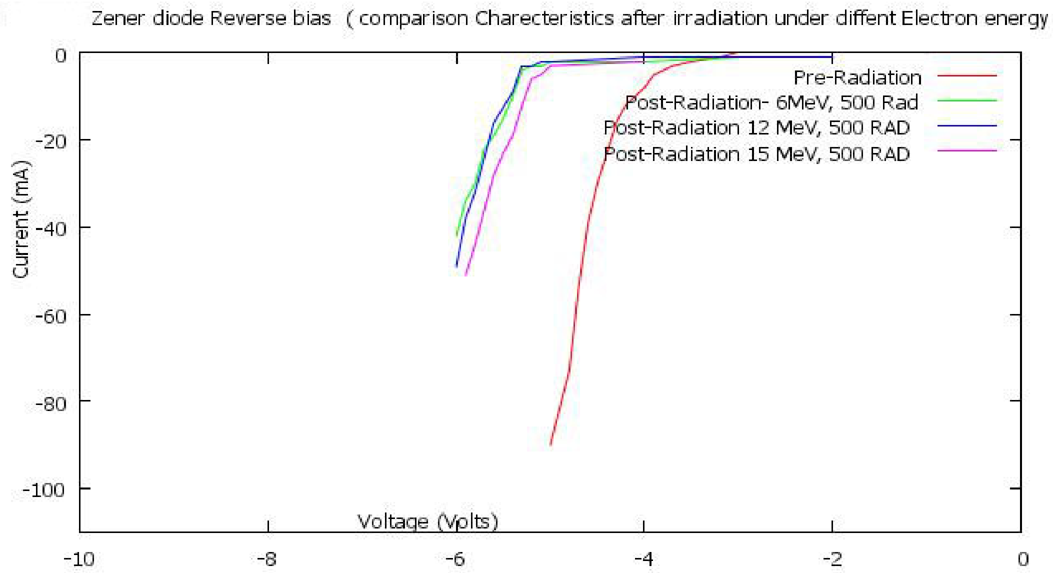

Figure 6.17: Zener diode - Reverse characteristics after irradiation with electrons at different energies along with that before irradiation

Irradiation effect on the reverse characteristics of Zener diode - Photon irradiation

- Zener diode - Reverse Bias Characteristics After photon Irradiation(variation with photon energy)

A set of 5 samples of zener diodes with identical Voltage- Current characteristics were used in the study. Pre- irradiation characteristics was first determined. Sample 1 was irradiated with 6 MeV photon and sample 2 was irradiated with 15 MeV photon. Both samples were irradiated to the same dose of 500 rads. The break down voltage of zener diode was found to increase after irradiation . However, under a given dose, there was no variation in the reverse characteristics, with change in energy of the electron beam. The effect is similar to that of the forward biasing.

- Zener Diode Reverse Bias - Effect of Photon Dose.

The other set of zener diodes irradiated with photons of energy 6 MeV . Sample 3,4,and 5 are irradiated to doses of 500 rad, 2000 rad and 3000 rad respectively. V-I characteristics plotted after irradiation is shown in figure 6.19

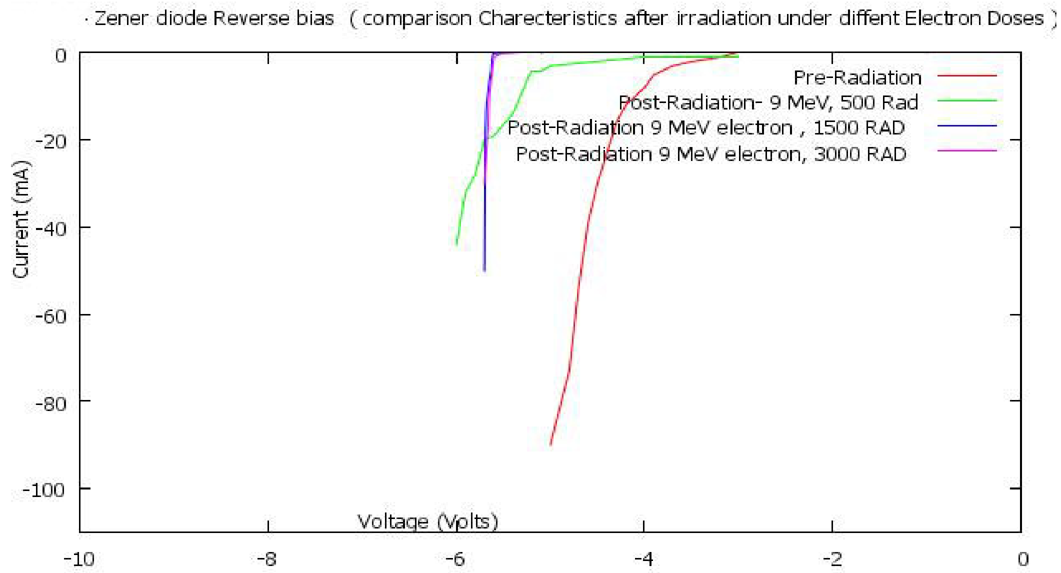

Figure 6.18: Zener diode - electron dose effect study on reverse characteristics. Compared with that of Pre-irradiation plot

6.3.2 Zener diode under reverse bias - Electron effect study

- Zener diode - Reverse Bias Characteristics- Variation with Electron Irradiation(variation with electron energy)

From the above st of samples, sample 3 - 5 were used for the variation of reverse characteristics of zener diode when irradiated with electrons of different energy. Three samples were irradiated with 6 MeV, 12 MeV and 15 Mev electrons at 500 rad each. The observations are plotted in figure 6.17. The observations are very similar to the energy variation effect of photon irradiation on the reverse characteristics of zener diode.

- Zener Diode Reverse Bias - Comparison of Characteristics- effect of electron dose.

A set of 6 identical zener diodes were used in the study. 3 samples were irradiated with electrons of energy 9 MeV . The sample 1 was irradiated to a dose of 500 rad, sample 2 to 1500 rad and sample 3 to 3000 rad. The observation is plotted in figure 6.18.

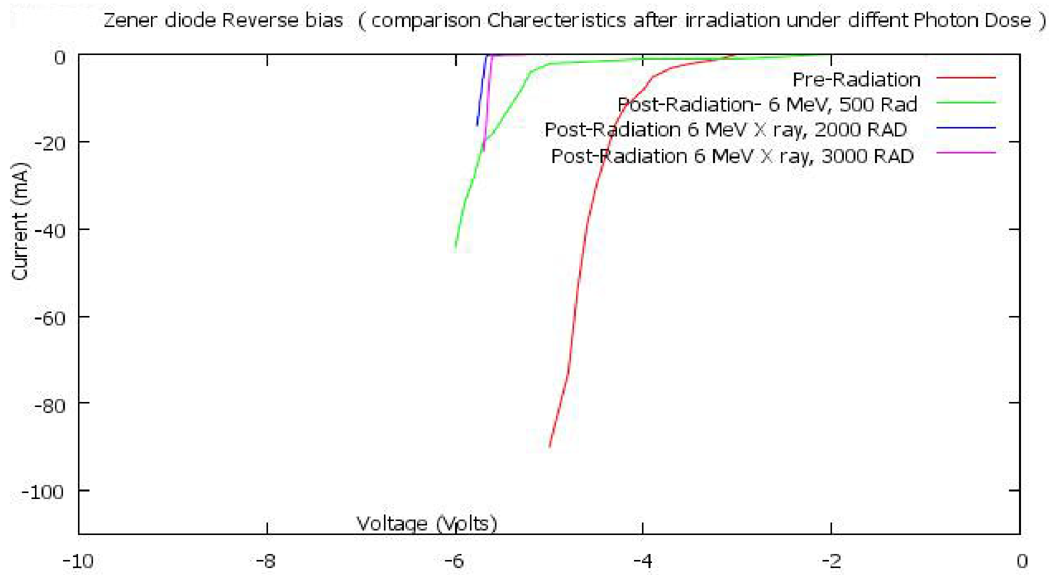

Figure 6.19: Zener diode - Photon dose effect study on reverse characteristics. Compared with that of Pre-irradiation plot

Notable features in reverse characteristics

When zener diode is irradiated with photons, very interesting features have been observed in the reverse characteristics. The breakdown voltage is found to increase with dose and finally reach a saturation value at a dose above 1500 rad. Further, reverse breakdown become more rapid, steep and ideal at these doses. Similar features were observed for irradiation with electrons where the sharp and steep breakdown occurs for the device irradiated with 2000 rad and 3000 rads.

The surface of the semiconductor device may have dangling bonds which are undesirable. Hence, these dangling bonds are usually got passivated by passing hot oxygen gas over the surface. This will cause the formation of SiO_2 layer. The $Si-SiO_2$ interface, so formed, are highly prone to ionization damage. Ionizing radiation can introduce hole traps at the $Si - SiO_2$ interface layer. The breakdown action of the zener diode is explained on the basis of avalanche multiplication of the charge carriers as well as the tunneling action of the charges. The presence of hole trap a the interface layer can slow down the avalanche process due to the accumulation of the electrons at the surface layer near the depletion region. Then, after irradiation, the break down of the zener diode require increased reverse bias. as observed from the graph.

Saturation effect of the number of hole traps, so generated, can also be observed from the graph. When the dose was made larger, the shift in the breakdown

voltage increases. At a dose of 1500 rad and above, however, the zener breakdown value reaches a maximum and further shift in the breakdown voltage was not observed on increasing the dose. Since, the interface traps are not easily self annealed, radiation hardening effect could be achieved by irradiating the device to saturation dose at the time of production.

The steep fall of the reverse characteristics during the breakdown also could be understood in terms of the same effect. Since the avalanche process is delayed due to accumulation of electrons at the interface, larger reverse bias is needed for the breakdown to happen. This will continue till the accumulation process is saturated. During this time, the avalanche electrons that has not been accumulated would achieve larger energy. Hence, immediately after the saturation, there will be a sudden increase in the rate of avalanche process causing an abrupt multiplication of charges along with release of accumulated charges. This will cause sudden breakdown of the diode. Hence, the breakdown would be more steeper. This was the effect observed in the reverse characteristic curves of zener diode after irradiation.

6.4 Effect of Ionizing Radiation on Transistors

Similar studies were done to see the effect of radiations transistors due to electrons and photons

6.4.1 Transistors - Photon irradiation effect study

- Transistors. Pre-irradiation Characterization

ExpEyes was used to characterize the transistor. All the samples used in the study used BC 547 transistor with identical Volt-Ampere characteristics. The output characteristics of the transistor BC 547 was plotted for input current, $I_B = 10\mu A$, $I_B = 30\mu A$, $I_B = 50\mu A$, respectively, keeping the collector voltage constant at 5 volts, shown in figure (6.20).

- Transistors - Photon Irradiation Study - Post-Irradiation Characterization

The transistors were irradiated with Bremsstrahlung X-rays of two different photon energies. One of the devices was exposed to 6 MeV and the other device

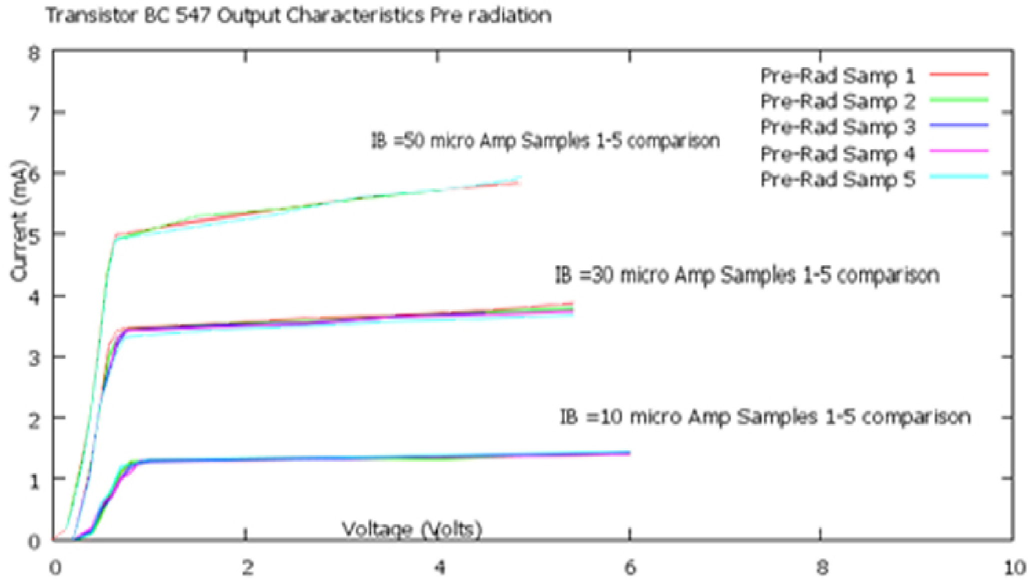

Figure 6.20: BJT Pre-irradiation output characteristics for $I_B = 10, 30, \&50(\mu A)$

was exposed to 15 MeV. After irradiation, analysis were done using ExpEyes. The output characteristics of the device, irradiated with 6 MeV photon and that irradiated with 15 MeV photons were plotted in the same graph (Figure 6.21) along with pre-irradiation characteristics. A shift in the collector current is observed. But, there is no observed change in collector current for change in energy.

- Transistors - Photon Irradiation Study - Post-Irradiation Characterization-Dose effect.

Effect of variation of photon dose on the output characteristics of the transistor was also studied. Three different transistor were irradiated by 6 MeV photons in to doses of 300 rad, 500 rad and 1000 rad. After irradiation the output characteristics of all the samples were plotted in the same graph (figure 6.22). It was observed that, for a dose of 500 rad or less, there is an enhancement in the collector current compared to that of pre-irradiation for the same collector emitter voltage. However, when the dose was increased to 1000 rad, the characteristics became almost similar to that of pre-irradiated characteristics. This may be the annealing due to heating effect.

6.4.2 Transistors - Electron irradiation effect study

- Transistors - Electron irradiation study - Pre-irradiation characterization

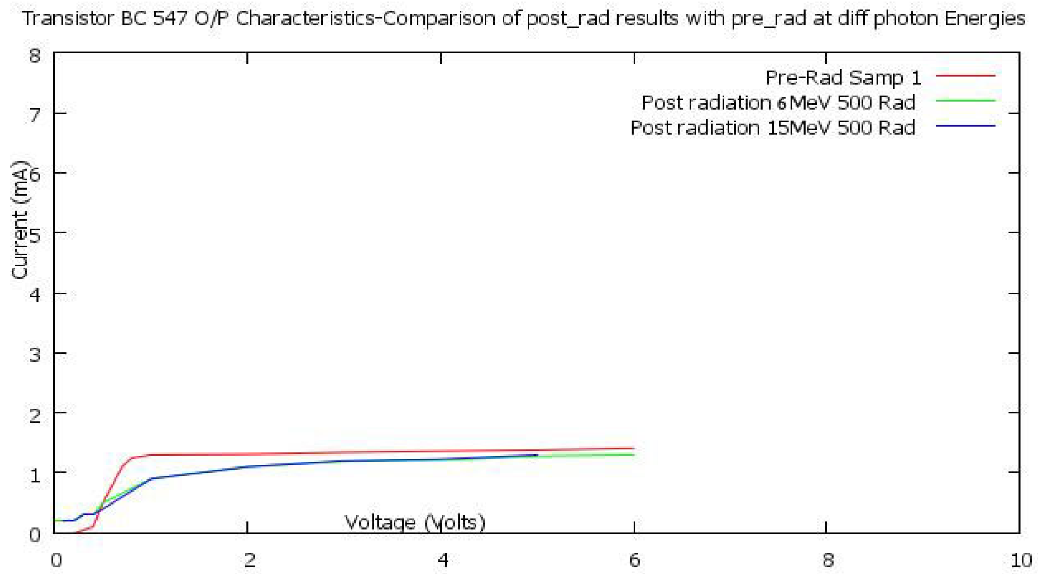

Figure 6.21: Comparing pre-irradiation characteristics with that of post-irradiation under two different Photon energies at I_B= 10 micro Amps

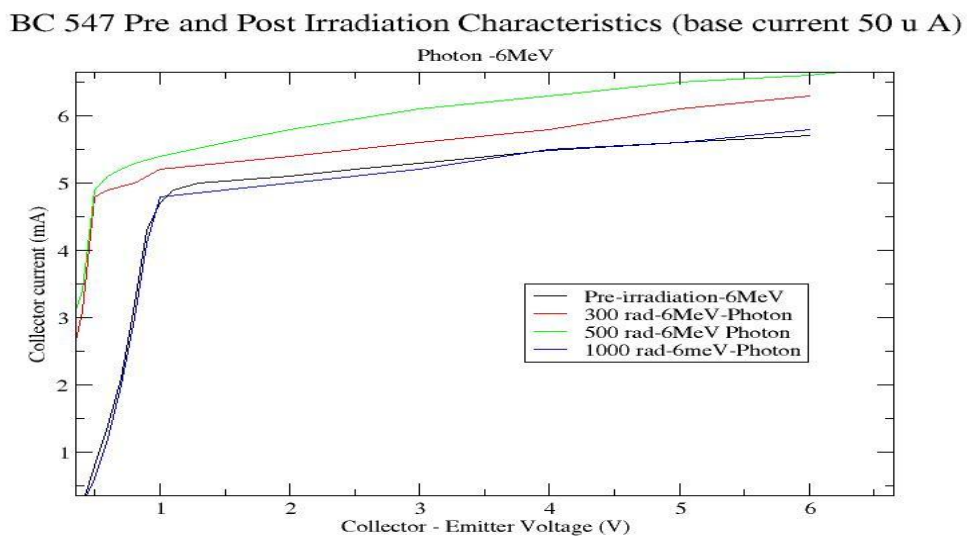

Figure 6.22: Comparing the output characteristics of transistors irradiated with photon of different doses with that of pre-irradiated device

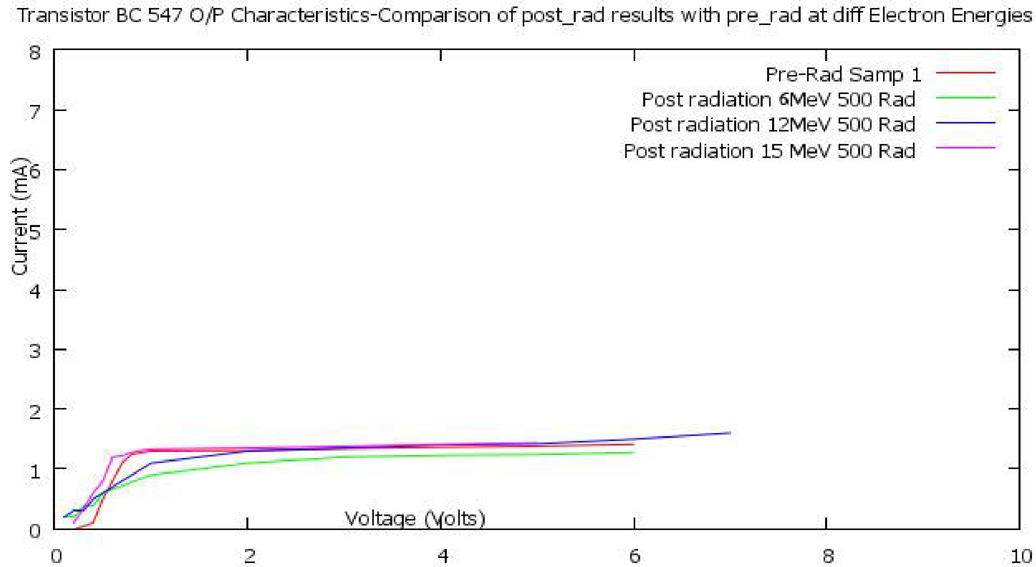

Figure 6.23: Comparing the output characteristics of transistors irradiated with electrons of different energies with that of pre-irradiated device

BC 547 low power transistor was used for the experiment. As with photon irradiation experiment, the output characteristics of all the samples were found to be identical at $I_B = 10\mu A, 30\mu A$, and $50\mu A$, for 5 different samples used in experiment.

- Transistors - Electron Irradiation Study - Post-Irradiation Characterization

The transistors were irradiated with Bremsstrahlung X-rays of three different electron energies. One of the devices was exposed to 6 MeV and the other device was exposed to 12 MeV and the third device was exposed to 15 MeV electron beam to a dose of 500 rad each. After irradiation, analysis were done using ExpEyes. The output characteristics of the device, irradiated with 6 MeV electron and that irradiated with 12 MeV and 15 MeV electron were plotted in the same graph (Figure 6.23) along with pre-irradiation characteristics. Here also,like photon energy effect,There is a small shift observed in collector current for 6 MeV electron irradiation. For devices irradiated with 12 MeV and 15 MeV beam the output current is almost the same as that of pre irradiation characteristics except that they did not possess a sharp saturation voltage like that of pre-irradiated transistor. In general, There is no variation in collector current with change in energy of the electron.

- Analysis and Features.

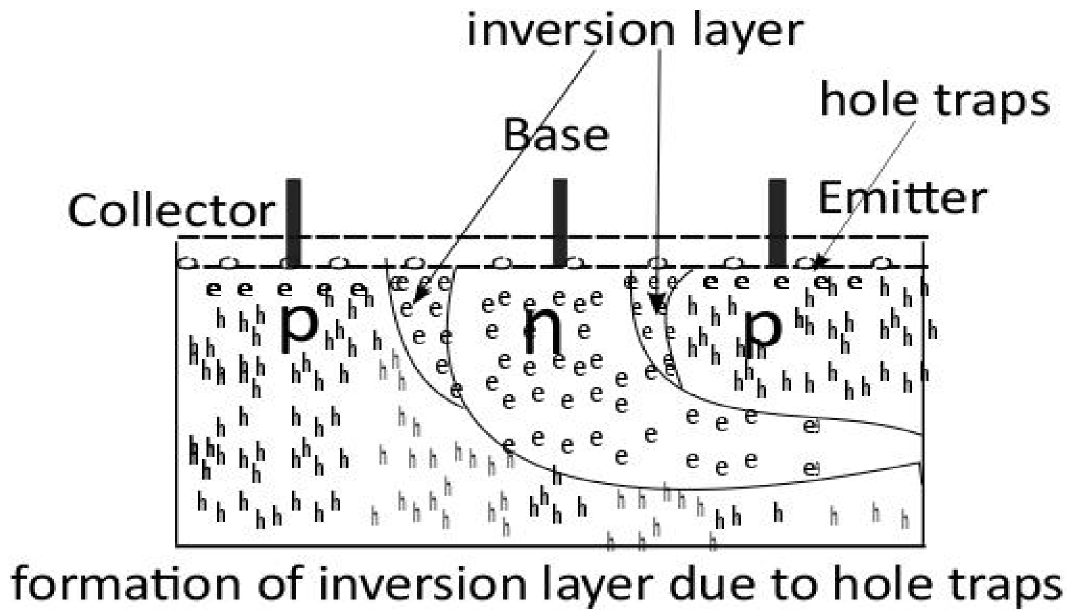

Figure 6.24: Hole traps near the surface and the insulating layer result in the formation of inversion layer

The most important surface effect of ionizing radiation was the accumulation of charge on the device surface. This charge, affect the underlying semiconductor surface and causes the degradation of device characteristics, particularly the leakage current of p-n junction and the gain of transistors. For non-passivated transistors these charges affect the devices more directly and such devices are more sensitive to radiation effect. In passivated devices space charge will accumulate in the SiO2 and near Si-SiO2 interface and causes device degradation. (Ref. Figure 6.24).

It could be concluded that, the exposure of BJTs to Bremsstrahlung photons or electrons has caused ionizing radiation damage, mainly by the excess charges trapped on or near the surfaces of their insulating layers and interfaces. This phenomenon has reduced the minority carrier lifetime and thus, leading to a decrease in the current gain of the BJTs.

6.5 Transistors - Radiation Effect - *in-situ* Study of the Device Characteristics

Most of the studies on the effect of radiation were done, offline by irradiating the device to the specified dose by radiations of selected energies and the characteristics were studied after irradiation. The measurements and characterization are not simultaneously made during the time of radiation. However,

In the space environment the device will be exposed to radiation while it is active. The design of modern radiation detectors with embedded amplifiers and data processing system, electronic space application systems etc. needs the consideration of such a study. Hence, it is essential to make quantitative and qualitative evaluation of the performance characteristics of these devices during the time the device exposed to radiation. Keeping the above facts in view, the variation of characteristics of the transistor 2N 2222 during the time of exposure to gamma rays/ high energy Bremsstrahlung has been measured and analyzed. Commercial transistor 2N 2222 has been irradiated separately with 6 MeV and 15 MeV photons from LINAC. The collector characteristics were studied during the irradiation at a constant base current. The details of the experiments are discussed in section below.

6.5.1 The Experimental setup

Device and systems

The experimental set up was designed to obtain online data from device being exposed. The transistor 2N 2222 under test was connected to ExpEyes [10] which serves as programmable data acquisition system. A computer system installed with ExpEyes software was connected to ExpEyes hardware by means of a long USB cable of 1 meter length which was also shielded for radiation protection.

ExpEyes was configured for the data acquisition from the transistor. It has been built around a 16 bit micro controller programmed in C language to control the hardware modules ADC, DAC, amplifiers, oscillators, digital and analogue input and output connectors and sensor input connectors. A hardware communication library written in python language installed in a PC can communicate with hardware module. Users could make use of the various classes in the hardware communication library from python development environment to control the hardware. Other python modules such as *eyeplot.py* and *eyemath.py* could be included in the python program for graphics and data functionalities. The built in code was used for the experiment for characteristic study. ExpEyes has a constant current output which was set to 12 micro-ampere to provide the base current of the transistor. The equipment has an accuracy of 1.22 mV /bit.

A peer to peer network was employed to control this PC (PC-1) from another PC (PC-2) located in the control room of radiation lab via remote desk top

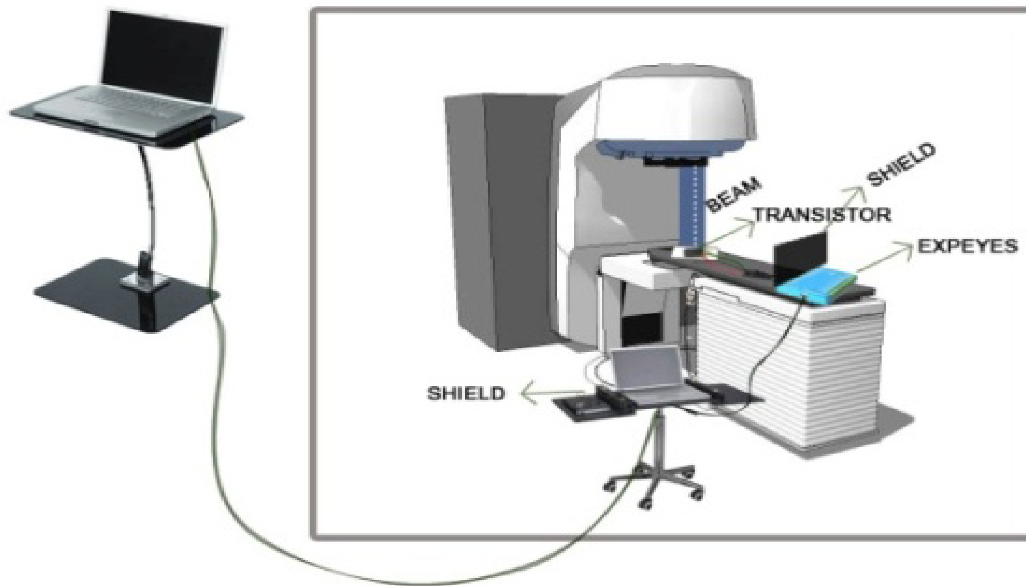

Figure 6.25: experimental setup

access tool VNC. A twisted pair CAT 5 network cable was used, which has good performance up to 100 MHz.

2N 2222 - silicon planar epitaxial NPN transistor in TO 92 packages from NTE Electronics was used to study the variation in the characteristics of transistors. It has been reported that, the radiation effect has a very little variation with regard to packaging and orientation for the same device technology [6]. Hence, the orientation of transistor to the radiation beam was neglected. The maximum rating of collector current for this transistor is 800 mA, max V_{BE} is 5 V and V_{CE} is 30-40 Volts. The maximum junction temperature is 200^oC.

Data acquisition and deduction

The experimental set up is shown in Figure 6.24. The transistor was positioned exactly at the beam line by the help of laser cross beams provided with the machine. The transistor under test was connected to ExpEyes by means of shielded copper wires of 10 cm long. ExpEyes was, then, connected to PC-1 arranged inside the lab by means of a USB cable of 1 meter long. ExpEyes has been pre-calibrated with the USB cable provided with the instrument to connect with PC-1 which has the ExpEyes Software to control the ExpEyes hardware. PC-2, arranged in the control room, was connected to PC-1 by means of a cable (CAT 5) of 30 meters long and ExpEyes parameters were set using PC-2. The data flow sequence of the experimental setup is shown in Figure 6.25.

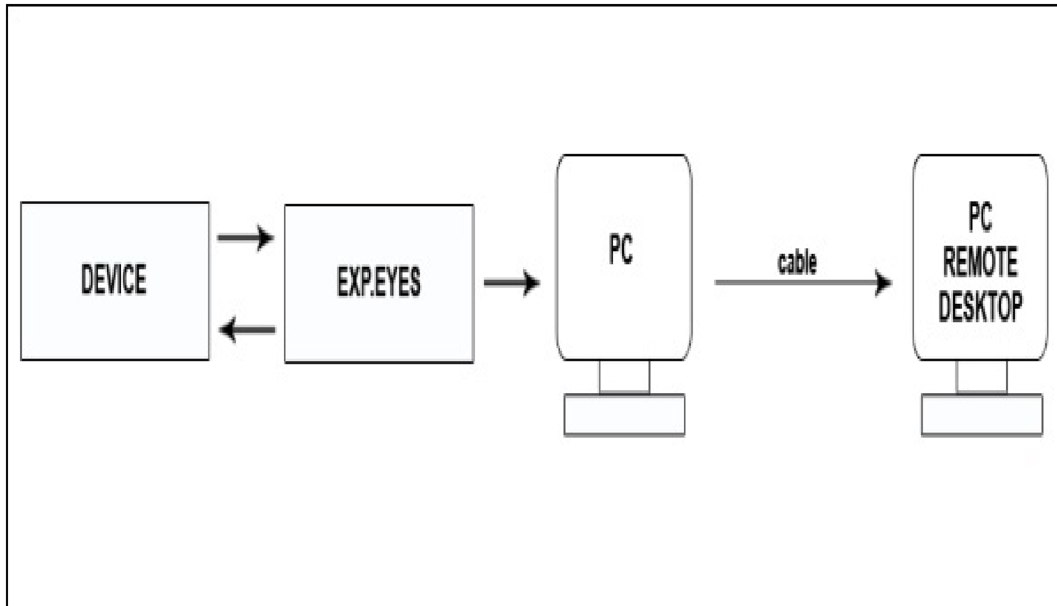

Figure 6.26: data flow sequence

Initially, pre-irradiation characteristics of the transistor 2N 2222 was measured by invoking ExpEyes software code from PC-2 for a base current setting of 12 micro amperes while the voltage was set to vary linearly with time. The data was plotted.

The LINAC was set for 6 MeV X-ray photon. The dose and dose rate can be varied each time the observation is carried out. The dose measurements were done automatically by the machine setup and displayed on the screen. Towards the end of the exposure, ExpEyes was invoked to collect the transistor collector current data against the voltage, at fixed intervals of time to form a time series data. The experiment was repeated for doses of 500, 1000 and 2000 rad for the same dose rate.The data is plotted in fig 6.27. It was seen that, total dose doesn't seem to have much effect in the characteristics under 6 MeV gamma radiation except for the random signal or noise current produced by the device. It is seen that, the variation of dose did not have significant effect on the collector current for 6 MeV

The results obtained in the above observation naturally prompted to study the effect of varying dose rate of the irradiated gamma rays and hence the measurement was repeated for a total dose of 500 rad with dose rates of 500 rad/minutes and 50 rad/minute base current of 12 micro amperes. The data was collected during the time of irradiation for the same base current of at the end of achieving the same total dose of 500 rad. It was seen that, the variation of dose rate did not have significant effect on the collector current. In order to check the dependence on cumulative dose, the experiment was repeated for

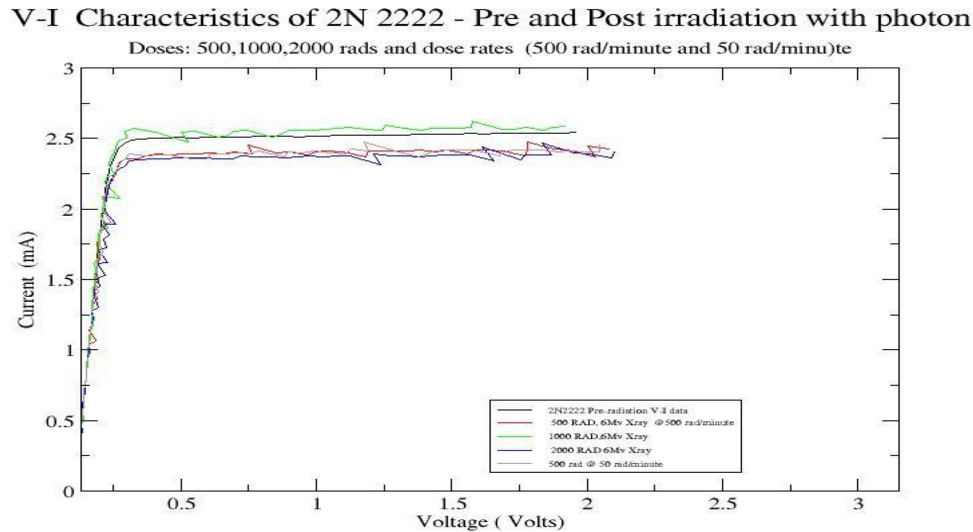

Figure 6.27: Effect of cumulative dose and dose variation effect of 6 MeV Xrays on transistor to produce random noise with instances of negative resistance

cumulative dose of 500 rad with a dose rate of 500MU/minute and was plotted along with the data for 1000 rad at same dose rate. The result is summarized in figure 6.27.

In order to observe the effect of photon energy, the experiment was repeated for a photon energy of 15 MeV at a cumulative dose of 500 rad with dose rates 500 rad/minute and 50 rad/minute. It could be seen that, there was significant reduction in collector current. Further, it is interesting to note that, there was no significant dependence of collector current on the dose rate. The results are summarized in figure 6.28.

From the above observations shown in fig 6.27 and 6.28, it is seen that, the collector current is significantly varied for a gamma exposure of 15 MeV, where as, the photon of 6 MeV does not produce significant change in the collector current. Further, dose rate or cumulative dose did not have any effect on the collector behavior for both the energies. The entire observations are summarized in figure 6.29.

It is interesting to note that there is a marked difference in characteristics in the offline measurement and in online measurement in respect of response to energy and dose effect. In off-line studies dose effect was seems to be significant where as in the case of online study, dose effect was not prominent while energy effect is much more sensitive. It may be inferred that, the effect observed in the offline analysis is due to the total heat dissipated in the lattice and the surface trapping

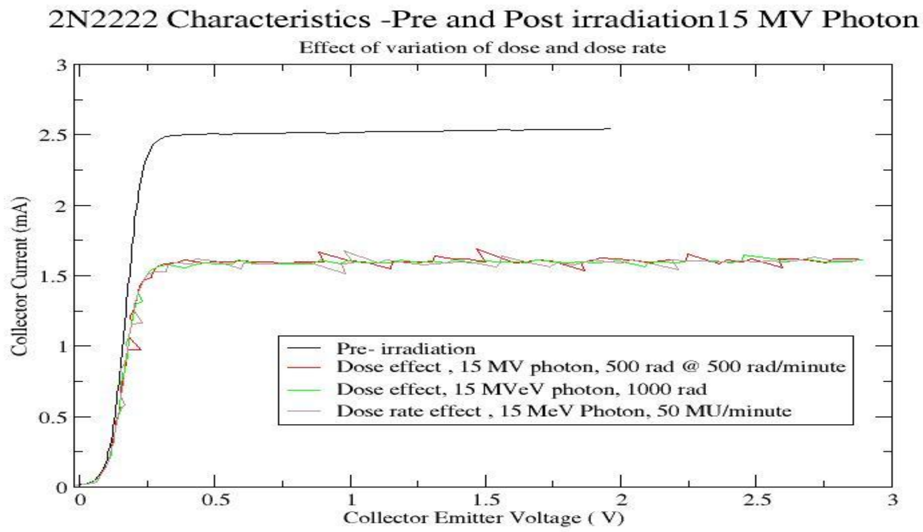

Figure 6.28: Transistor 2N 2222, Effect of dose and dose rate of 15 MeV photon irradiation

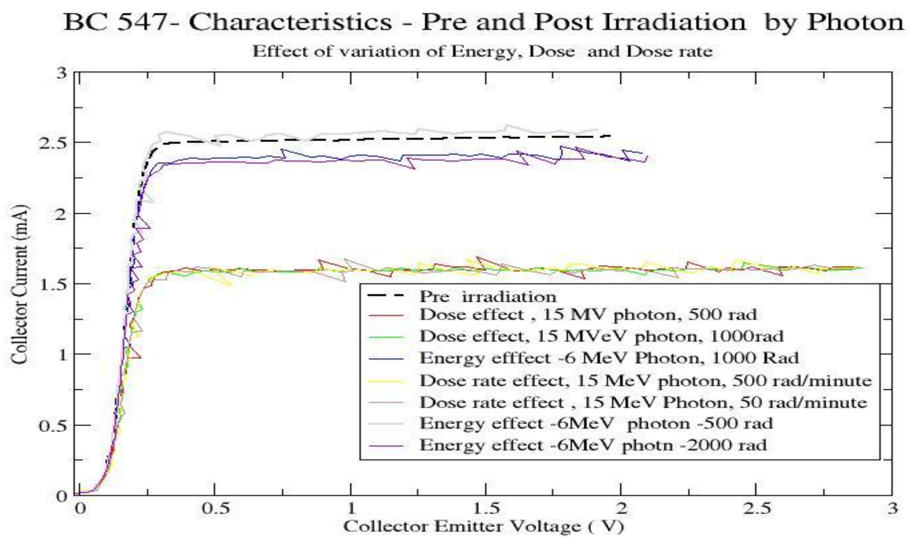

Figure 6.29: Transistor- BC 547, Effect of dose , dose rate and energy of photon irradiation

whereas, the effect observed in the online studies is due to the instantaneous availability of charge carriers, traps and their mobility,as explained below.

The significant decrease in the steady state collector current may be attributed to the trapping of charge carriers in the surface trap centers formed in between silicon and the oxide layer due to irradiation. This effect is expected to persist even after irradiation and subjected anneal out due to various causes including room temperature annealing in due course. In the case of higher energy, radiation may penetrate in to deeper layers creating e-h pairs in the base regions, similar one to photo injection process, altering carrier concentration in the regions where energy is dissipated. Since the mobility of electron is larger, the electrons will immediately diffused or drifted away. This will cause an increased concentration of holes in the base region. This will affect the base current as observed in the online study.

Random telegraphic signals observed and its analysis

It is interesting to note that, in all the above cases, the collector current has showed a low varying random fluctuation with the instances of switching into negative resistance in the collector region. The negative resistance during irradiation under electric field may be attributed to radiation induced defects in the band gap which under electric field may cause enhanced thermal generation of carries due to Poole Frankel effect. On reaching the conduction band, the electron can move through the crystal, for a brief amount of time, eventually relax into another localized state.

The close analysis revealed that, it reflect, the superposition of multiple frequency random telegraphic signals on the steady state collector current. During, the irradiation of transistor device by gamma rays, in addition to e-h pair generation there would be rare events of displacement [11,12] which, in turn, would have caused trapping and release of charge carriers and random telegraphic signals of varying time base. The possible superposition of all such waveforms would give rise to the observed low varying patterns on the collector current, discussed below.

Gamma and X-rays produce rare displacement through compton scattering [13]. The defect site generated due to radiation induced displacement effect may cause alternate capture and emission of carriers with the result that, the device resistance value may switch discretely. This will cause low frequency noise

referred to as Random Telegraph Signal. The study of RTS can give insight in to the defect location in the device.

The energy of the trap centers [14] that falls in the range of energy gap of semiconductors will cause temporary energy states in the band gap region, where, the carriers may first absorbed and, then, released [15]. When the carriers are absorbed, they will no more be available for conduction causing a reduction in current and the current will be enhanced when the carriers are released. The capture and release might have a wide range of time constant depending on the position of energy level in the band gap. The trap center with energy near the middle of the band gap is easily filled and easily released while this time constant will vary exponentially with the location of their energy level move away from the mid gap[14].

A free carrier in a conducting media stopped by the trap center would not be available for current transport. Random telegraph signal observed in the experiment is the modulation of charge carriers with wide spread relaxation time described by Poisson point process. The number of points in the disjoint interval are independent. The number of possible events may be large, but each of which is rare. Hence Poisson distribution model is appropriate [16].

The probability of observing m events (Telegraphic signal) in a time T is:

$$P(m,T) = \frac{(\nu T)^m}{m!} exp(-\nu T) \tag{6.2}$$

where ν is the mean rate of transition per second. $\nu T = \lambda$ is the intensity of the Poisson point process.

The capture and emission kinetics of the individual defects could be understood by considering the probability of transition from high current state (state 1) to low current state (state 0) and back at a definite interval of time. The superposition of such states due to all the defect centers or the modulation of RTS signals from all such defect centers will lead to the low frequency noise signals similar to 1/f noise. Assume that, probability per unit time for transition from state 1 to state 0 is $\frac{1}{\tau_1'}$ and that from state 0 to state 1 to state 0 is $\frac{1}{\tau_0'}$. Let $A(t)$ is the probability that, there is no transition from state 1 to state 0 in a time t. Then, the probability that, the state 1 will not make a transition between 0 and t and that do make a transition to state 0 between t and $(t + dt)$ is given by,

$$P_1(t)dt = \frac{A(t)}{\tau_1'} \tag{6.3}$$

Similarly, probability of not making a transition between time 0 and $(t + dt)$, is the product of probability of not making a transition between time 0 and t and that between t and $(t + dt)$ is given by:

$$A(t + dt) = A(t)(1 - \frac{dt}{\tau_1'}) \tag{6.4}$$

ie,

$$\frac{(A(t + dt) - A(t))}{dt} = -\frac{A(t)}{\tau_1'} \tag{6.5}$$

Or,

$$\frac{dA(t)}{dt} = -\frac{A(t)}{\tau_1'} \tag{6.6}$$

On integration,

$$A(t) = exp(-\frac{t}{\tau_1'}) \tag{6.7}$$

Equation(3) yields,

$$P_1(t) = \frac{1}{\tau_1'} exp(-\frac{t}{\tau_1'}) \tag{6.8}$$

Hence, the probability that the state 0 will not make a transition between 0 and t and that do make a transition to state 1 between t and $(t + dt)$ is given by,

$$P_0(t) = \frac{1}{\tau_0'} exp(-\frac{t}{\tau_0'}) \tag{6.9}$$

. Thus the up and down transitions have exponential characteristics distributed in time. Hence the relaxation times of various states have exponential distribution, even though the capture and emission process is purely random as in equation (1). The formation of lattice defect introduced during the passage of radiation introduce energy level within the band gap as in Figure (6.30). Most active traps are near the intrinsic level. As the energy level pass away from the mid-gap, there would be an exponential decrease in the relaxation time [14].

The low frequency noisy wave form observed to have super imposed on the constant collector current region of the Gummel plots was the result of linear

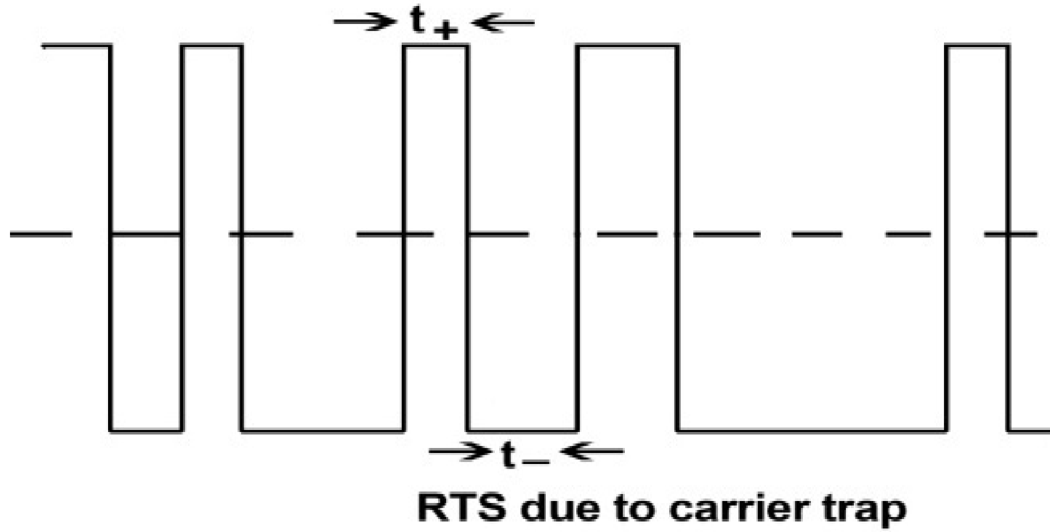

Figure 6.30: Random telelgraphic signals

superposition of exponential relaxation processes caused by defect sites. The nature of RTS signal is as in Figure (6.31). The auto correlation function of the RTS signals could be written as

$$\phi_t(x) = a^2 exp(-\frac{t}{\tau_z}) \tag{6.10}$$

Random Telegraphic signals

The power spectrum due to noise signal characterized by an exponential autocorrelation function may be calculated by Einstein- Wiener-Khintchine theorem. According to which,

$$S_{X(\omega)} = 4\int_0^\infty \Phi_{X(\tau)} cos(\omega t) d\tau \tag{6.11}$$

$$S_{X(\omega)} = (2a)^2.(\frac{\tau_Z}{1+\omega^2\tau_z^2}) \tag{6.12}$$

If $P(\tau_z)$ is the probability distribution of τ_z ,then, Power spectral density of total carrier fluctuation is:

$$S_n(\omega) = 4\Phi_n(\tau = 0)\int_0^\infty \frac{\tau_z P(\tau_z)}{1+\omega^2\tau_z^2} \tag{6.13}$$

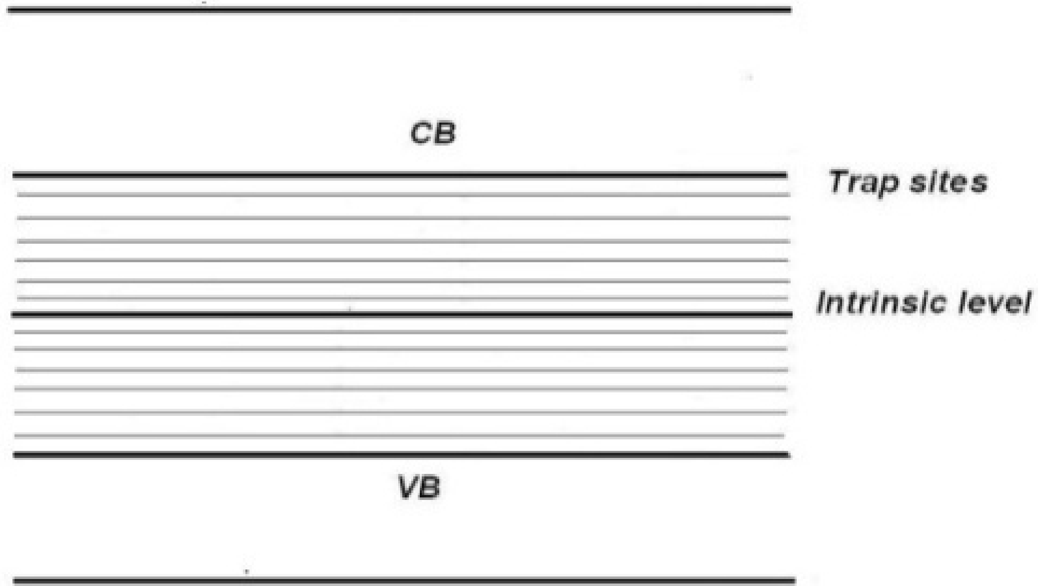

Figure 6.31: Energy levels due to traps within the band gaps

Thus, if a noisy wave form $z(t)$ has an exponential relaxation process with time constant τ_z, the power spectral density has the general form

$$S_Z(\omega) = \frac{g(\tau_z)}{1+\omega^2\tau_z^2} \tag{6.14}$$

where $g(\tau_z)$ depends on the generation mechanism of random pulse train. The linear superposition of all such relaxation process with time constant distributed between τ_1 and τ_2 is obtained by integrating $S_Z(\omega)$ from τ_1 to τ_2 Hence we get,

$$S_X(\omega) = \int_{t_1}^{t_2} S_Z(\omega) P_{\tau_z} d\tau_z \tag{6.15}$$

$$S_X(\omega) = \int_{t_1}^{t_2} P(\tau_z) \frac{g(\tau_z)}{1+\omega^2\tau_z^2} d\tau_z \tag{6.16}$$

The product$P(\tau_z)g(\tau_z)$is equal to a constant P, the above integral reduces to;

$$S_X(\omega) = P\frac{(tan^{-1}(\omega\tau_2) - tan^{-1}(\omega\tau_1))}{\omega} \tag{6.17}$$

If $\omega\tau_2 >> 1$ and $0 <= \omega\tau_1 << 1$, then, the above equation become

$$S_X(\omega) = \frac{K}{\omega} \tag{6.18}$$

where K is a constant.

Thus the superposition of relaxation process due to radiation induced trap centers can give rise to a power spectrum of the form above which has the same nature of the power spectrum due to $1/f$ noise[17].

The low varying signal over collector current observed on the Gummel plots of common emitter configuration of gamma irradiated transistors described in above experiment is analyzed to have been due to the Random Telegraph Signals originated from the selective trapping and release of carriers in the radiation induced trap centers in the band gap region of semiconductor. The relaxation time of various trap centers are related by an exponential auto-correlation function. The trapping and release of carriers from individual trap site may be considered as pulse trains of varying time constant and superposition of all such pulse trains due to trapping and release of carriers from various trap sites can give rise to noise signals. The power spectrum of such noise signals is similar to 1/f noise. This must be distinguished from the normal 1/f noise generated in various electronic devices and systems.

6.5.2 Phase - 3 - Ground test on the device used in space - Analysis of proton irradiation effect on SCD (CCD236) X-ray fluorescence detector

Electronic devices are constructed utilizing various materials, technologies, configurations and packaging. The devices find various applications. For space applications, devices are to be radiation hardened to combat with possible radiation damage of the device. Shielding of the device cannot be a solution in most of the cases due to secondary radiations. Solar cells and other devices which form the part of camera, detectors etc. should not be shielded, anyway, for its working. Radiation damages to the devices and system could be modeled to some extent. However, to understand the accurate damage profile of the devices and system, ground simulation test should be conducted on the device, exposing the device to an equivalent dose to which, the device may be exposed during mission period. Considering this interest, a real time application device in space used as *X-ray Fluorescence Detector* under the name *Swept Charge Device* was subjected to ground test in our study. The SCD prototype used in the study is shown in fig (6.32)

A detailed theory and the working principle of SCD are given in the chapter 4 sections 3.4. SCD prototype view , structure and internal layout, process of of charge collection and charge transfer techniques are also explained in

prototype.jpg 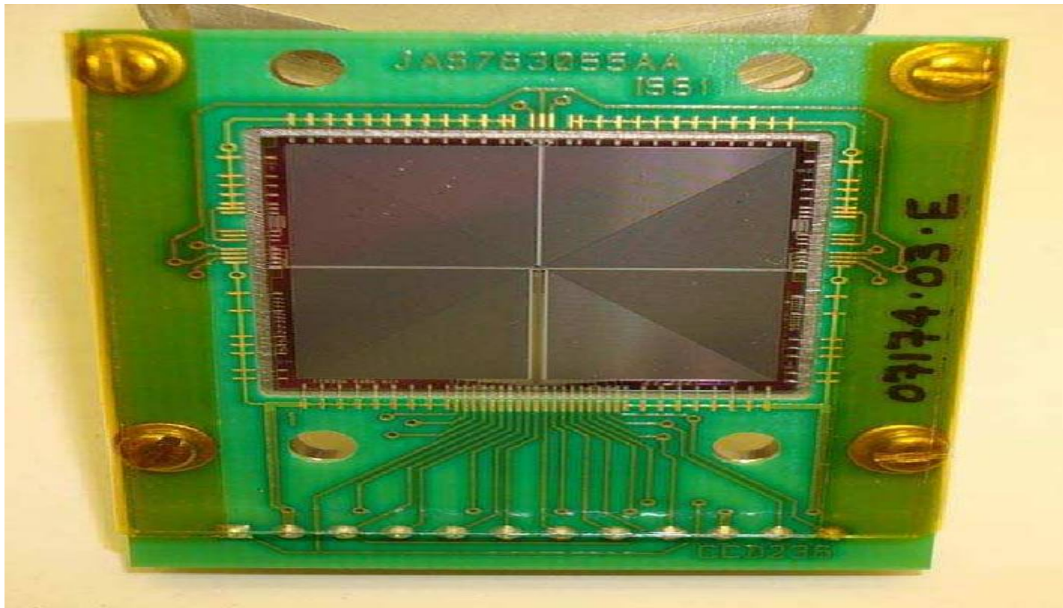

Figure 6.32: CCD Prototype

this section. The Effect of proton irradiation on SCD and the subsequent self-annealing effect were experimentally determined and analyzed. Since SCD is used as a detector for X-ray photons, the damaging effect of SCD due to radiation that may affect the resolution of the detector is of utmost concern. This is because the scientific data derived out of the X-ray fluorescent spectrum demand high resolution for the characteristic peaks in the spectra. The SCD prototype used in the experiment and its structure is shown in figure 6.32 and 6.33

Even though, many of the causes of damages were recognized, the extent of damage to total dose effect at different energies is to be studied systematically for various operating condition. The study requires experimental setup for analyzing standard spectra before irradiation and that after irradiation at different operating conditions of the CCD. Hence, the first part of the experiment was done to determine the resolution of the CCD at various operating conditions such as clock voltage, clock frequency and the temperature. The temperature being the most important parameter as the performance of the CCD varies considerably with operating temperature. The section below describe the experiment done to optimize the CCD for the on-board operation of Chandrayan II mission.

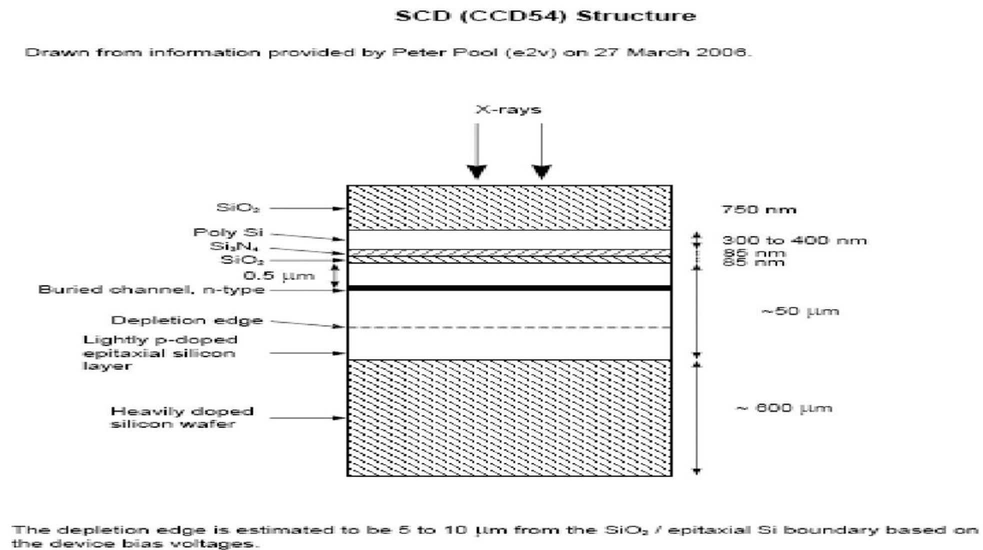

structure.jpg

Figure 6.33: SCD structure

Optimization Study of SCD X-ray fluorescence detector proposed for the use in Chandrayan II mission.

One of the objectives of CLASS experiment proposed in Chandrayan-2 mission is the mapping of elemental abundance on the surface of the moon while traversing the lunar polar orbit at a distance of 200 Km above the surface. Swept Charge Device (SCD), a large area X-ray Fluorescence Detector, will be used for this purpose. When the satellite is on the orbit of the moon, SCD can detect the X-ray fluorescence from the surface of the moon due to X-ray from the sun falling on the surface of the moon. This fluorescence spectra will have the information of the elemental abundance of the surface layer of the moon. This will also give information on the elements in the meteors and asteroids that has formed large crates on the surface of the moon. CCDs could be cascaded to form large area detector so as to form spectral image of low intensity X-ray peaks. This is one of the advantage of SCD over other detectors. SCD also offer high resolution of the spectral lines which is most important for such analysis. It is the spectral resolution that is expected to be affected severely due to irradiation.

The ability of the spectral resolution of SCD, in terms of FWHM of the spectral peak, at various operating parameters of the device and the optimum operating parameters were determined . The device is likely to degrade during the course of its use in the space mission due to the expected space radiation damage caused by protons. The resolution has to be so fine, so that, even a little shift in the resolution caused by the radiation damage of the device should be

within the accepted performance criterion. *Charge Transfer Efficiency* (CTE) and *Dark Current* are the performance parameters of a SCD that determine the resolution of the SCD. CTE is affected by the *Clock Voltage* and *Clock Frequency* . Dark current determines the operating temperature. The optimum operating parameters of such devices are usually determined by trial and error methods for the particular situation. Hence, it was required to determine the optimum operating parameters of the device such as *operating temperature* , *Clock bias voltage* and *Clock frequency* for the best resolution.

The device performance parameters were determined prior to proton irradiation at ISRO - ISAT center, Bangalore. A systematic approach was done to optimize the operating parameters of the device to be used in space application. The spectral resolution of the SCD was determined for the $K\alpha$ and $K\beta$ X-ray spectral peaks emitted from Fe^{55} source by measuring the FWHM of the peaks. The experiment was done by varying one of the parameters while keeping the values of the other parameter constant. This was repeated for other parameters also in a converging method. Optimum operating parameters that satisfy the targeted spectral resolution lesser than 150 eV for the above spectral lines were determined.

Experimental setup

The setup, for optimization consisted of a source of X-ray, a vacuum chamber that connected to a vacuum pump, a temperature controlling system and SCD driver electronics board with XCAM software for the control and data acquisition of SCD. The source of X-ray was Fe^{55} which emits soft X-ray. The advantages of the Fe^{55} emitted X-rays are that, it is monochromatic and produced continuously over a years-long period. There are two prominent peaks of interest in the experiment. They are the $K\alpha$ and $K\beta$ lines of energy 5.89875 keV and 6.49045 keV respectively. The source was kept in a metallic (lead) container with a long narrow opening sufficient to produce a collimated beam. Vacuum system consisted of two cascaded pumps. A backing pump that creates a vacuum up to 10^{-2} mbar and a turbo molecular pump that could create a vacuum of 10^{-4} mbar. The normal operating speed is 56 KRPM.

The cooling system consisted of a *Thermo Electric Cooler*, *Temperature Controller* (MTTC -1410-Melcor Corporation) backed by a *PID Controller*. SCD was mounted on a cold plate. The temperature was kept constant by circulating water through the cold plate attached to the SCD. The PID controller (TEC

Controller DX 5100) from RMT Ltd, Moscow, ensured high degree of temperature stability. Temperature of the device cooled by thermoelectric plate was continually sensed by PT 1000 temperature sensor and displayed by the system. An overall temperature stability of $(+/-0.1^oC)$ was achieved by the system.

SCD has a driver which in turn connected to a PC. The SCD driver could pass the data to PC. The SCD driver provides the voltage sequence for the SCD for the operation and the power and ground required for the pixel array and the embedded charge to voltage amplifier within the device.

The controlling and data handling of SCD is performed using X-CAM software mentioned in chapter 5 . X-CAM software read 216 data sets in an experiment to record the spectral details. X-CAM provides various settings such as sequential file, voltage file, delay etc. which may need to vary to obtain the optimized values. In the experiment to study the dependence of temperature on FWHM, the sequential file, voltage file and delay are kept constant and the temperature was allowed to change by predetermined value.

SCD, with its driver board was kept on the top of the cold plate at the center of the vacuum chamber which has a mylar window. Fe^{55} source was kept above the window so that, X-ray falls on the top of top left quadrant of SCD. PT 1000 temperature sensor was fixed on the cold plate. The connection leads from the driver board, temperature sensor and tubes of the circulating water etc. could be taken out of the chamber.

Temperature has been changed in steps of 5 degree from $+5^oC$ to -35^oC. Clock speed was set to 100 kHz and the frames were chosen to be 300. All these settings could be made using XCAM software. Data was captured by XCAM software and stored in a PC. The data consisted of the density of counts against channels number.

Analysis

A typical spectrum from Fe^{55} source recorded by SCD kept at -20^oC and applying clock voltage pulse of 7.0 V at a frequency 100 kHz is shown in figure (6.34). Typical X-ray spectrum emitted by Fe^{55} source as recorded by SCD at temperature -20 degree. Noise peak,$MnK\alpha$ and $MnK\beta$ are seen in the plot.

The spectrum was plotted as histogram of the photon counts observed versus channel number. Matlab code, described in chapter 5 section 8 is used to

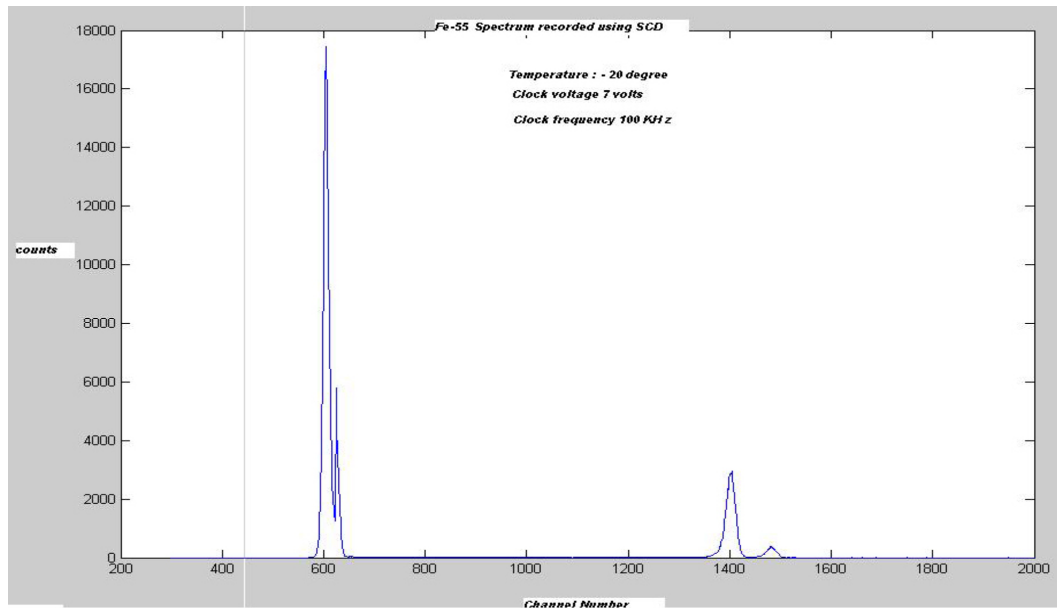

Figure 6.34: Typical X-ray spectrum emitted by Fe^{55} source as recorded by SCD at temperature -20 degree

calibrate the spectrum by interactively choosing the known energy peaks. The spectrum consisted of three major peeks and other peaks with less intensity. The first and the largest peak being the noise peak at zero energy. This is also called the Zero peak'. The second being the Mn Kα peak at 5.9 MeV the third important being 6.4 MeV Mn Kβ peak. Other peaks such as Mn Kα and Kβescape peaks were also observed by magnifying the region involved.

To evaluate the performance of the device or the resolution of the device, we measured the FWHM of the peaks. To measure FWHM, the spectrum was calibrated using the known energy values of the peaks and the corresponding channel number. The calibrated spectrum was displayed on the screen. The peaks were selected interactively from the spectrum on the screen using a mouse. The selected peaks were given a Gaussian fit and the resulting new data points are taken for calculating FWHM. The whole process was done using computer codes written in Matlab. The code was written to measure the density of counts under the peak , the calculate value of FWHM and to transfer the data in to a flat file for later analysis.

The FWHM of Fe^{55} spectral peaks were measured before irradiation. The resolution depends on temperature, clock frequency and clock voltage. So, each of these parameters has been varied , systematically, and fixed up best operating parameters for the device to be used on-board during the mission. Optimization is also required for comparing post irradiated data with that of pre-irradiated data , based on optimized operating parameters

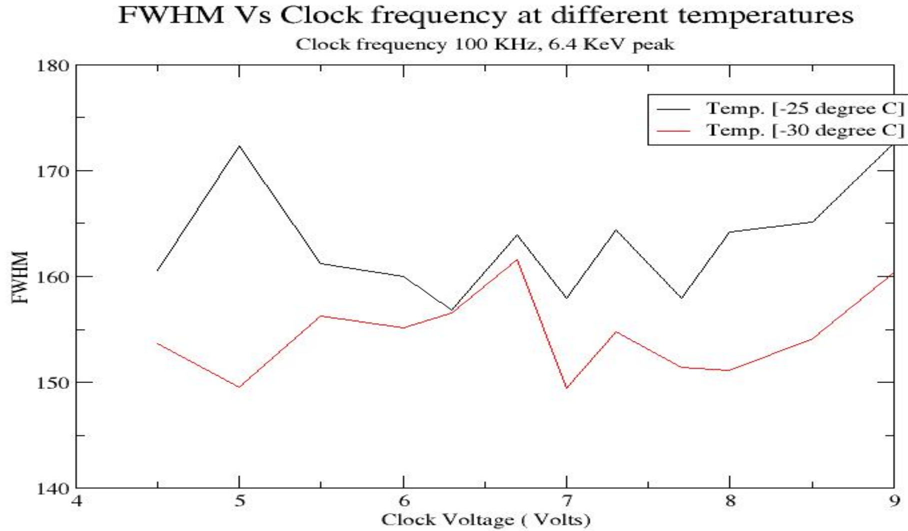

Figure 6.35: Mn Kα peak : Variation of FWHM with clock voltage at different temperatures

- SCD Pre-irradiation Analysis: FWHM Vs. Clock Voltage at Different Temperatures at 100 kHz.

Observed FWHM of the spectral lines for the optimization of clock frequency, clock voltage and temperature are plotted through figures 6.33 to 6.40

Figure 6.35 shows the variation of FWHM of Mn Kα peak of the spectrum recorded by SCD with change in clock voltage, maintaining SCD at different temperatures. From figure 6.35, it was observed that, a clock voltage of 7.0 Volts and 5.0 volts when applied to CCD offers the least value of FWHM at -30 degree. The clock voltage has caused the formation of potential well required for charge collection and it has to have some trade-off with clock frequency and temperature. It was observed that, at 100 kHz, the transport velocity of the charges determined by the depth of potential well matches the time required for transfer of charges to neighboring pixel and collection of maximum charges in that pixel. In this case, minimum number charges that has been collected by the CCD is likely to be be spilled off, during the charge collection and transfer process. Hence, maximum resolution was obtained at that clock voltage, clock frequency and temperature. Fig 6.34 and 6.35 shows the variation of FWHM with clock voltages for the noise peak and the Kβ peak.

Figure 6.36 shows the variation of FWHM of the noise peak with clock frequency, at various temperatures. In Figure 6.36, the value of FWHM come down to 60 eV for -30 degree and for a clock voltage of 4.5 volts. Even though the results of zero peak does not represent the performance of the device as a

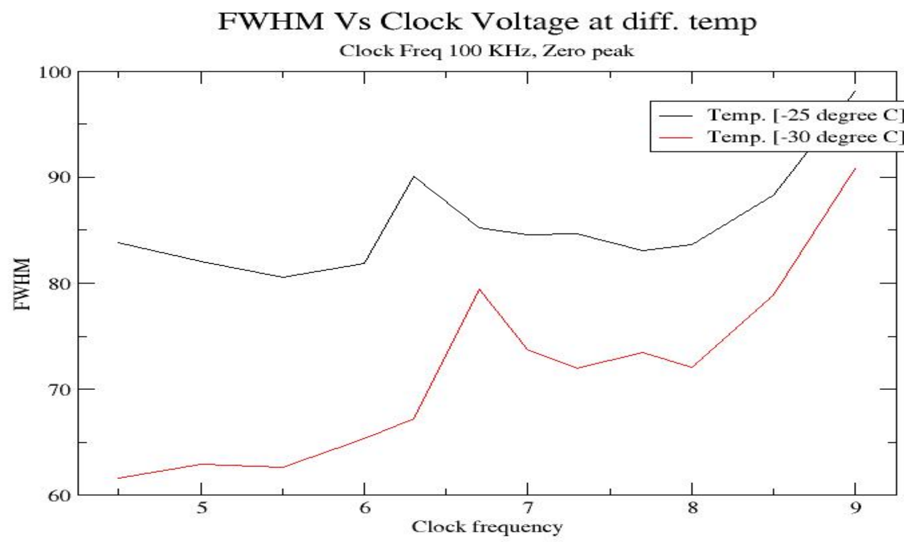

Figure 6.36: Noise peak : Variation of FWHM with clock voltage at different temperatures

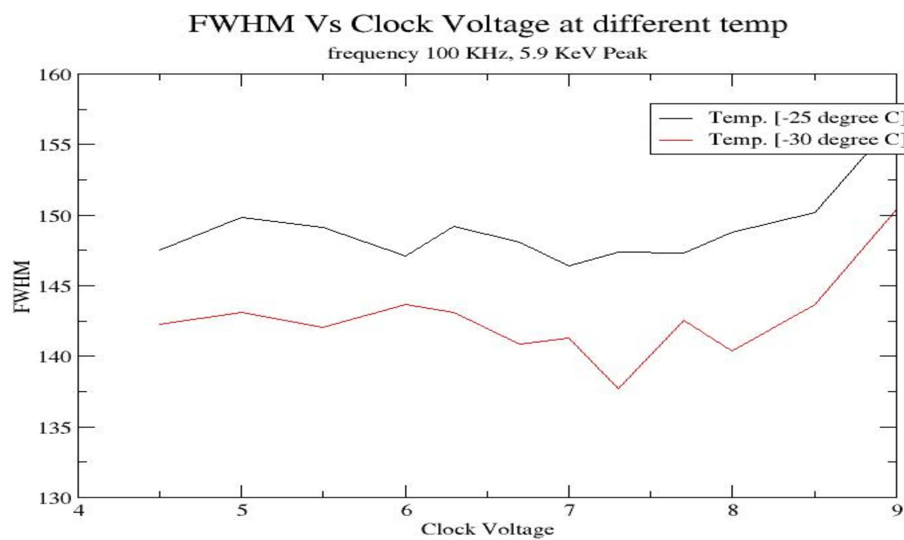

Figure 6.37: Mn Kβ peak : Variation of FWHM with clock voltage at different temperatures

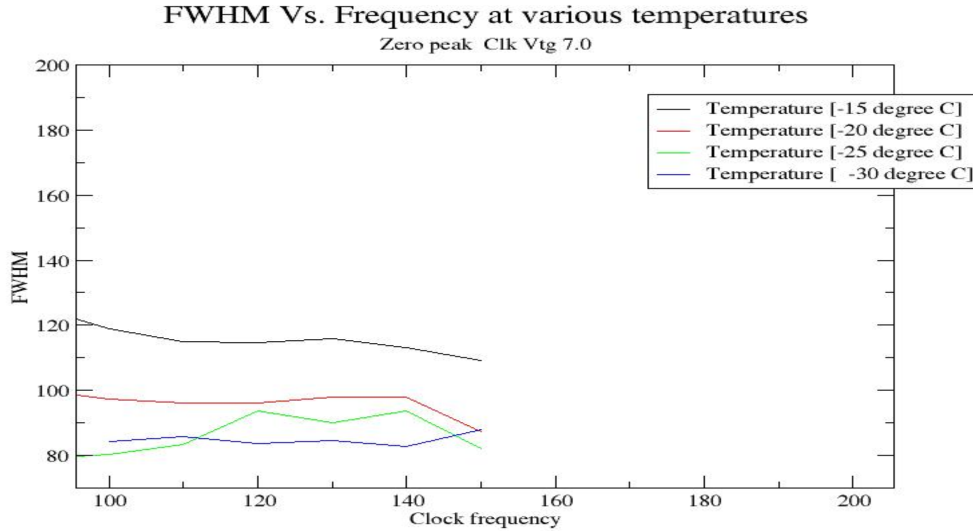

Figure 6.38: Noise peak - FWHM Vs, Clock Frequency at different temperatures

X-ray detector, it may be used for comparing the damage caused to the detector due to radiation.

Fig 6.37 shows the variation of FWHM with clock frequency at different temperatures for 5.9 keV line and figure 6.38 is the same study for 6.4 keV line. For 5.9 keV line and 6.4 keV line , the FWHM is the least(138 eV) at $\sim$ 7 volts when the temperature is 30 degree Celsius at a clock frequency near to 100 kHz.

Hence, clock voltage has been optimized at 7 Volts. Further studies were carried out to optimize the other parameters.

- SCD Pre-irradiation Analysis: FWHM Vs, Clock Frequency at different Temperatures:[Clock Voltage 7.0V]

figures 6.38 to 6.40, show the variation of FWHM with clock frequencies at a clock voltage of 7 volts. The curves were drawn for the temperatures -15, -20, -25 and -30 degree Celsius. We found that, at -30 degree C, the lowest value of FWHM of the device measured to be 140 eV at a frequency of 110 kHz. However, the required 150 eV resolution could be obtained even at 100 kHz. Hence 100 kHz is an optimum value of clock frequency to be chosen for the set standard resolution. In all cases, the temperature needed to be -30^oC to meet the resolution standard chosen. Hence, optimum operating temperature is -30^oC, Optimum operating Voltage is 7.0 Volts and Optimum Clock Frequency is 100 KHz.

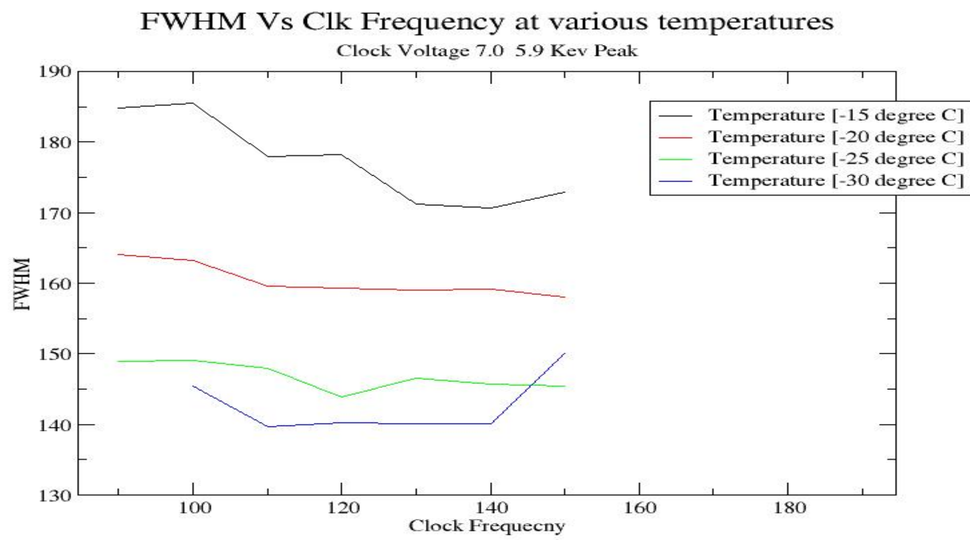

Figure 6.39: Mn Kα line - FWHM Vs, Clock Frequency at different temperatures

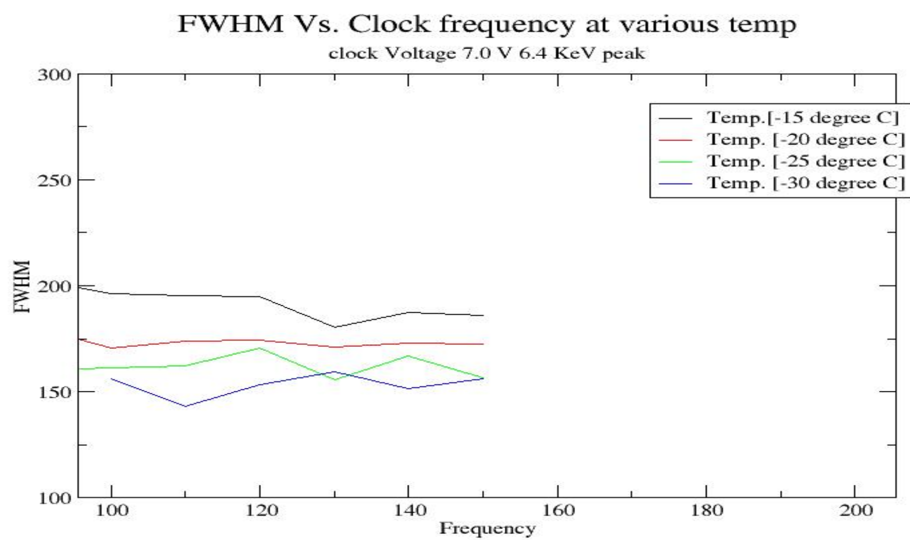

Figure 6.40: Mn Kβ line - FWHM Vs, Clock Frequency at different temperatures

6.5.3 Experimental study on the effect of proton irradiation on SCD

The optimization of CCD was done by determining the resolution of CCD in terms of FWHM for various parametric conditions. We chose values of different operating parameters in the possible range in actual application scenario and the best operating parameters were determined. The next step in the experiment was to irradiate the device with protons of suitable energy and fluence of interest. Calculation of the amount of proton radiation to which, the space vehicle will be exposed, is complicated. It depends on the vehicle trajectory, mission period, details of orbits round the earth and round the moon, mission date and solar cycle number. The previous data of the radiation studies over a wide period of time at various altitudes in the earth's magnetosphere and that of outer space have been modeled in SPENVIS software described in chapter 5. Hence, SPENVIS could be used to simulate the radiation environment of the space vehicle and to generate the detailed radiation data based on the actual mission plan. Since the mission plan was postponed, SPENVIS data from previous mission was chosen as the basis of determining the proton fluence required in the study. The proton fluence was, then, converted to equivalent fluence at 10 MeV. A detailed discussion on the experiment and its set up, based on the actual irradiation experiment at VECC , is given below.

- Study of the Irradiation Effect on CCD 236 X-ray Fluorescent detector Proposed to be Used in Chandrayan II Mission at ISRO.

Resolution of the device at various operating conditions was determined and the optimum operating parameters were fixed. The device was, then, taken to VECC Kolkata and then exposed to 10 MeV protons at a dose equivalent to that the device may be exposed in the space during the mission.

It was planned to find the performance degradation of the device during different stages of the mission period. The decrease in *Charge transfer efficiency*(CTE), *Flat band voltage shift* and increased *Dark current* etc. were the result observed in terms of shift in FWHM. Hence, the change in resolution due to irradiation was measured more directly by measuring FWHM of a known spectral line detected by SCD. The change in resolution of the spectral peak of Fe^{55} source detected by the device was measured at various operating conditions before and after irradiation.

Pre-Irradiation Study - Measurement setup

The details of experimental setup was the same as that used for the optimization study conducted earlier section. It consists of a source of X-ray, a vacuum pump connected to a vacuum chamber, a temperature controlling system with stability of 0.1 degree. The SCD driver electronics control CCD and provide an interface with XCAM software and SCD.

XCAM was set for sequence setting, voltage setting, delay setting etc. for SCD operation. In the experiment to study the dependence of temperature on FWHM, the sequential file, voltage file and delay were kept constant and the temperature was allowed to change by predetermined value. Since the read out electronics was also controlled by XCAM software, settings for read out parameters were also made in XCAM.

Only the top left quadrant of the device was exposed to the proton beam. Hence, the other part of the device was masked by an aluminum sheet of 1 mm thickness. When all the operating parameters were fixed, the system was switched on and waited for temperature to maintain constant value in the cold plate over which the SCD was fixed. When the temperature was steady at the fixed value data was captured by XCAM Software. The data was analyzed for split events as well as isolated events. The split events and isolated events were detected by the intensity of the pixel at that point. Using XCAM software, based on intensity, the data corresponding to isolated event alone was extracted and plotted against the channel number, which was, then, calibrated using known energy values of the Fe^{55} X-ray peak. The FWHM value of the spectral peaks was determined for zero peak, 5.9 KeV peak and 6.4 KeV peak. The experiment was repeated systematically for different values of temperature, clock frequency and clock voltage. A typical spectrum from Fe^{55} source keeping SCD at -20^oC and applying clock voltage pulse of 7.0 V at a frequency 100 kHz is shown in Figure 6.34, chapter 6. There are the noise peak, Mn-Kα peak and Mn-Kβ peak clearly visible in the figure mentioned. Other peaks are also present and become visible by magnifying the area of interest.

In the pre-irradiation analysis, the FWHM of the device was determined at different combination of device operating conditions such as sequence voltage, clock frequency and temperature. In the first part, the variation of FWHM with clock voltage was analyzed. For this study, the sequence voltage was varied from 4.5 volts to 9 volts in steps of 1 volt, 0.5 volts and 0.3 volts etc. (depending on the convergence towards optimum value). Fe^{55} spectrum was recorded at

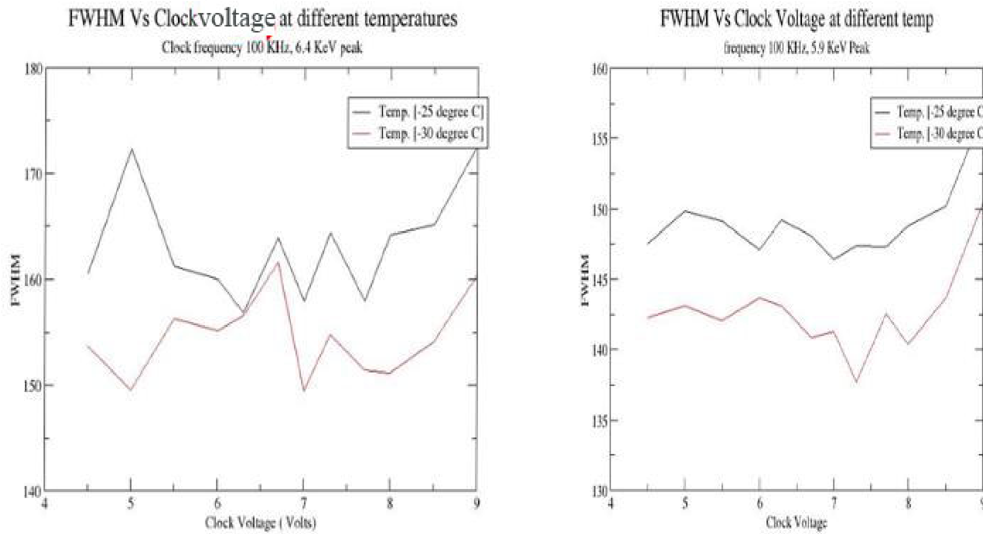

Figure 6.41: FWHM Vs clock voltage at different temperatures. For 5.9 keV peak and 6.4 keV peaks

each voltage at the same temperature. The spectrum was plotted using matlab code. It was, then, analyzed by the code written for determine the FWHM of the peaks as explained in the chapter 5. The FWHM was determined. The whole experiment was repeated varying the temperature. The temperature was varied from -35 to +5 ^{o}C in steps of 5 degree. Using the value of FWHM determined at each voltage and at each temperature , a plot was made to analyze the variation of FWHM at each voltage at different temperature. The whole analysis were repeated for zero peak, 5.9 keV peak and 6.4 keV peaks. The results were plotted in figures 6.35- 6.37. In Fig 6.41 it has been reproduced to maintain the continuity of discussion.

Even though, the variation of FWHM with clock voltage was not so smooth, both of the graph showed that FWHM was minimum near 7 Volts when the temperature of SCD was maintained at -30 degree. In both cases the clock frequency was set identical at 100 kHz.

To optimize the clock frequency for the operation of CCD, experiments were conducted to determine the FWHM of the spectral lines for various clock frequencies at different temperatures keeping the clock voltage constant at 7.0 volts in all the cases. The clock frequency was varied using XCAM Software. As before, the spectrum was recorded first from which FWHM was computed and plotted against frequency in figure 6.42. The figures showed that a clock frequency of 100 kHz was required to get the required performance of 150 eV resolution.

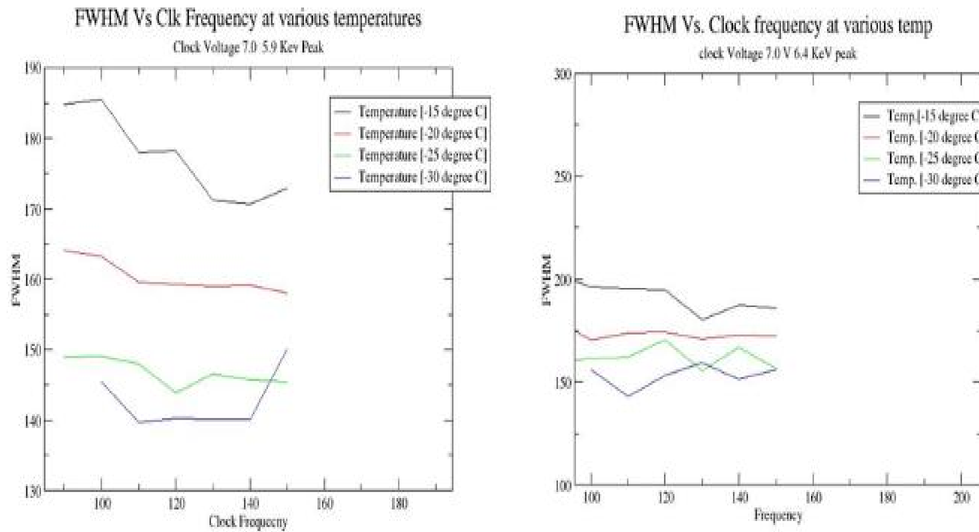

Figure 6.42: FWHM Vs clock frequency at different temperatures

Now, the experiment for the optimization of temperature was done. The above plots confirmed that, temperature should be maintained at -30 degree to get the desired performance . Hence, post irradiation experiments and comparison of pre and post irradiation results are mainly done by analyzing the performance of SCD at -25 to -35 degree.

The dark current of the device was also obtained at various temperatures. It was found that, FWHM vary with change in temperature, clock frequency and clock voltage set in the device. Optimum clock voltage and clock frequency were found to be 7.0 V and 100 kHz at temperature of -30 degree . Typical value of FWHM at the optimal parameters was found to be 150 eV.

Proton irradiation of the SCD device

For irradiation of the device with 10 MeV proton, the device was taken to Variable Energy Cyclotron Centre at Kolkatta. Only one quadrant of the device was irradiated. To mask the other quadrants and to hold the device facing the proton beam line a *Jig* was designed. The jig was made using stainless steel of thickness 5 mm . The jig can hold the device without shorting the pin-outs of the device. The masks were made using 1 mm aluminium sheet. The masks could be slide in to the jig, so that, the wire cut window of size 1.07 cm^2 exposes one quadrant of CCD to the proton beam. Due to the symmetrical layout of the SCD, only two masks were enough to choose any of the four quadrants to expose. A focused proton beam with cross sectional diameter 0.6 cm was

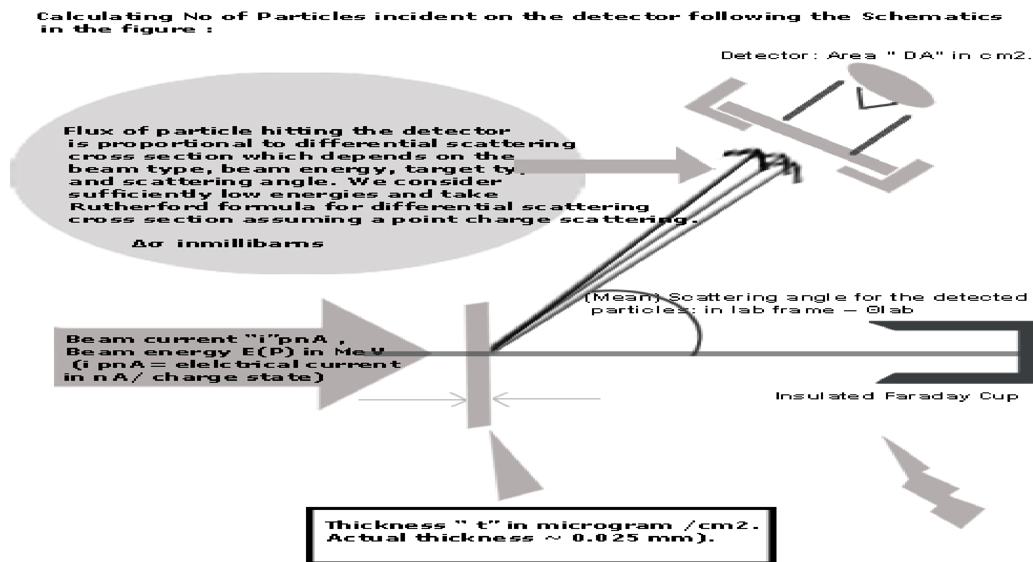

Figure 6.43: Rutherford Scattering Setup for irradiation of SCD

scattered using tantalum metal and the scattered beam was made to fall on the exposed part of CCD and ensured that, the number of protons passing through the window and falling on the CCD could be calculated exactly during experiment. The experiment was arranged to hit the top left quadrant of the CCD with a total number of 2 X 10^8 protons. It require a very small flux of protons to last the irradiation period over convenient time to conduct the experiment. So, the beam current has to be very small. Production and tuning of such a small beam current has very many practical difficulties beyond the control of the systems and set up in the cyclotron. In order to reduce the beam current to the desired low level of flux, Rutherford scattered component of the beam was used. Rutherford scattering formula was used for the calculation of the number of protons passing through a solid angle $d\omega$ at an angle $d\theta$. This has ensured the distribution of flux over a wider range of time (Typically 6 Hrs) for the desired fluence and to have a better control of beam stability. A Rutherford Scattering Setup as in figure (6.43) was arranged to the scatter the beam by a suitable target.

The Rutherford Scattering Chamber has approximately 90 cm diameter. Three quadrants of the device, except the top left quadrant, were masked by aluminum sheet of thickness 1 mm. and housed in a jig. The jig was mounted on a stand suitably fabricated to fix on one of the flanges provided inside the irradiation chamber. It was fixed at angle of 20 degree. A CsI scintillation detector was housed in a metallic box provided with a Window of 2 mm diameter. It was mounted on the other flange provided in the opposite direction. CsI detector was used to count the number of particle falling at an angle 40 degree after the

scattering. Tantalum was used as the target and fixed normally to the beam direction.

In order to verify the counts in the CsI monitor, a Faraday cup was arranged in the direction of the beam line to count the actual number of particle passing through the target without deviation. The counts in the Faraday cup were approximately equal to the number of particles incident on the target.

The beam was made to the desired size with the help of an Alumina beam viewer. The beam was tuned to obtain 10 MeV protons. SCD was kept at angle of 20 degree. The beam current was fixed to be 2.5 pnA. ie, (1.5 X 10^{10}, particles/second). The fraction of particle hitting the CsI detector at 40 degree was calculated.

The counts due to the radiation falling on the CsI detector was obtained after few minutes. This histogram is expected to be a normal Gaussian. When plotted, it was found that, in addition to the Gaussian peak, a back ground also appeared. From the Gaussian peak, (assuming normal distribution), the area was determined by the system which gave the exact count rate in accordance with calculation. Since, the observation agrees with calculation, the number of protons hitting the CCD at an angle 20 degree per second was also determined by calculation.

Details of calculation - Rutherford setup

The Rutherford scattering chamber has a dimension of approximately 90 cms radius. It has two mounting flanges inside which was slotted along the radial direction at various distance from the target position at the centre. Slots were provide for the positioning of the detector. The flange could be rotated by an automated control for the required angle between the target and the detector. The chamber could be evacuated by a diffusion pump to keep the pressure inside to be at 10^{-5} milli-bar. No. of particle hitting per second,

$$N = (3.76/A_T) * (\Delta\sigma) * (t) * (i) \tag{6.19}$$

Here , t and i are as defined in the figure 41. A_T is the atomic mass of the target. $\Delta\sigma$ is the cross section seen by the detector and is by :

$$\Delta\sigma = \frac{d\sigma}{d\omega} * \Delta\omega \tag{6.20}$$

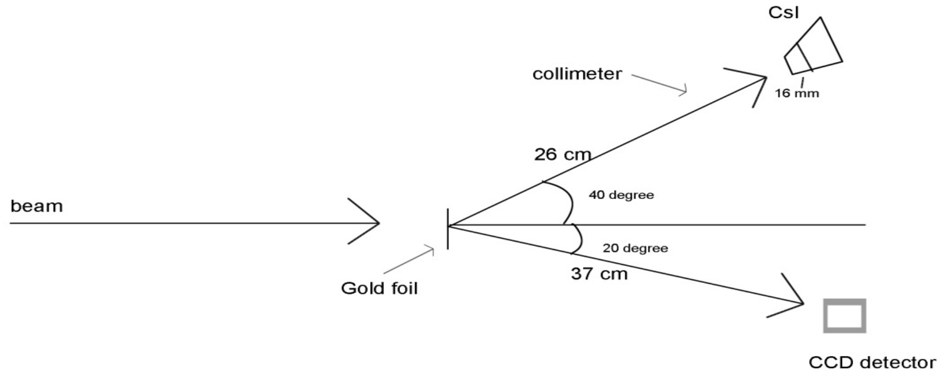

Figure 6.44: SRIM simulation showing 1 MeV proton trajectories in CCD 236

with the first term being the differential scattering cross section per unit solid angle and the second term is the solid angle subtended by the detector, approximately given as $\Delta\omega = D_A/d^2$. The expression for $d\sigma/d\omega$ is as below.

$$d\sigma/d\omega = 1.39 * [Z_P * Z_T/E_P]^2[sin(\Theta_{LAB}/2.0)]^{-4} millibarns/steradian. \quad (6.21)$$

Z_P and Z_T being the atomic numbers of the beam and the target. CCD is kept at 20 degree and the detector at the angle 40 degree on the other side. The detector and CCD were fixed in the collimator as shown in the figure (6.43).

Taking t = 250 microgram / cm^2, i= 5pnA , E_P = 10 MeV, Z_P = 1, Z_T =79 (for Gold target) ,A_T = 197, Θ_{LAB} = 40 degrees,

Value of $d\sigma/d\omega = 1.39 * (1 * 79/10)^2 * [sin(40/2)]^-4 = 6338.815193$.

With $\Delta\omega$ = 4.645X10-5, we get $\Delta\sigma$ = 0.29443

The no of particle hitting per second was calculated using the formula (19) above, we got it to be 7.02 counts /second.

The number of particle falling per second in the detector was verified and found to be 7 counts per second. This observation has assured that, the determination of the number of particles falling on the CCD was fairly accurate.

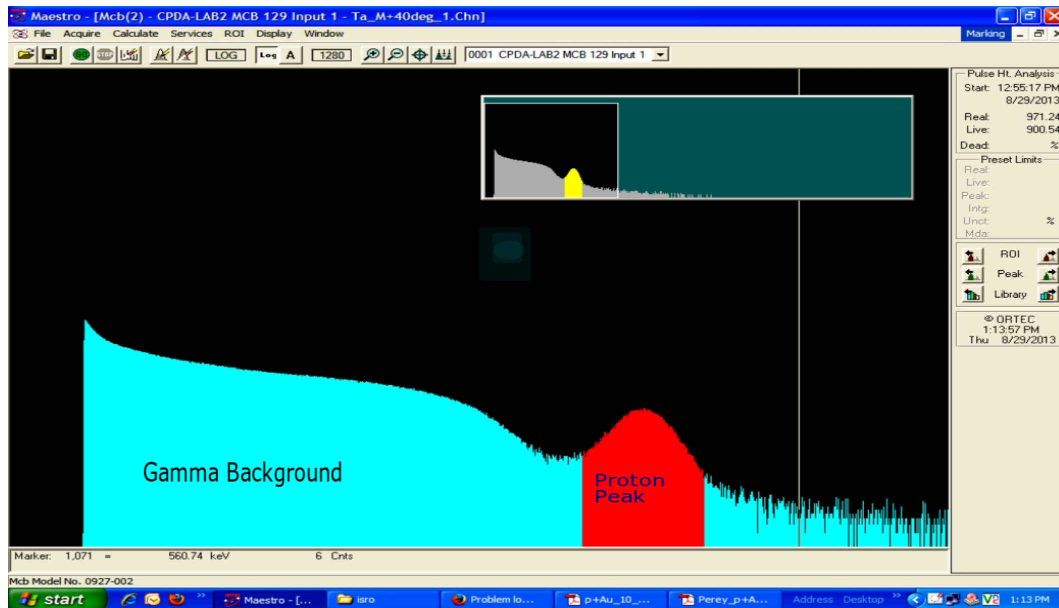

Figure 6.45: Histogram showing proton peak and background gamma rays

Analysis of the spectrum and calculation of exposure time

To estimate the fluctuation of the proton counts at 10 MeV, CCD was brought at 90 degree position and CsI monitor was brought to 20 degree. It was found that, at 20 degree the beam was stable with expected counts. Above 30 degree, the beam showed a small fluctuation from the expected count, limited to statistical error. CCD and monitor were brought back to their positions to continue the experiment.

The exposure time required to hit the CCD by $2X10^8$ numbers of protons was calculated observing the counts obtained from Farady cup as well as that from CsI detector. Both calculations agreed that, CCD kept at angle of 20 degree require 6 hrs 38', 25" to hit with $2X10^8$ particles when the beam current is 2.5 pnA. The integrated charge collected in the Farady cup and the integrated counts expected in the detector at 40 degree during the calculated exposure time were also calculated. These figures were observed to be in good agreement at the end of the calculated exposure time (6 hrs 38 minutes, 25 seconds).

Figure (6.44) is a histogram of the spectrum obtained in the experiment drawn using Maestro Software tool. The red peak is the proton peak. The total number of particle hitting the detector was determined from the area under the peak

The spectrum was analyzed using a *Pulse Shape Discriminator* set up. The analysis using PSD confirmed that, the background is due to gamma rays.

However, the analysis could not reveal the source of gamma rays.

The counts in the monitor and the Faraday cup were continuously monitored, and found to follow calculations done during exposure in every hour. This has shown that, the beam current were more or less steady during the exposure at 2.5 pnA.

The error associated with positioning of CCD at angle at 20 degree was also estimated for 0.05 degree deviation at 20 degree basing the least count of the angle measurement. This error was found to be within statistical limits of the counts observed. The final number of particles that hit the CCD during the experiment was recorded to be $2.155X10^8$.

Two hours, after irradiation, the CCD with its jig was removed from the chamber and verified that, there was no residual radioactive emission from them. After 3 days the device was analyzed for the performance degradation at ISRO with the same experimental setup used for the pre-irradiation study.

A comparison of the pre-irradiation and post irradiation analysis of the device performance, by comparing FWHM of the spectral peaks of Mn-Kα and Mn-Kβ from Fe^{55} source, it was found that, there was considerable degradation of performance of the device. FWHM has gone up from a pre-irradiation average of 150 eV to nearly 350 eV at -30 degree after irradiation of the top left quadrant when irradiated with $2.1X10^8$ protons.

Results of experiment

.

As in the case of pre-irradiation experiment, the device was mounted in the vacuum chamber and exposed to radiation from Fe^{55} source. The spectrum was plotted from the data obtained using the irradiated CCD. Using the same matlab code used for the pre-irradiation study, the FWHM was determined at various operating conditions particularly converging to the optimum operating conditions. The FWHM obtained in case was tabulated and plotted against the variation of clock voltage, variation of frequency and that of temperature etc. through figures (6.45) to (6.54) along with the pre-irradiated data.

- Repetition of Proton Radiation Damage Experiment Using CCD 2. Irradiated at TIFR

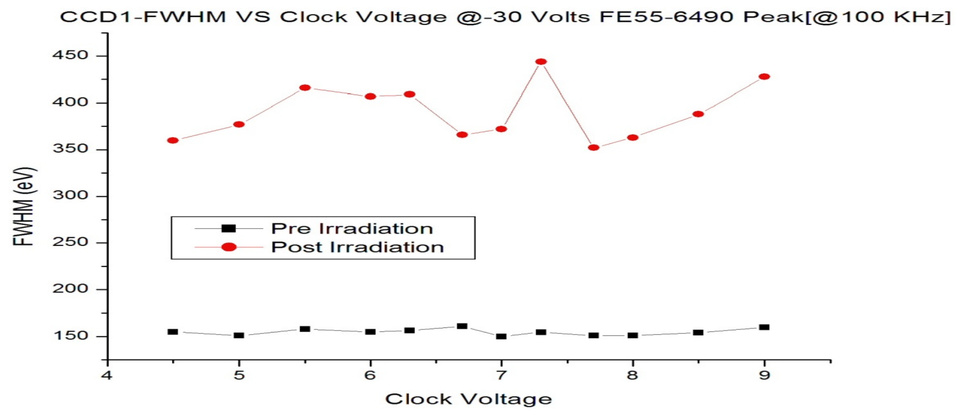

Figure 6.46: Variation of FWHM with clock voltage of CCD of the Mn Kβ line of Fe^{55} spectrum, at 100 kHz and -30° C; Comparison of pre and post irradiation performance.

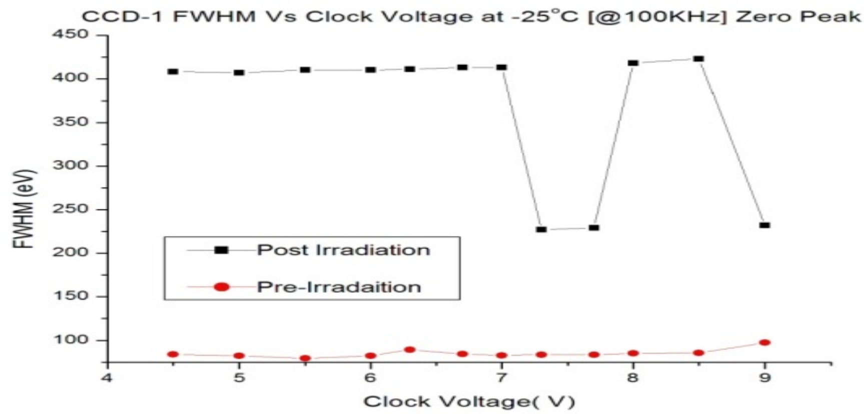

Figure 6.47: Variation of FWHM with clock voltage of CCD of the noise peak in the spectrum, at 100 kHz and -25° C; Comparison of pre and post irradiation performance.

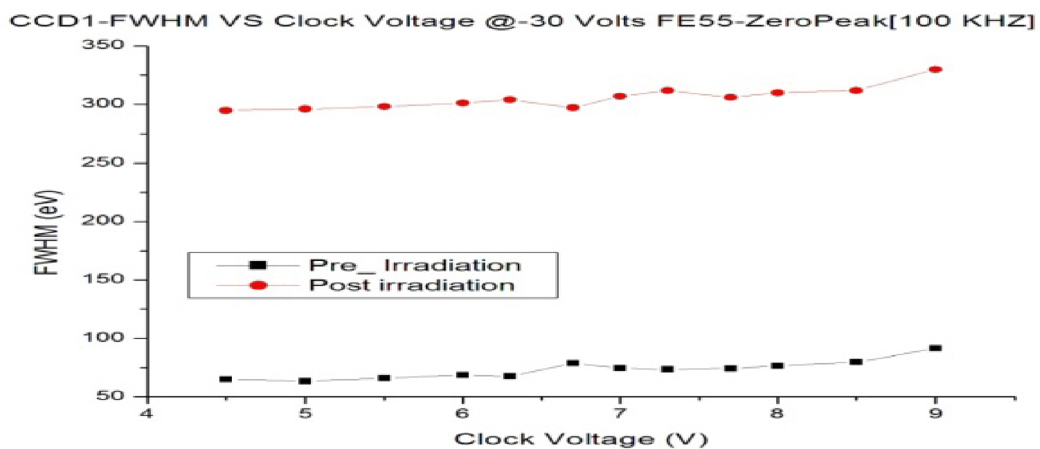

Figure 6.48: Variation of FWHM with clock voltage of CCD of the noise peak in the spectrum, at 100 kHz and -30° C; Comparison of pre and post irradiation performance.

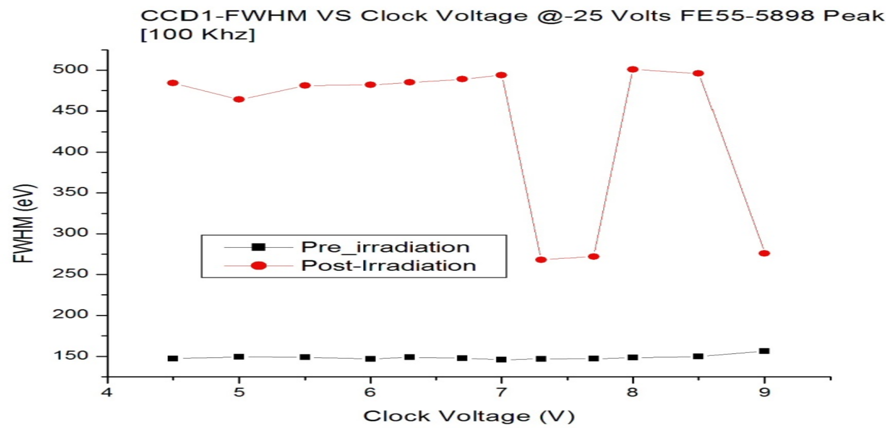

Figure 6.49: Variation of FWHM with clock voltage of CCD of the Mn Kα line of Fe^{55} spectrum, at 100 kHz and -25° C; Comparison of pre and post irradiation performance.

Since, there was a large deviation in the post irradiation performance with that of pre-irradiation performance, the experiment was repeated with a clone of the same CCD. The pre-irradiation study was performed as before using CCD 2. The pre-irradiation characteristics of CCD-2 was found to match exactly with that of CCD-1 except for the noise peak for which, there was a fixed offset for the variation of FWHM with temperature as depicted in Figure 6.53. Then, the device was, then, taken to Pallatron Center at Tata Institute of Fundamental Research, Bombay for irradiation . The CCD was, then, irradiated with 10 MeV proton at a fluence of 0.5 X 10^8 , over an area of 4 cm^2 of CCD 2 so that, the damage effect to this CCD was the same as that given for CCD-1

Details of the experiment

The experimental set up were the same as used for CCD 1. A vaccum chamber was used for Rutherford scattering using gold foil. After irradiation, the device was brought back to ISRO Bangalore for measurements. The same set up used for the pre-irradiation study was used for post irradiation measurements. As before FWHM of Fe^{55} spectral lines were measured with the help of experimental setup for different values of sequence voltage, frequency and temperature. The measurements were tabulated. The variation of FWHM with the above operating parameters were plotted along with the results obtained in the pre-irradiation analysis.

The results once again confirmed the large variation of CCD characteristics between pre-irradiation and post irradiation measuremetns.

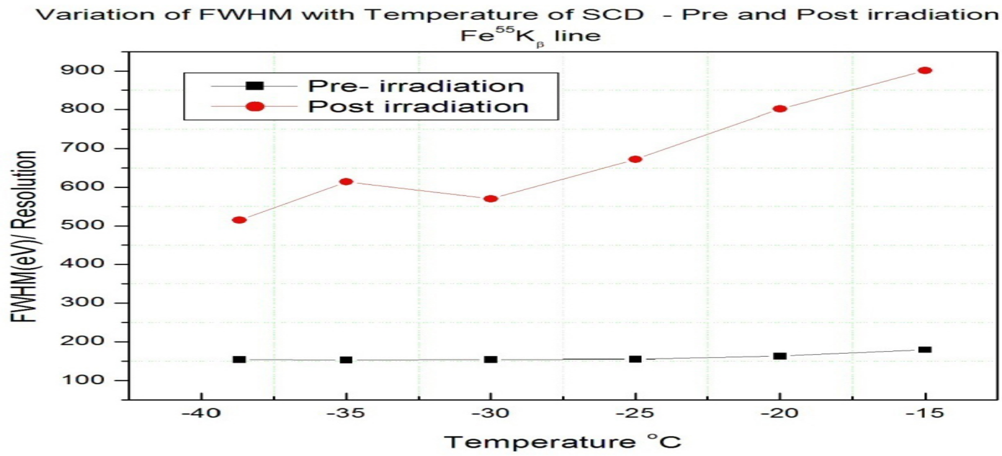

Figure 6.50: CCD 1: Variation of FWHM with temperature of CCD for the Mn Kβ line of Fe^{55} spectrum, at 100 kHz and 7.0 Volts; Comparison of pre and post irradiation performance.

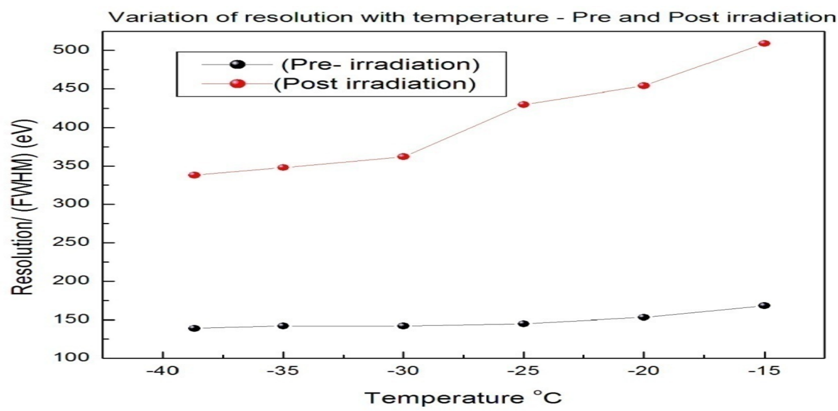

Figure 6.51: CCD 1: Variation of FWHM with temperature of CCD for the Mn Kα line of Fe^{55} spectrum, at 100 kHz and 7.0 Volts; Comparison of pre and post irradiation performance.

Result of irradiation for CCD 2 Comparison of results before and after irradiation

Post-irradiation results show that at -30 degree the post irradiation performance of CCD 2 was different from the post irradiation performance of CCD 1. There was a large deviation.

Comparison of the variation of performance of two CCDs after irradiation

- Comparison of CCDs: Variation of performance with temperature before and after irradiation

Resolution study of CCD 1 and CCD 2 was depicted in figure 6.53 before irradiation. The same CCD was analysed for the change of resolution after

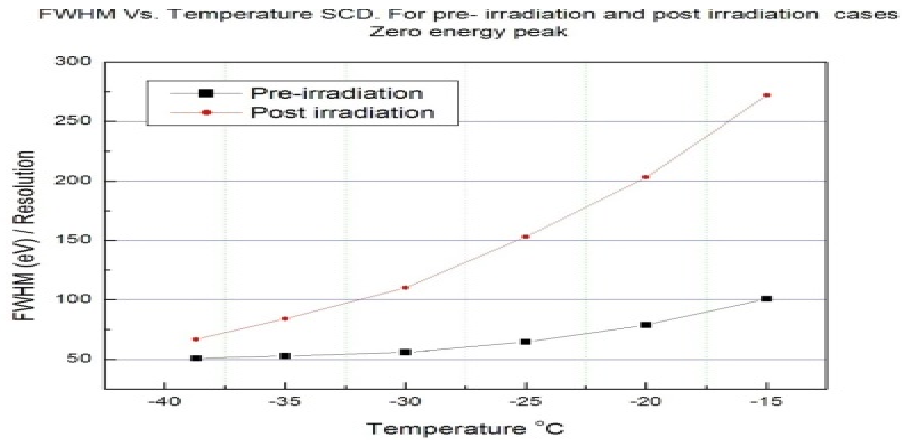

Figure 6.52: CCD 1: Variation of FWHM with temperature of CCD for the zero energy peak of Fe^{55} spectrum, at 100 kHz and 7.0 Volts; Comparison of pre and post irradiation performance.

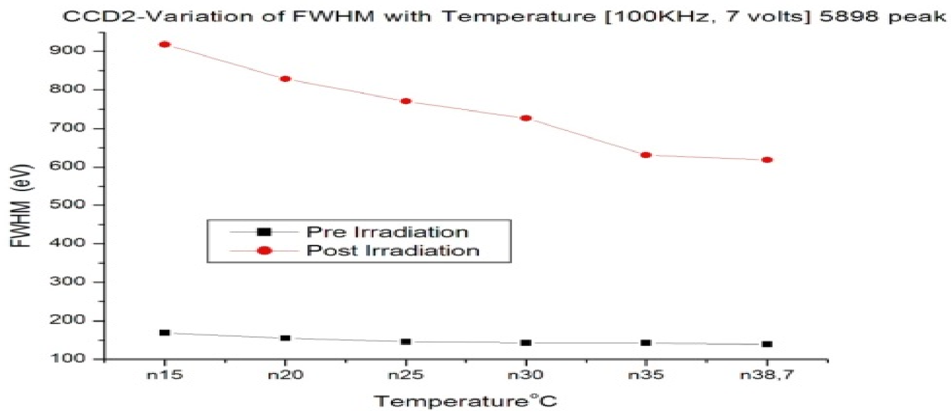

Figure 6.53: CCD 2: Variation of FWHM with temperature of CCD for the Mn Kα line of Fe^{55} spectrum, at 100 kHz and 7.0 Volts; Comparison of pre and post irradiation performance.

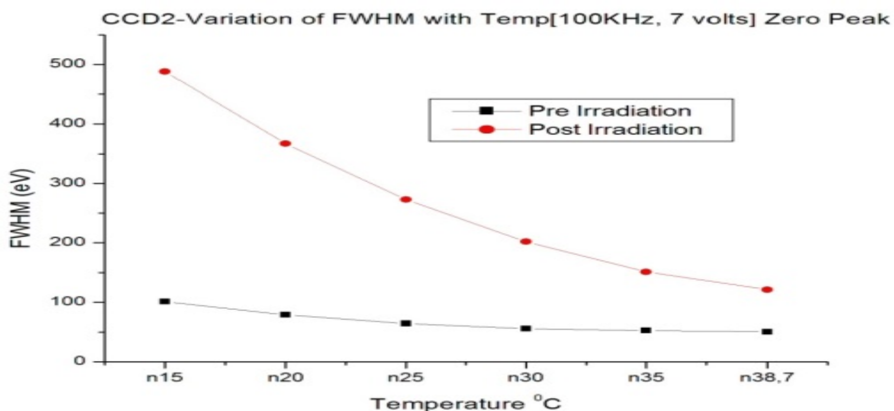

Figure 6.54: CCD 2: Variation of FWHM with temperature of CCD for zero energy peak of Fe^{55} spectrum, at 100 kHz and 7.0 Volts; Comparison of pre and post irradiation performance.

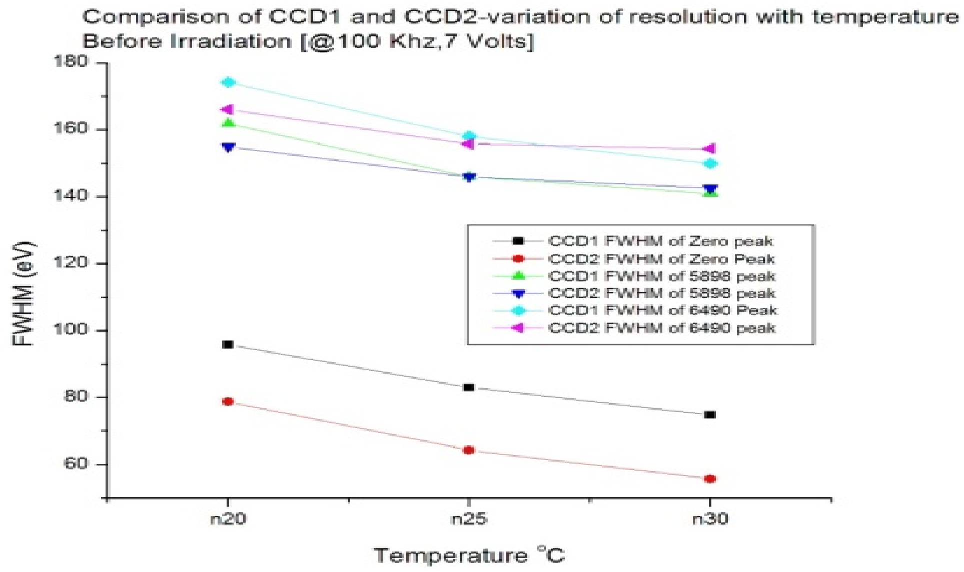

Figure 6.55: Comparison of CCDs: Variation of the post irradiation performance with temperature in two CCDs

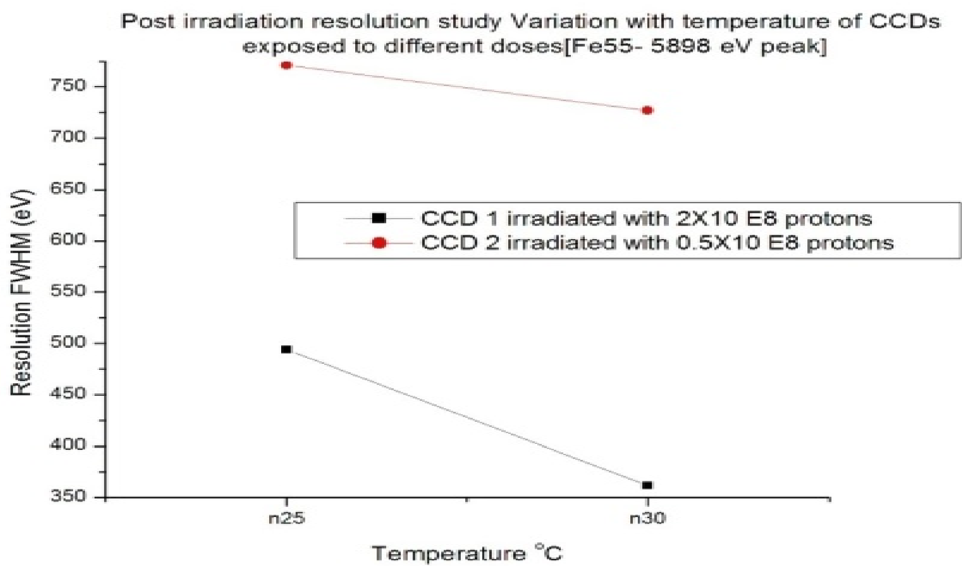

Figure 6.56: Post irradiation comparison of CCDs: Variation of post irradiation performance with temperatures - (Mn Kαline) of Fe^{55} spectrum

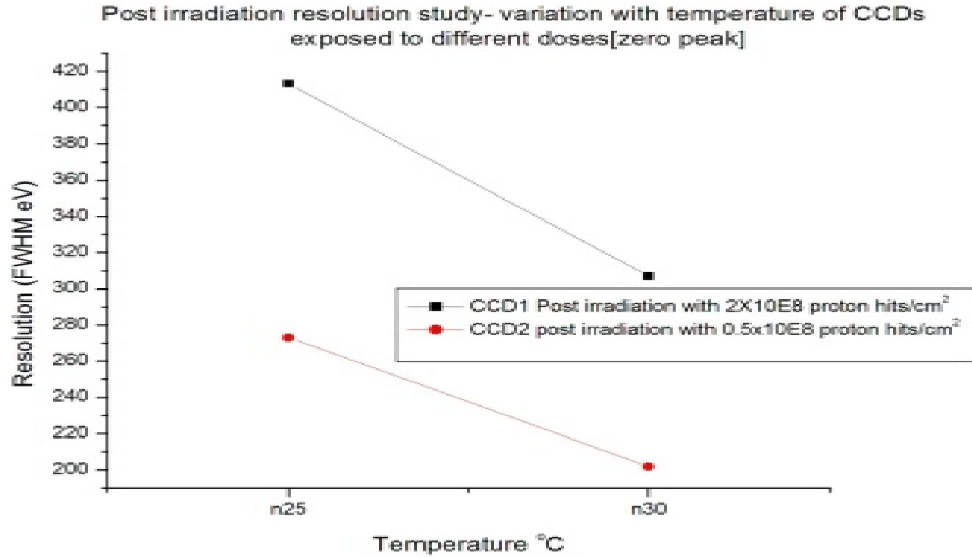

Figure 6.57: Post irradiation comparison of CCDs: Variation of post irradiation performance with temperatures - Zero peak of Fe^{55} spectrum

irradiation and depicted in fig 7.55 and 7.56. It was very difficult to measure the resolution at temperatures above -20 degree. Hence, after irradiation the resolution could be determined only at -25 and -30 degree. Since the operation of CCD in the space is optimized at -30 degree,the observation at -20 degree is not significant.

The FWHM value increased considerably after irradiation. CCD2 recorded more damage than CCD 1. Only one quadrant of CCD 1 was irradiated with a flux of 2 X 10^8 protons while the entire surface consisting of four quadrants and the electronics channel area was exposed with a flux of 0.5 X 10^8 protons. The area integrated dose being the same. Still CCD 2 recorded a high change in resolution with respect to CCD 1. This shows that, the exposure in the electronics area, described in chapter 5 section 4, could deteriorate the CCD performance to a considerable extend.

6.5.4 Room temperature annealing of CCD irradiated by protons at high doses

The next step in the study was to observe the self annealing process in the CCD to see the possible recovery of damages caused to CCD over a period of time. It was decided to study the self annealing behavior of the CCD to see the possible recovery of resolution change over a period of time. So, the observation was continued on the CCDs to study on the effect of room temperature annealing

of CCD 226 following irradiation. The measurement of the improvement in resolution of the device was taken as the measure of annealing effect of CCD. Hence, measurement of (FWHM) were carried out (i) immediately and (ii) after twelve months and(iii) after 20 months since irradiation.

The study has provided some insight in to room temperature annealing effects of CCD as against the previous observation that, room temperature annealing was insignificant [18][19]. Laboratory dose rate are relatively large so that, years of in-flight damage accumulation could be produced in a reasonable period of time [19]. This method does not consider self annealing process in CCDs over the years of mission period.

Even though the room temperature annealing itself was not a method to anneal the device onboard in the space vehicle, the data will help in understanding the mechanism behind the RT annealing.

In order to determine the performance of CCD immediately after irradiation with protons and that after a long annealing period, the FWHM of characteristic X-ray peaks emitted by Fe^{55} radioactive source was taken as a benchmark. Since, the resolution was highly dependent on the device temperature, (see, figure 6.56 and 6.57), clock frequency and clock voltage, there is a need for optimizing these parameters for the desired performance measurement.

The results of optimization study of CCDs before irradiation was used to fix up the operating conditions. CCD was irradiated by 10 MeV protons with a fluence of $2X10^8$. The result of analysis of CCD immediately after irradiation as well that after at later periods were made use in studying the self annealing behavior of CCDs. CCD was first analyzed immediately after irradiation, then, after storing the device for a period of 12 months and finally after a period of 20 months storage at room temperature. The performance change was recorded in terms of the change in FWHM, which is tabulated.

Figure (6.57) depicts the variation of resolution with temperature of the CCDs before irradiation and that after irradiation. After irradiation the resolution of the CCDs exhibit larger sensitivity to temperature.

Figure (7.58) shows the resolution (FWHM) after 12 months of RT annealing from the date of irradiation and figure (7.59) shows the same after 20 months of RT annealing along with its value before irradiation and that immediately after irradiation. The FWHM of Mn Kα peak of Fe^{55} recorded at the temperatures of -25^oC and -30^oC alone are shown. Above -25^oC it was not

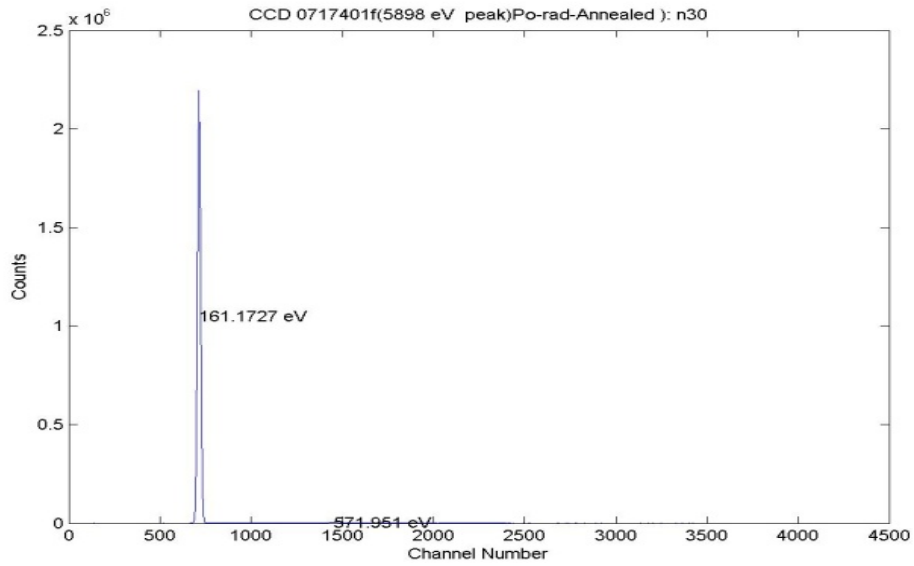

Figure 6.58: Fe^{55} Spectrum recorded using an irradiated CCD - Mn Kα and Mn Kβ peaks are seen- measured 12 months after irradiation - at -30° C

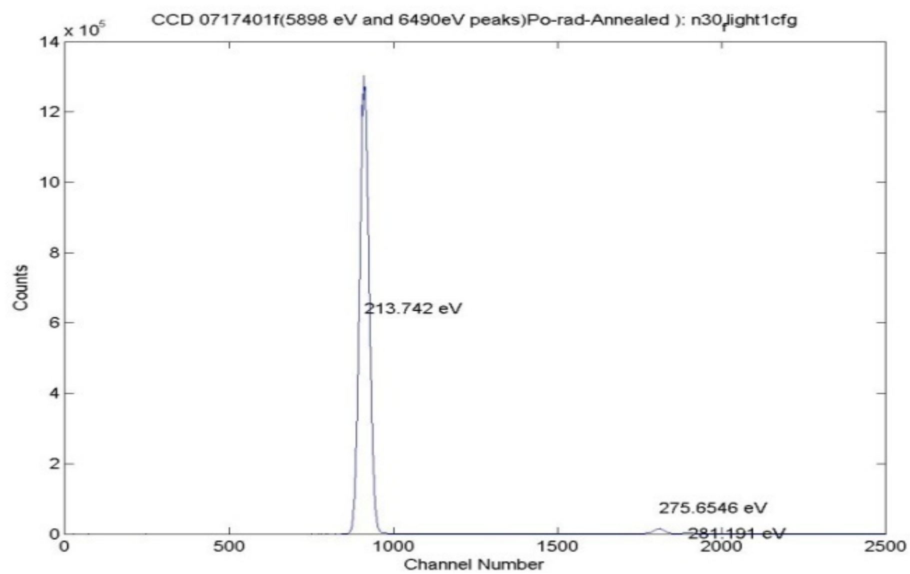

Figure 6.59: Fe^{55} Spectrum recorded using an irradiated CCD - Mn Kα and Mn Kβ peaks are seen- measured 20 months after irradiation - at -30° C

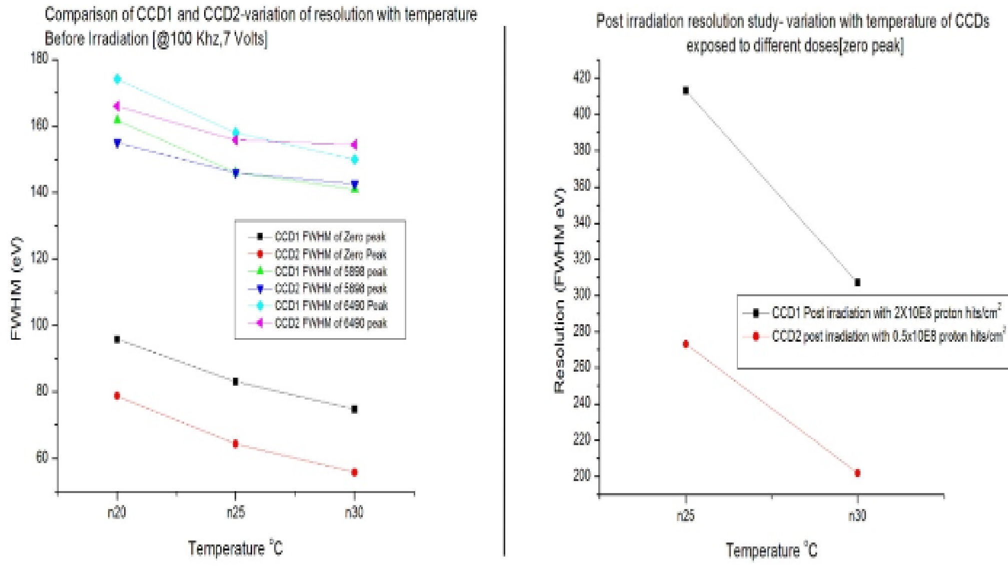

Figure 6.60: Figures depicts the dependence of resolution of the devices on temperature before and after irradiation

possible to measure FWHM for the irradiated CCDs. Hence, a comparison at temperatures above -25^oC was not possible. Since, the resolution is highly dependent on temperature, as evident from (7.60) the comparison of FWHM before irradiation, after irradiation and after annealing were made at respective temperatures.

Table 6.5: CCD irradiation data-pre and post irradiation, post annealing

	CCD-1	
	Temperature	FWHM (eV)
Pre-irradiation	-20^oC	161
	-25^oC	146
	-30^oC	141
Post irradiation	-20^oC	——
	-25^oC	494
	-30^oC	362
Post Annealling	12 months of annealing	
	-25^oC	615
	-30^oC	572
	20 months of annealing	
	-25^oC	354
	-30^oC	276
$\triangle FWHM$ (-30^oC)	Between Pre-irradiation and Post irradiation	
	-25^oC	348
	-30^oC	221
	Between post radiation and post annealing	
	-25^oC	140
	-30^oC	86

After prolonged room temperature storage, both the devices recorded an improvement on resolution which is an indication to room temperature annealing.

Comparison of device performance pre-irradiation, post irradiation and post annealing is shown Figure (6.59)

Table 6.6: CCD annealing data-in different annealing period

Annealing period	Temperature	Δ FWHM post radiation	Δ FWHM post anneal	Ratio %
12 months	-25	156	625	25
	-30	155	585	26
20 months	-25	140	348	40
	-30	86	221	39

The performance of CCD in terms of FWHM was tabulated for its values before irradiation and after irradiation at different temperatures in Table 6.5. It shows the change in resolution (ΔFWHM) (1) due to irradiation and (2) that due to room temperature annealing. In Table 6.6, the improvement of resolution ΔFWHM due to self annealing is presented in percentage as the ratio between the *change in resolution due to annealing* and the *change in resolution due to irradiation.* The effect of annealing on FWHM and its effect on annealing time are demonstrated in Figure (6.61). At -30°C, The ΔFWHM value was decreased by 26% after room temperature storage for a period of 12 months and 39% after 20 months of RT storage, from their respective values immediately after irradiation. The observed variation in ΔFWHM at two different temperatures are shown in Figure (6.62).

Hence, it was concluded that, at room temperature, the improvement in resolution due to annealing has a direct dependence on annealing time. It may be possible to create a look up table for annealing data, if several measurements are done. With a proper Interpolation of annealing data it may be possible to predict the annealing caused CCD over any period of time.

This fact could be established only if more studies were done over a longer period . Since there was limitation of time to conduct such study, the analysis was made only with available data. The time dependance of self annealing process has to be studied in future. The data will help in better modeling of radiation damage to CCDs. It is important that, self annealing process is always present in CCDs during its exposure to radiation in the mission period. Hence, ground studies with CCD prototypes need a self annealing correction, which could be predicted for the period mission. This also has to be carried out as a future work.

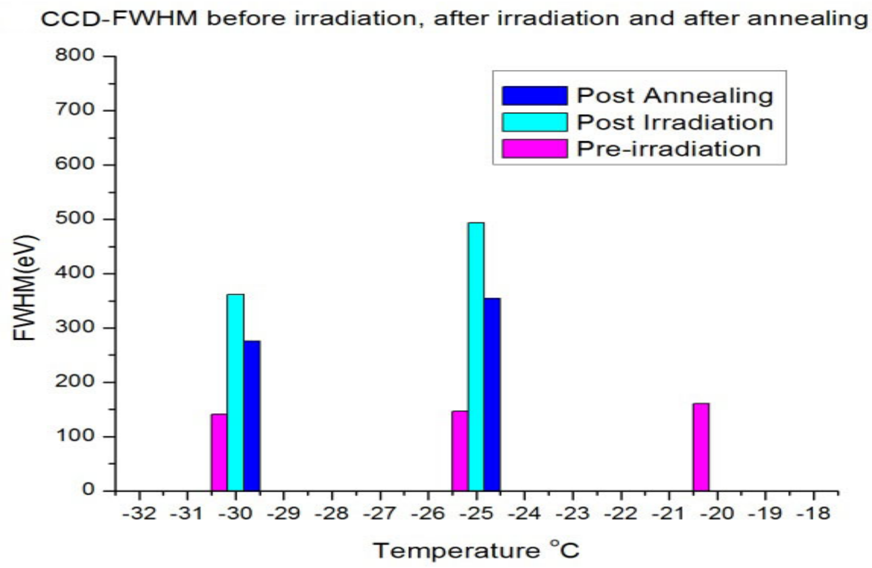

Figure 6.61: Comparison of device performance pre-irradiation, post irradiation and post annealing

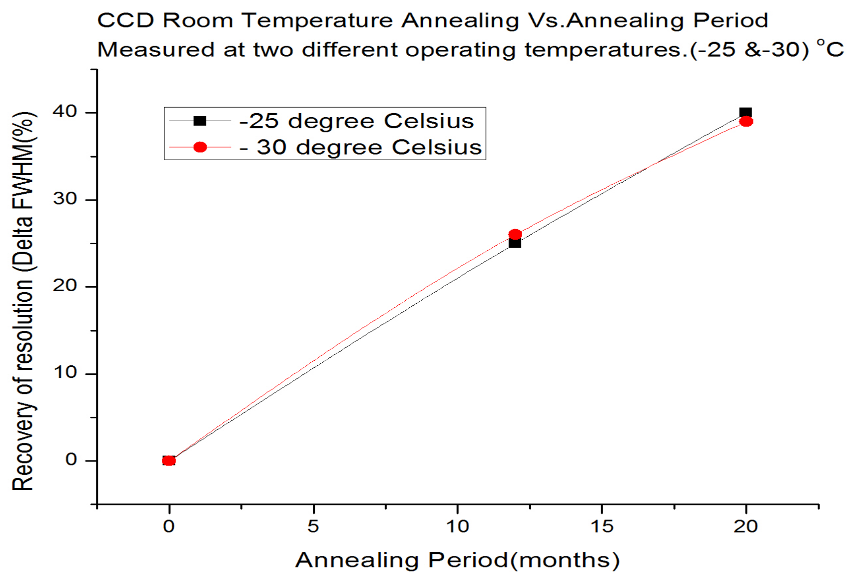

Figure 6.62: Variation in the measurement of ΔFWHM at two different temperatures.

6.6 Conclusion

The study of the effect of radiation on electronic devices was done on discrete devices- p-n junction, zener diode and transistors- as well as on the state of the art complex devices-CCD 236 X-ray fluorescence detector system. Remarkable change in performance characteristics were observed. In the off-line study with p-n junction, it was observed that, the change in variation of energy of radiation has little dependence with regard to observed effect, while change in dose has remarkable effect. Further, a kind of annealing effect was found, at higher doses. This observation is true with electron radiation as well as photon radiation. Hence, it is concluded that, the energy deposition mechanism is identical for both electron irradiation and photon irradiation. The annealing effect observed at higher doses may be due to the heating effect of the interaction of radiation with matter. The heat so generated will reverse the effect of radiation. Zener diodes are found to be more sensitive to than that of p-n junction. This may be due to the reason that, the base region is very thin in the case of zener diode. The change in the reverse biased characteristics of zener diode is interesting. The break down voltage of zener diode is found to increase after irradiation with electron as well as photons. The reverse break down become more rapid and approaches the ideal characteristics. The device simultaneously gets radiation hardened and improvement in the characteristics with a shift in the value of breakdown voltage. This situation can be made use in manufacturing zener diodes with improved characteristics. In the offline study using transistors, irradiation of the device has caused degradation in transistors. It could be concluded that, the exposure of BJTs to Bremsstrahlung photons or electrons has caused radiation damage leading to a decrease in the current gain of the BJTs.

In the online study of the transistor characteristics change during the irradiation. Contrary to the observation for offline analysis, the observed effect of shift in the collector is significant for varying energies where as variation in dose or dose rate has no remarkable effect on the collector current. The Random Telegraph Signals observed in the output characteristics as attributed to the selective trapping and release of carriers in the radiation induced trap centers in the band gap region of semiconductor. The relaxation time of various trap centers are related by an exponential autocorrelation function. The power spectrum of such noise signals is similar to 1/f noise. This has significant effect on data recorded and transferred by the device. Recent publications in this area [20]-[24] are supportive to the findings.

On exposure of the SCD to proton beam of 10 MeV at a fluence of 10^8 causes deterioration in performance parameters of the device with a shift in flat band, increase in dark current and worsening of resolution. Exposure of electronic channel of the device is found to be more lethal to the device than exposing of sensitive detector area to the radiation. The device performance has shown remarkable improvement on room temperature annealing over a period and found to depend directly on duration of self-annealing. This is important as the rate of exposure of the device to the space radiation is relatively small, compared to the experimental time scale, there is better possibility, at least partial, of self-annealing of the device during the mission period itself. More systematic and measurements repeated in short and long intervals and exposure to varying dose of radiation are to be carried out to have a strong database for such studies thereby the effects produced on each device is precisely predicted. This will form the substance of future work.

Bibliography

[1] Gnana prakash AP. Ke Sc. And Siddappa. K. Swift Heavy ion effects on electrical and defect properties of NPN transistors. Semiconductor sci. and Tech., Vol.19, 1029-1039,2004.

[2] Issim M Najim; Studying the effect of Xray radiation on the electrical properties of Diode IN 1405'. Intl. Journal of Nano Electronics and material; pp 35-39; 2008.

[3] Space radiation effects on electronic components in Low earth orbit; Preferred reliability Practices. NASA. Practice No. PD-ED_1258. Space science documentation from NASA

[4] Myung-Won Sign and myung-Hyun Kim; . An evaluation. of radiation damage to solid state components Flown in low earth orbit satellites Radiation Protection Dosimetry, Vol.108; pp 279-291; 2004;

[5] 'Space Radiation Effects on Microelectronics', NASA Jet Propulsion Laboratory, , pp 118-120; 2002

[6] Pater, S.L., RE Sharp; Gamma radiation effects on bipolar transistors A comparison of surface mount and standard packages; Paper presented at Third European conference, RADECS-95- pp -18-22 ; Sep 1995;

[7] Radiation Induced Effects on Electrical Characteristics Of Semiconductor Devices 1 Seema Mansoor, 2k.M Jadhav, 3munib UR Rahman, 4 Soliha Rahman. Proceedings of 23rd IRF International Conference, 1st May, 2016, Bengaluru, India, ISBN: 978-93-86083-05-0

[8] David R Alexander: Transient Ionizing Radiation Effects in Devices and Circuits. IEEE Tran. On Nucl. Sci. Vol. 50, No.3; June 2003

[9] Reena et al: Performance and Characterization of Siemens Primus Linear Accelerator under small monitor unit and small segments for the implementation of step-and-shoot intensity-modulated radiotherapy. Journal of medical Physics; Vol 31; issue 31: pp 269-274;

[10] www.expeyes.in

[11] G.C. Messenger and M.S. Ash, The effects of radiation on electronic systems, Van Nostrand Reinhold, 2nd edition, 1992

[12] B. Vrsnak1 et al: Kinematics of coronal mass ejections between 2 and 30 solar radii Astronomy and Astrophysics, issue A and A; Vol. 423, No. 2; Aug 4,2004

[13] 'Applications; of Junction Compensation Techniques in reducing Transient Gamma Radiation Effects in Transistor Circuits'

[14] Meidinger et al; 'Alpha Particle, Proton and X-ray Damage in Fully Depleted CCD Detectors for X-ray Imaging and spectroscopy'; IEEE Tran. on nucl. Sci., Vol. 45, No. 6, PP-2849 ;Dec. 1998 ;

[15] J.R.Srou et al; Review of Displacement Damage Effects in Silicon devices;IEEE Tran. Nucl. Sci.; Vol.50, NO.3, June2003.

[16] M. GRAY, D.DAVISSON; The Ergodic Decomposition of Stationary Discrete Random Processes; IEEE Tran. Info Theory, Vol. No.5; September1974.

[17] Aldert van der Ziel, fellow, IEEE ; Unified Presentation of 1/f Noise in Electronic Devices: Fundamental 1/f Noise Sources . Proceedings of IEEE, VOL. 76, NO. 3, March 1988 2005.

[18] Marshall Bautz et al; Anomalous Annealing of High resistivity CCD Irradiated at Low temperature; IEEE Tran. Nucl.sci.Vol. 52, No.2 , April, 2005

[19] Gordon R Hopkinson.Comparison of CCD Damage Due to 10- and 60 MeV ProtonsIEEE Trans. of nucl. Sci; Vol 50, No 6, December 2003

[20] Seema Mansoor, KM Jadhav, Munib ,UR Rahman, and Soliha Rahman, Radiation Induced Effects on Electrical Characteristics Of Semiconductor Devices. Proceedings of 23rd IRF International Conference, 1st May, 2016, Bengaluru, India, ISBN: 978-93-86083-05-0

[21] Tundwal, V. Kumar, N. S. Raghaw & A. Datta (2016) Monte Carlo simulation of radiation damage produced in iron and vanadium by primaryknock on atom 'PKA', Radiation Effects and Defects in Solids, 171:7-8, 658-667, DOI:10.1080/10420150.2016.1241784

[22] Nagendra Singh Raghaw, Vinod Kumar, Ambika Tundwal, Yury Korovin3 and Jindrich Adam; Monte Carlo Simulation of Radiation Damage of SiC and Nb Using JA-IPU Code Journal of Energy and Power Engineering 9 (2015) 967-975 doi: 10.17265/1934-8975/2015.11.005

[23] V Kumar, Ambika Tundwall, Y K Vijay & H S Palsania; Investigation of defect production on iron on gamma irradiation using the positron Doppler broadening Technique; Indian Journal of pure and applied Physics; Vol-54, Jan 2016, pp.51-55

[24] J. R. Srour, Fellow, IEEE, Cheryl J. Marshall, Member, IEEE, & Paul W. Marshall, Member, IEEE; Review of Displacement Damage Effects in Silicon Devices; IEEE TRANSACTIONS ON NUCLEAR SCIENCE, VOL. 50, NO. 3, JUNE 2003